

Pneumatic Power Measurement of an Oscillating Water Column Converter

by
Bavesh Kooverji

*Dissertation presented for the degree of Master of Science in
Engineering (Mechatronic) in the Faculty of Engineering at
Stellenbosch University*



Promoter: Prof J.L. van Niekerk

April 2014

Declaration

By submitting this thesis electronically, I declare that the entirety of the work contained therein is my own, original work, that I am the sole author thereof (save to the extent explicitly otherwise stated), that reproduction and publication thereof by Stellenbosch University will not infringe any third party rights and that I have not previously in its entirety or in part submitted it for obtaining any qualification.

Signature:

Date:

Abstract

A measurement device was developed to accurately determine the pneumatic power performance of an Oscillating Water Column (OWC) model in a wave flume. The analysis of the pneumatic power is significant due to the wave-to-pneumatic energy being the primary energy conversion process and where the most energy losses can be expected. The aim of the research study is to address the accurate pneumatic power measurement of unsteady and bidirectional air-flow in OWC model experiments.

The two fundamental measurements required for the pneumatic power measurement are the pressure difference over an orifice on the OWC model and the volumetric flow rate of air through the outlet. The designed, constructed and assembled measurement device comprised of a venturi flow meter, containing a hot-film anemometer, which could measure the pressure drop and the volumetric flow rate in one device. The assembled pneumatic power measurement device was calibrated in a vertical wind tunnel at steady state. The results from the calibration tests showed that the volumetric flow rate measurements from the pneumatic power measurement device was accurate to within 3 % of the wind tunnel's readings. The pneumatic power measurement device was incorporated onto a constructed Perspex physical model of a simple OWC device. This assembled system was used as the test unit in the wave flume at Stellenbosch University (SUN).

The results from the experimental tests underwent comparative analysis with three analytical OWC air-flow models which were simulated as three scenarios using Matlab Simulink. These results showed that the measurement device has the ability to measure the pneumatic power but there is difficulty in modelling the complex air-flow system of the OWC device. This results in varying levels of agreement between the experimental and simulated pneumatic power results.

The research study has revealed that there is difficulty in designing an accurate device for a wide range of test parameters due to the variance in output values. The unsteady and bidirectional nature of the air flow is also difficult to accurately simulate using a one-dimensional analytical model. Recommendations for further investigation are for CFD systems to be used for the analysis of the air-flow in an OWC system and to be used to validate future pneumatic power measurement devices

Samevatting

'n Meetinstrument was ontwikkel om die pneumatiese kraglewering van 'n model van die Ossillerende Water Kolom (OWK) golfenergie omsetter in 'n golf tenk akkuraat te meet. Dit is belangrik om die omskakeling van golf na pneumatiese energie te analiseer siende dat die grootste energieverlies in dié proses plaasvind. Die doel van hierdie navorsingsprojek was om die akkurate pneumatiese kragmeting van variërende en twee-rigting vloei van lug in 'n OWK model na te vors.

Die twee fundamentele metings wat benodig word vir die pneumatiese kragbepaling is die drukverskil oor die vloei vernouing en die volumetriese vloeitempo van lug deur die uitlaat van die toetstoestel. Die spesiaal ontwerpte meettoestel wat gebruik is in die eksperiment het bestaan uit 'n venturi vloeimeter wat 'n verhitte-film anemometer bevat het wat die drukverandering en die volumetriese vloeitempo kan meet in 'n enkele instrument. Die pneumatiese kragmeting was gekalibreer in 'n vertikale windtonnel waarin 'n konstante vloei tempo geïnduseer was. Die kalibrasieproses het bevestig dat die meettoestel metings lewer met 'n fout van minder as 3 % wanneer dit vergelyk word met die bekende konstante vloei tempo soos bepaal in die windtonnel. 'n Fisiese model van 'n vereenvoudigde OWK golfenergie omsetter was ontwerp en gebou uit Perspex om as toetstoestel te gebruik vir die evaluering van die ontwerpte pneumatiese kraglewering meettoestel. Die toetse was uitgevoer in 'n golf tenk by die Universiteit Stellenbosch (SUN).

The toetsresultate was vergelyk met drie ander OWK lugvloei modelle wat gesimuleer was deur om die analitiese modelle op te stel en te simuleer in Matlab Simulink. Die vergelyking van modellering resultate het gewys dat die meettoestel die vermoë het om pneumatiese krag te meet. Daar was wel komplikasies met die modellering van die komplekse lugvloei in die OWK toestel, die resultate het geen definitiewe ooreenstemming gewys tussen die eksperimentele en gesimuleerde pneumatiese krag resultate nie.

Die navorsingsprojek het gewys dat daar komplikasies is om 'n enkel toestel te ontwerp wat oor 'n wye bereik kan meet weens die variasie van die verskillende parameters. Die variërende en twee-rigting lugvloei is ook moeilik om akkuraat te simuleer met 'n een-dimensionele analitiese simulasiemodel. Aanbevelings vir verdere navorsing sluit in om die lugvloei in die OWK stelsel te modelleer en te analiseer in 'n drie-dimensionele model om die lesings van 'n pneumatiese krag meettoestel te bevestig.

This thesis is dedicated to my loving parents, Hargovind and Taramaty Kooverji, and my dear sister, Praneeta Kooverji. Their support and encouragement throughout my studies has given me the opportunity to grow as an academic and as an individual.

Acknowledgements

I would like to give a special thanks to Professor J.L. van Niekerk for being my supervisor for the duration of my Masters studies. My deepest gratitude is extended to James Joubert for continuously assisting me with my research and for being my co-worker through the experimental stages of my research.

I am very grateful for having received a bursary from The Centre for Renewable and Sustainable Energy Studies (CRSES) and NRF for the duration of my postgraduate studies.

Further thanks go out to Cobus Zietsman for always assisting with equipment selection and workshop labour and Kenny Allen for his unconditional assistance during the wind tunnel calibration tests. His valued advice throughout my experimental tests was very much appreciated. I would also like to thank Professor von Backstrom for his guidance on the design of the pneumatic power measurement device. Lastly I would like to acknowledge all the workers from the wave flume lab at the Department of Civil Engineering for their hard work and support during the wave flume experiments.

Table of contents

Declaration	i
Abstract.....	ii
Samevatting	iii
Acknowledgements	v
List of tables	x
List of figures	xi
Nomenclature	xiv
1 Introduction	1
1.1 Overview of ocean waves and Wave Energy Converters.....	1
1.1.1 Global and regional wave climate	2
1.1.2 Types of WEC's.....	4
1.1.3 The Oscillating Water Column (OWC).....	5
1.2 Thesis objectives.....	6
1.3 Approach to the research study.....	7
1.4 Layout of the thesis	7
2 Literature survey	9
2.1 The water waves	9
2.1.1 Wave theory	9
2.1.2 Ocean wave power.....	11
2.2 Energy conversion - wave to pneumatic energy	11
2.2.1 Energy balance.....	12
2.2.2 Pneumatic power	14
2.2.3 Efficiency of the OWC system.....	15
2.3 Particulars of OWC devices	15
2.3.1 Principle of operation	15
2.3.2 OWC structure.....	16
2.4 SWEC and the ShoreSWEC	16
2.4.1 The SWEC.....	16
2.4.2 Air flow in the ShoreSWEC.....	17
2.5 Experimental air flow measurement in OWC models	18
2.6 Additional air flow measurement techniques	21
2.7 Model testing.....	24

2.7.1	Scaling laws.....	24
2.7.2	Model testing of OWC designs	25
2.8	Resonance.....	26
2.9	Conclusion.....	27
3.	Development of the pneumatic power measurement device.....	28
3.1.	Concepts for measurement device.....	28
3.1.1.	Volumetric flow rate measurement.....	28
3.1.2.	Pressure measurement	31
3.2.	The venturi flow meter.....	34
3.2.1.	Design of the venturi flow meter	34
3.2.2.	Construction and assembly	37
3.2.3.	Measurement locations	38
3.3.	Summary of equipment required.....	38
3.4.	Conclusions	39
4.	Simulation of the pneumatic power from an OWC model.....	40
4.1.	Design of OWC model.....	40
4.2.	Laws of fluid mechanics	41
4.2.1.	Ideal gas law	41
4.2.2.	First law of thermodynamics	41
4.3.	Air-flow models	42
4.3.1.	Constants	42
4.3.2.	Closed-roof OWC model.....	42
4.3.3.	OWC model with an orifice.....	44
4.3.4.	OWC model with pneumatic power measurement device.....	47
4.3.5.	Selection of loss coefficients.....	49
4.4.	Conclusions	50
5	Testing: calibration and experiments.....	51
5.1.	Measuring equipment.....	51
5.2.	Calibration of the pneumatic power measurement tool	52
5.2.1.	The vertical wind tunnel.....	52
5.2.2.	Calibration setup and testing	53
5.2.3.	Results of the calibration tests	55
5.3.	Wave flume experiments	58
5.3.1.	Overview of the wave flume.....	58

5.3.2.	Experimental setup	59
5.3.3.	Test schedule.....	61
5.4.	Conclusions	62
6.	Results and discussion	63
6.1.	Overview of experimental tests.....	63
6.1.1.	Test procedure	63
6.1.2.	Damping	64
6.1.3.	Closed roof tests.....	64
6.1.4.	Basic post processed results.....	64
6.2.	Equipment accuracy & resolution.....	64
6.3.	Comparative analysis of the pneumatic power measurement device.....	66
6.3.1.	Scenario 1 – Model 2 (Sinusoidal water column input)	67
6.3.2.	Scenario 2 – Model 2 (Experimental OWC input)	74
6.3.3.	Scenario 3 – Model 3	76
6.4.	Examination of the wave flume experimental results	77
6.4.1.	Resonance.....	77
6.4.2.	Average Power.....	78
6.4.3.	Efficiency.....	79
6.5.	Conclusions	80
7.	Conclusions and recommendations.....	81
8.	References	83
A.	Derivation of air-flow models	87
A.1.	Model 1 - Closed-roof OWC model	87
A.2.	Model 2 - OWC model with an orifice	91
A.3.	Model 3 - OWC model with pneumatic power measurement device	96
A.4.	Values for simulation parameters	99
B.	Dimensions of constructed test equipment.....	100
C.	Calibration and wave flume testing.....	101
C.1.	Images from calibration tests.....	101
C.2.	Images from wave flume tests.....	102
C.3.	Data acquisition (DAQ) wiring diagram.....	104
D.	Measuring equipment.....	105
E.	Testing schedule	106
E.1	Wave flume testing schedule (smaller wave heights)	106

E.2 Wave flume testing schedule (larger wave heights)	107
E.3 Wave flume theoretical performance curve	107
E.3 Absorption gain curve	108
F. Additional pneumatic power measurement results	109
G. Additional information on OWC devices	111
G.1. Operational OWC devices	111
G.2. OWC related terminology	112

List of tables

Table 3-1: Reasons for non-selection of the concept flow meters.....	30
Table 3-2: Description of the different pressure measurement scales.....	33
Table 4-1: Constants used for the air-flow models	42
Table 4-2: State equations for model 1.....	44
Table 4-3: State equations for model 2.....	47
Table 4-4: State equations for model 3.....	49
Table 5-1: Summary of the calibration results for the hot-film anemometer and the venturi flow meter	56
Table 5-2: Percentage residuals of the calibration tests	58
Table 5-3: Ambient conditions during calibration tests.....	58
Table 5-4: Experimental test parameters	61
Table 6-1: Resolution of measurement equipment.....	65
Table 6-2: Test parameters for the comparative analysis.....	66
Table 6-3: Natural frequency approximation for OWC model	77
Table 6-4: Average Pneumatic Power for larger wave heights	79
Table 6-5: Efficiency calculation for $D=0.6\text{m}$ and $H_w=0.1\text{m}$	79
Table A-1: Constants used for the air-flow models	87
Table A-2: State equations for model 1.....	89
Table A-3: State equations for model 2.....	94
Table A-4: State equations for model 3.....	97
Table A-5: Simulation parameters.....	99
Table D-1: Detailed list of measuring equipment.....	105
Table E-1: Wave flume testing schedule (smaller wave heights).....	107
Table E-2: Wave flume testing schedule (larger wave heights).....	107

List of figures

Figure 1-1: Approximate global distribution of wave power levels (kW/m of wave front) [Thorpe, 1999]	3
Figure 1-2: Wave power levels along the South African coastline (Retief, 2006) ...	3
Figure 1-3: Classification of WEC's (Whittaker, 2006)	4
Figure 1-4: Three-dimensional layout of an OWC device (Patterson et al, 2010) ..	5
Figure 2-1: Wave theory diagram	9
Figure 2-2: Ocean wave spectrum (Bascom, 1980)	10
Figure 2-3: Description of wave energy distribution in an OWC (Wavegen, 2002)	13
Figure 2-4: Diagram of a generalised OWC device during operation.....	15
Figure 2-5: Design of the SWEC's V-shaped structure (Retief, 2006)	17
Figure 2-6: Experimental set-up of caisson model and pneumatic power measurement system (Tseng et al, 2000).....	20
Figure 2-7: Experimental set up of PIV system in the wave flume (Ram et al, 2010).....	21
Figure 2-8: Probe design for oscillating air flow velocity (Jayashankar et al, 1997)	22
Figure 2-9: Cross-sectional view of the flow pipe design and the Pitot tube placement (Lu and Lau, 2008)	23
Figure 2-10: Three-dimensional model of the SWEC (Müller & Retief, 2011).....	25
Figure 3-1: Selection diagram for the air-flow meter	29
Figure 3-2: Permanent pressure loss for the obstruction flow meters (ASME, 1971).....	31
Figure 3-3: Sensing schematic of a diaphragm pressure transducer (Figliola & Beasley, 2006).....	32
Figure 3-4: Possible pressure measurement locations (Islay Limpet Wave Power Plant, 2002).....	33
Figure 3-5: Typical layout of a venturi flow meter (Figliola and Beasley, 2006) ...	34
Figure 3-6: Design and dimensions of bidirectional venturi flow meter (dimensions in mm)	35
Figure 3-7: Non-linear relationship between volumetric flow rate and pressure drop in differential pressure flow meters.....	36
Figure 3-8: Image of venturi flow meter with attached air-ducts and OWC model roof.....	37
Figure 3-9: Horizontal layout showing the pressure tapplings on the venturi flow meter	38
Figure 4-1: CAD drawing of the simple OWC model design (SolidWorks, 2010)	41
Figure 4-2: Sectional view of the closed chamber OWC model.....	43
Figure 4-3: Diagram of the OWC model with an orifice on the roof	44
Figure 4-4: Diagram of the OWC model and the pneumatic power measurement device (venturi flow meter)	48

Figure 4-5: Selection of contraction and expansion coefficients (Çengel and Cimbala, 2010)	49
Figure 5-1: Layout of the complete measurement system.....	51
Figure 5-2: Schematic diagram of the vertical wind tunnel.....	53
Figure 5-3: Setup of the calibration tests at the vertical wind tunnel.....	54
Figure 5-4: Calibration curve for the hot-film anemometer.....	55
Figure 5-5: Calibration curve for the venturi flow meter	56
Figure 5-6: Calibration curve of the pneumatic power measurement device	57
Figure 5-7: Dimensions of the OWC model (mm) and image of the experimental setup	59
Figure 5-8: Experimental setup in the wave flume.....	60
Figure 5-9: Supports for the OWC model in the wave flume.....	60
Figure 6-1: Pressure drop over venturi throat for test $f=0.44\text{Hz}$ and $Hw=0.1\text{m}$ (scenario 1)	67
Figure 6-2: Volumetric flow rate for test $f=0.44\text{Hz}$ and $Hw=0.1\text{m}$ (scenario 1)	68
Figure 6-3: Pneumatic power for test $f=0.44\text{Hz}$ and $Hw=0.1\text{m}$ (scenario 1).....	68
Figure 6-4: Pneumatic power for test $f=0.44\text{Hz}$ and $Hw=0.05\text{m}$ (scenario 1)....	69
Figure 6-5: Pressure drop over venturi throat for test $f=0.67\text{Hz}$ and $Hw=0.1\text{m}$ (scenario 1)	70
Figure 6-6: Volumetric flow rate for test $f=0.67\text{Hz}$ and $Hw=0.1\text{m}$ (scenario 1)	70
Figure 6-7: Pneumatic Power for test $f=0.67\text{Hz}$ and $Hw=0.1\text{m}$ (scenario 1).....	71
Figure 6-8: Pneumatic power for test $f=0.67\text{Hz}$ and $Hw=0.05\text{m}$ (scenario 1)....	71
Figure 6-9: Kaux application on pneumatic power for test $f=0.44\text{Hz}$ at $Hw=0.1\text{m}$ (scenario 1).....	72
Figure 6-10: Kaux application on pneumatic power for test $f=0.67\text{Hz}$ at $Hw=0.1\text{m}$ (scenario 1).....	73
Figure 6-11: Kaux application on pneumatic power for test $f=0.67\text{Hz}$ at $Hw=0.05\text{m}$ (scenario 1)	73
Figure 6-12: Experimental water column displacement for $f=0.44\text{Hz}$	74
Figure 6-13: Experimental water column displacement for $f=0.67\text{Hz}$	74
Figure 6-14: Pneumatic power comparison for test $f=0.44\text{Hz}$ and $Hw=0.1\text{m}$ (scenario 2)	75
Figure 6-15: Pneumatic power comparison for test $f=0.67\text{Hz}$ and $Hw=0.1\text{m}$ (scenario 2)	75
Figure 6-16: Pneumatic power for test $Hw=0.1\text{m}$ $f=0.67\text{Hz}$ (scenario 3)	76
Figure 6-17: Pneumatic power for test $Hw=0.1\text{m}$ $f=0.44\text{Hz}$ (scenario 3)	77
Figure 6-18: Comparison of the average pneumatic power	78
Figure A-1: Sectional view of the closed chamber OWC model.....	87
Figure A-2: Simulink model for OWC model 1.....	90
Figure A-3: Diagram of the OWC model with an orifice on the roof	91
Figure A-4: Simulink model for OWC model 2.....	95
Figure A-5: Diagram of the OWC model and the pneumatic power measurement device (venturi flow meter)	96
Figure A-6: Simulink model for OWC model 3.....	98

Figure B-1: Dimensions (mm) of constructed OWC box with pneumatic power measurement tool attached (SolidWorks, 2010)	100
Figure B-2: Detailed dimensions (mm) of pneumatic power measurement device (SolidWorks, 2010).....	100
Figure C-1: Assembled pneumatic power measurement device	101
Figure C-2: Vertical wind tunnel	101
Figure C-3: Venturi clamped to wind tunnel with air-tight seal on air-duct of the device	101
Figure C-4: Support of venturi during blocked test with polystyrene seal.....	101
Figure C-5: Wave probes and assembled OWC model with measuring device ..	102
Figure C-6: Gauge pressure transducer and hot-film anemometer.....	102
Figure C-7: Differential pressure transducer	102
Figure C-8: Attached pneumatic power measuring device with air-tight seal.....	102
Figure C-9: Front and back supports of the OWC model	103
Figure C-10: Threaded rods strengthening the OWC model.....	103
Figure C-11: DAQ and PSU	103
Figure C-12: DAQ for wave probes and differential pressure transducer.....	103
Figure C-13: Wiring diagram during the wave flume experiments.....	104
Figure E-1: Wave flume theoretical performance curve (HR Wallingford, 2010)	107
Figure E-2: Absorption gain identifier for various water depths	108
Figure F-1: Example of post processed results from the experimental tests.....	109
Figure F-2: Pneumatic Power for larger wave heights at test parameters: $H_w=0.125\text{m}$ $f=0.5\text{Hz}$	109
Figure F-3: Pneumatic Power for larger wave heights at test parameters: $H_w=0.125\text{m}$ $f=0.44\text{Hz}$ & $H_w=0.15\text{m}$ $f=0.44\text{Hz}$	110
Figure G-1: LIMPET Construction and Incline Design Structure (Boake et al, 2002).....	112

Nomenclature

Symbols

A	Area
A_w	Amplitude of water column oscillations
c	Celerity
C_d	Coefficient of discharge
C_p	Specific heat for constant pressure process
C_v	Specific heat for constant volume process
D	Water depth (<i>no subscript present</i>)
D_d	Duct diameter
D_p	Pipe diameter
D_t	Throat diameter
E	Energy
E_w	Energy density of waves
f	Frequency
f_c	Natural frequency
g	Gravitational acceleration
h_1	Air chamber length
h_c	Wave crest height
h_L	Head loss
h_t	Wave trough height
h_w	Water column displacement
\dot{h}	Velocity of air pocket
H_w	Crest-to-trough wave height
K_{aux}	Auxiliary loss coefficient
K_e	Expansion loss coefficient
K_c	Contraction loss coefficient
L_a	Initial height of air chamber
L	Length
m	Mass
p	Pressure
p_a	Atmospheric pressure
P	Power
P_i	Instantaneous wave power
P_{iw}	Incident wave power
$P_{T,inc}$	Total average incident wave power
P_w	Wave energy flux
Q	Volumetric flow rate
\dot{Q}	Rate of heat transfer
R	Gas constant
Re	Reynolds number

T_p	Period
T	Temperature
ΔT	Change in temperature
U	Internal energy
ΔU	Change in internal energy
v	Gas volume
V	Velocity
W	Work done
x	Distance
z	Height

Greek

β	Contraction ratio
ε	Wall roughness
λ	Wavelength
η	Efficiency
ρ	Density
μ	Viscosity
ω	Angular frequency

Abbreviations

CAD	Computer-aided Drawing
CFD	Computational Fluid Dynamics
CTA	Constant Temperature Anemometer
CV	Control Volume
DAQ	Data Acquisition
FSO	Full Scale Output
GHG	Greenhouse Gases
ISO	International Organisation for Standardisation
LIMPET	Land Installed Marine Energy Transformer
MOWC	Multi-resonant Oscillating Water Column
OERG	Ocean Energy Research Group
OES-IA	Ocean Energy Systems International Agreement
OWC	Oscillating Water Column
PIV	Particle Image Velocimetry
PSU	Power Supply Unit
PTO	Power Take Off
PVC	Polyvinyl Chloride
QUB	Queen's University of Belfast
RTD	Resistive Temperature Device
SWEC	Stellenbosch Wave Energy Converter
SWL	Sea Water Level
WEC	Wave Energy Converter

1 Introduction

The majority of the Earth's energy production is extracted from non-renewable energy resources such as fossil fuels and nuclear energy. In particular, the use of fossil fuels has led to negative anthropogenic environmental impacts resulting in climate change. This change is a result of increasing pressure on the earth's atmosphere to absorb greenhouse gases (GHG). The excessive use of fossil fuels has also resulted in the rapid depletion of these finite resources, subsequently causing them to become an expensive commodity. In essence this situation has created a demand for new, clean renewable energy resources.

Looking at the local situation, South Africa is faced with three main issues: an electricity supply shortage, an electricity price increase and a high carbon emission rate. Furthermore, South Africa is ranked in the top 20 carbon emitters in the world and the highest carbon emitter in Africa (South Africa Yearbook 2010/2011, 2011). This can be attributed to the majority of its electricity being derived from fossil fuels. The successful utilisation of renewable energy resources will not only contribute towards the reduction of carbon emissions, it will also ensure the security of energy supply.

The current renewable energy research in the world consists predominantly of the following energy resources: solar, wind, bio and ocean energy. The platform upon which this research study is based is ocean energy. Even though the oceans of the world form 71% of the Earth's composition, it is the least researched area of the renewable energy spectrum. This can be contributed to the high capital expenditure (Capex) costs and harsh functional conditions associated with the implementation of these devices in the marine environment. Continuous research and design endeavours in the ocean energy research sector will build a path for future commercialisation.

Ocean energy research is comprised of five sectors: ocean waves, ocean currents, tides, thermal gradients and salinity gradients. Renewable energy systems that are employed by the action of the waves are known as Wave Energy Converters (WEC) and it forms part of the specific research area for this thesis.

This introductory chapter gives an overview into the global and regional wave climate, a brief description into the various categories of WEC's that are present and an overview of the Oscillating Water Column (OWC) devices related to this research study. The research problem statement will then be presented followed by a description of the approach to this research study of a specific WEC device.

1.1 Overview of ocean waves and Wave Energy Converters

The history of WEC's can be dated back to the 18th century where the first ever patent for a wave energy device was reported in 1799 by Monsieur Girard and his son from Paris (Ross, 1979). Not much is known on the success of this patent but it can be described as being of a pump-action nature that utilises the potential

energy of the ocean's waves. In terms of OWC's history, the first recorded conceptualisation of an OWC is the whistling buoy used for its ability to act as a navigation buoy (Heath, 2012).

The energy density of ocean waves is known to be the highest amongst the renewable energy resources. As a result, it can frequently be seen through waves forcefully crashing on the shoreline, creating large splashes as the energy is dispersed. This is noteworthy considering that the wave energy levels decrease near the shoreline due to frictional losses. As an approximation, there are about 8 000 to 80 000 TWh/year of wave energy or 10 TW of wave power capacity available in the ocean's on Earth (Boud, 2003). The premise for wave energy conversion is to harness the potential and kinetic energy contained in the oceans waves at a particular location and in an efficient manner while also minimising the environmental impact. Having said this, the various types of WEC devices have to be aligned with the characteristics of the ocean's waves at a given location so that successful operation and implementation can be achieved.

When it comes to renewable energy platforms, the reliability and variability of the energy resource must be taken into account. The origin of ocean waves is known to be from solar energy. This energy from the sun creates winds which blow over the ocean; thus converting wind energy into wave energy (Muetze & Vining, 2006). Ram et al (2010) states that as long as there is a wind blowing over the ocean, water waves will always be present. This provides a vast source of wave energy whose variability, from the winter to summer seasons, can be predicted in advance. The factors that would most commonly affect the wave conditions are as follows:

- Wind velocity,
- Distance over which the wind is in contact with the ocean (known as the fetch),
- And time duration over which these wind conditions is in contact with the ocean.

1.1.1 Global and regional wave climate

Figure 1-1 below, shows the approximate global distribution of wave power levels in kW/m. From this figure it can be noted that the western coastlines hold a greater power distribution due to west-to-east winds; therefore it is a more attractive resource for wave energy conversion. Depending on the area conditions and wave conditions, a particular type of WEC can be implemented. The countries that have installed the highest power capacity WEC's thus far are the United Kingdom, Portugal, and Denmark, each with a capacity rating of 315kW, 400kW and 215kW respectively (OES-IA, 2009).

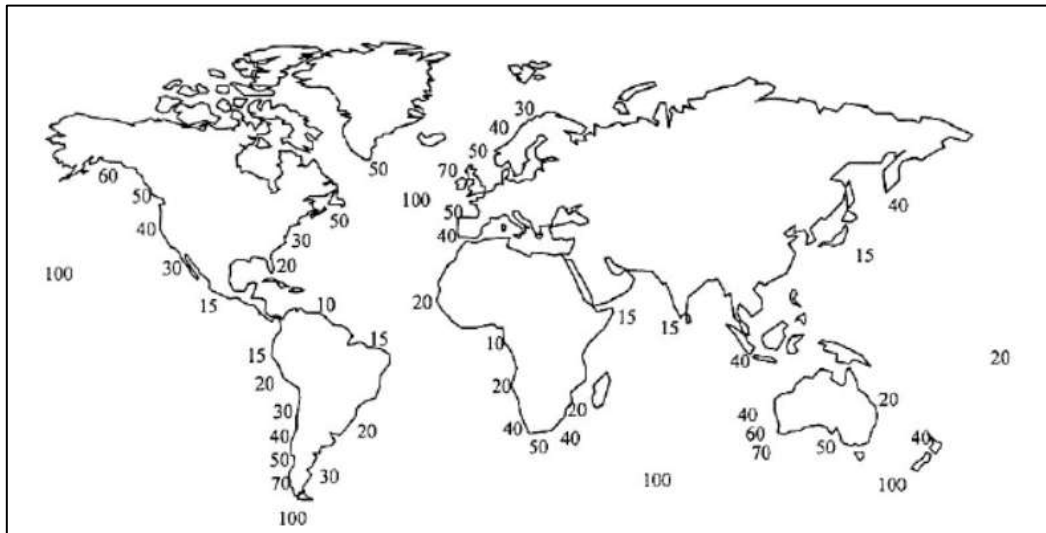


Figure 1-1: Approximate global distribution of wave power levels (kW/m of wave front) [Thorpe, 1999]

Focusing the attention on South Africa, the OES-IA (2009) states that the South African coastline is a useful wave energy resource with a yearly average wave power of 40 kW/m. From Figure 1-2, it can be seen that the stretch of coastline from the Namibian border (20 kW/m) down to the Cape Agulhas region (25 kW/m) holds the optimum average levels of wave power for the placement of WECs. Given these attractive qualities, the further research into WECs will be useful in future renewable energy penetration in the South African electricity grid. This is after the government has stated in the White Paper on Renewable Energy that a total renewable energy generation of at least 10 000 GWh must be achieved by 2013 (DME, 2003).



Figure 1-2: Wave power levels along the South African coastline (Retief, 2006)

1.1.2 Types of WEC's

The fundamental aspect with regards to developing a WEC device is to match the specific planned mode of operation of the device to the wave environment that it will be placed in. Essentially this means that the device should be appropriately matched with its mode of operation of capturing the combination of potential and kinetic energies of the waves at a desired location. Figure 1-3 indicates the four classification properties of a WEC which can be used to develop a WEC power plant. These include the structural reference frame of the device, the Power Take Off (PTO), the location and the function of the device. The selection from each of the properties would give the developed WEC device a specific feature in which it would harness the energy from the oceans waves.

As an example, the Oyster is a point absorber WEC that moves relative to the sea bed. It has a hydraulic power take off system and is located near the shoreline. A categorical description of a few distinguished commercial WEC devices that have been in operation are listed below:

- The Pelamis (hydraulic PTO, relative motion between floats, attenuator, offshore),
- The Archimedes Wave Swing (electrical PTO, fixed to the sea bed, point absorber, offshore)
- and the LIMPET (pneumatic PTO, fixed structure, terminator device, shoreline)

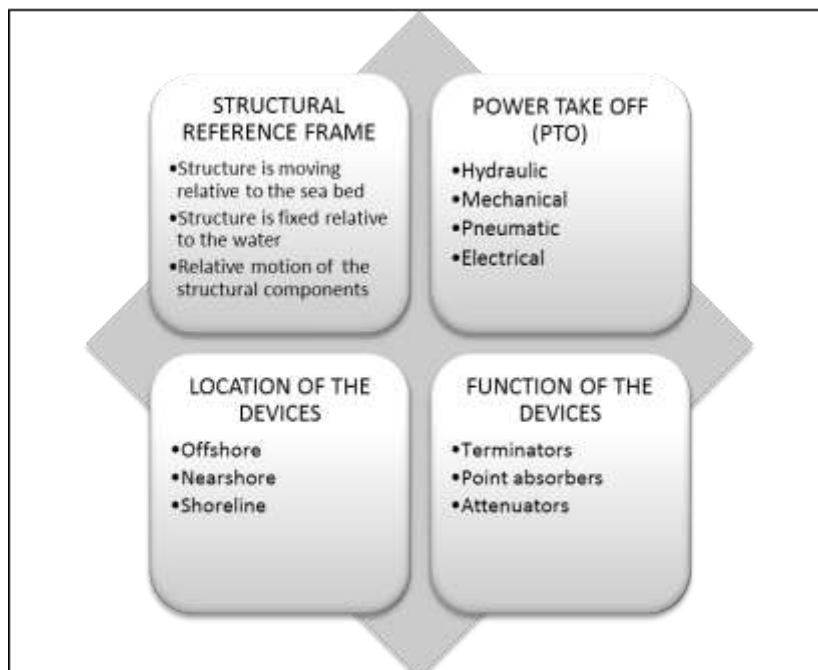


Figure 1-3: Classification of WEC's (Whittaker, 2006)

1.1.3 The Oscillating Water Column (OWC)

As an overview, Mendes & Monteiro (2007) has concisely stated that an OWC device is basically a hydraulic machine whose power take-off (PTO) mechanism is of a pneumatic nature, where this mechanism is a pneumatic chamber that is connected to an air turbine to harvest the energy. The aforementioned specific category of WEC's is pertinent to this research study. In particular, it is the pneumatic power take-off which is being investigated in this thesis, since it is the product of the primary energy conversion process in an OWC device.

Referring back to Figure 1-3, an OWC device can be classified as a WEC that is commonly a terminator device and is also a fixed structure relative to the movement of the waves. These devices are found to be either a near shore or shoreline structure and utilise the pneumatics from an air chamber for the power take-off system. Details of operational OWC devices and relevant terminology can be found in appendix G.

OWC devices integrate the conversion of wave energy to pneumatic energy through the oscillation of a trapped water column in a chamber. At the bottom of the structure, the energy from the waves is fed into the water column through a submerged opening, which results in the water column movement. Thereafter the air pocket, located above the water column, undergoes the induced oscillatory motion which is essentially utilised to drive an air turbine. The mechanical energy attained by the turbine can consequently be converted to electrical energy via an electrical generator.

Figure 1-4 illustrates a three-dimensional sectional layout of an OWC structure, where multiple chambers are placed alongside each other. The air pocket above the water column leads to the turbine-generator area through an inter-leading vent.

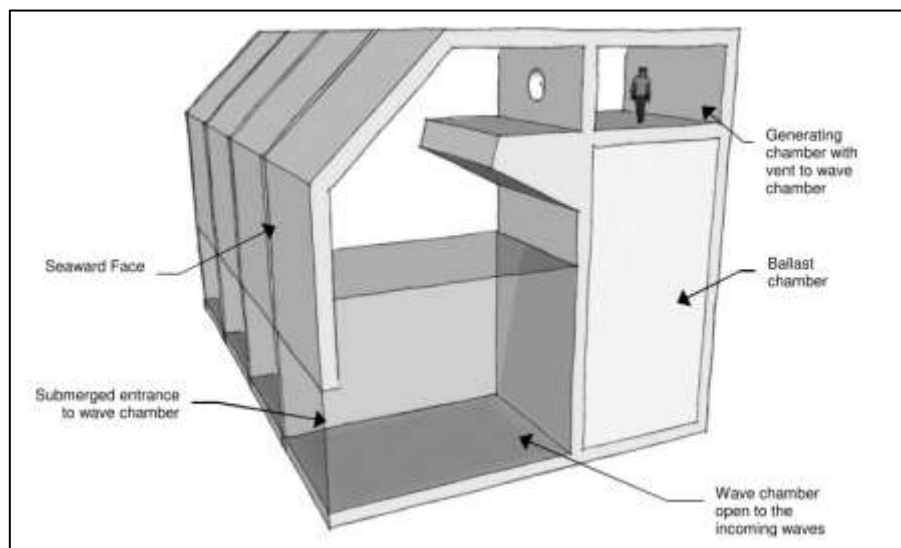


Figure 1-4: Three-dimensional layout of an OWC device (Patterson et al, 2010)

With regards to the turbine selection for an OWC device's pneumatic PTO, there has been a preference towards the use of the bidirectional Well's turbine as opposed to the Impulse turbine due to the bidirectional air-flow capability. Even though this turbine seems well suited to the oscillatory motion of the air chamber, there remain accounts of this turbine having a lower than predicted efficiency. A key advantage for the use of a unidirectional turbine is that it normally delivers high efficiencies as opposed to the Well's turbine (Ackerman, 2009).

To date, there have been many accounts of experimental tests performed on OWC models. Some of these tests are based on OWC model design for efficiency analysis, investigation of the air-flow characteristics in the air chamber and air turbine modelling. None of them have accurately researched the measurement of the pneumatic power generated from an OWC device. In this research study, the pneumatic power measurement of the oscillatory air-flow to and from the air chamber was the primary focus of this study.

1.2 Thesis objectives

The energy efficiency which is the most important in OWC devices is the conversion from wave energy to pneumatic energy, since it is the primary energy conversion process and the area within which most energy losses can be found. This research deals with the testing of a designed, constructed and assembled pneumatic power measurement device, which can accurately measure the power of the air-flow through a model of an OWC device.

The designed pneumatic power measurement device will offer a platform to quantify the power capacity of an OWC design at a scaled down level. This is considering that the resultant power of the air-flow in an OWC system is a measure of the rate of acquired energy that can be utilised to generate electricity.

The sub-objectives of this research study are as follows:

- Design a theoretical model of the air-flow in the OWC model's air chamber by examining the fluid mechanics of the pneumatic system. This entails the understanding of the incoming wave energy source and the resultant air-flow in the system. Through this understanding, the establishment of the required measurement and measurement ranges can be defined to compute the pneumatic power into and out of the OWC air chamber.
- Investigate different strategies of performing the pneumatic power measurement and determine what appropriate equipment is needed for these accurate measurements.
- Design, construct and assemble the pneumatic power measurement device that will be implemented with the designed model of the OWC device.
- Perform calibration testing of the measurement device in order for accurate measurements to be recorded during model testing in the wave flume.

- Design and build the models of the OWC devices to be implemented with the air flow measurement device during the testing phase of the research study.
- Compare the results of the experimental testing from the air flow measurement device with the theoretical results from the air flow model.

This investigation of the pneumatic power through model testing of an OWC device design allows the power of a full scale system to be calculated.

1.3 Approach to the research study

The design of the pneumatic power measurement device was based on reviewing literature of experimental OWC device testing and aiming to fill the gap where accuracy of measurements regarding the pneumatic power was not maintained. This design was reinforced by further research into other applications concerning accurate air-flow measurement relative to the air-flow characteristics in an OWC device's air chamber.

As outlined in the objectives of the research study, the assembled pneumatic power measurement device was incorporated into an experimental model of an OWC during wave flume experiments. The initial model testing was performed on a simple model of an OWC device. The results from these tests were compared to a simulation air-flow model created in Simulink (Matlab, 2010), in an effort to validate the experimental pneumatic power results.

1.4 Layout of the thesis

The thesis is structured to firstly provide information in Chapter 2 (Literature Survey) on ocean wave theory and ocean wave power, and then explain the details on OWC systems. Previous research into experimental air-flow measurements is also documented with special attention being paid to wave flume related experiments.

Chapter 3 looks at the development of the pneumatic power measurement device from concept analysis to final design. This entails concepts for the measuring device, the detailed development of the pneumatic power measurement device and the equipment required going forward into the research study.

Chapter 4 details three simulation models which stem from an analytical analysis of the air-flow in an OWC model. This chapter lists important assumptions and fluid mechanics properties which have been incorporated into the analytical models.

Chapter 5 and Chapter 6 describe the calibration tests and the results from the wave flume experiments respectively. The documentation of the calibration tests involves the selection of the measuring equipment, calibration test results and an overview of the wave flume system and the experimental setup in the wave flume. Chapter 6 documents the process where the experimental results from the wave flume experiments are validated with the analytical models described in chapter 4,

which are simulated in Matlab Simulink. Further results from the wave flume experiments are then analysed.

Chapter 7 lists the relevant conclusions made on the findings of the research study, which relate to the design of the pneumatic power measurement device, calibration tests, validation of the experimental results and lastly analysis of the pneumatic power measurements.

2 Literature survey

This literature study provides a theoretical platform for the research by outlining wave theory, wave power, pneumatic power and the experimental measurement of air flow in OWC devices and other applications.

2.1 The water waves

The energy conversion boundaries for an OWC device are as follows:

1. Wave to pneumatic energy (water to air)
2. Pneumatic to mechanical energy (air to turbine)
3. Mechanical to electrical energy (turbine to electricity)

These energy transformations are performed over certain control boundaries where the energy is transmitted to the next medium. Even though this research study only deals with the pneumatic power flowing through an OWC model, the energy entering the OWC device must be investigated before looking at the energy movement through the air chamber. Firstly, the water waves will be studied and then the power of the water waves will be examined.

2.1.1 Wave theory

The waves of the ocean are made up of various combinations of wave types which contribute to its complex nature. Before the description of the wave types are given, Figure 2-1 will be used to introduce the nomenclature of wave theory (Muetze & Vining, 2006).

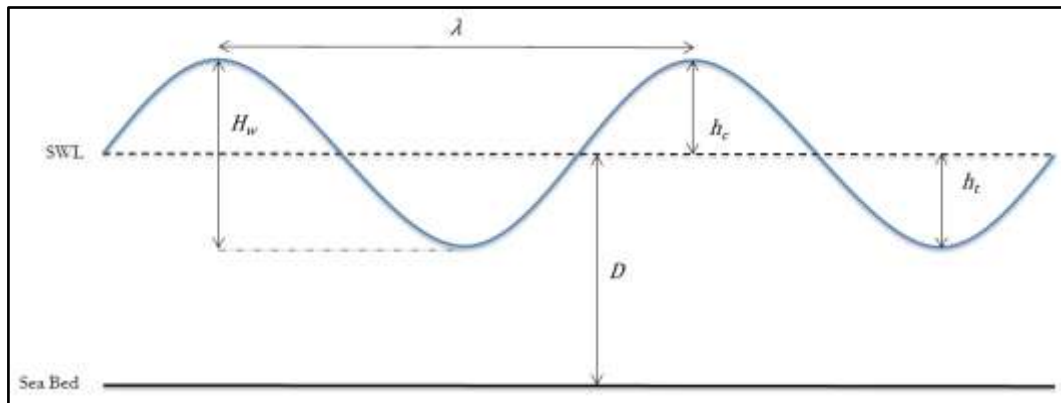


Figure 2-1: Wave theory diagram

Where H_w is the wave height, D is the water depth, h_c is the crest height, h_t is the trough height and λ is the wavelength.

As previously mentioned, the oceans waves are generated from the winds that blow over the oceans. These wind waves manifest as three types of wave forms:

1. Capillary waves
2. Seas
3. Swells

Capillary waves are seen as ripples in the ocean. Seas are the high frequency waves created by local winds over short fetches and lastly, swells are regular wave forms acquired from wave-source areas over long fetches.

Figure 2-2 describes the relative amount of energy contained in each type of wave form described above and for more extreme waves. It is evident from Figure 2-2 that seas and swells hold the highest energy in the ocean wave spectrum.

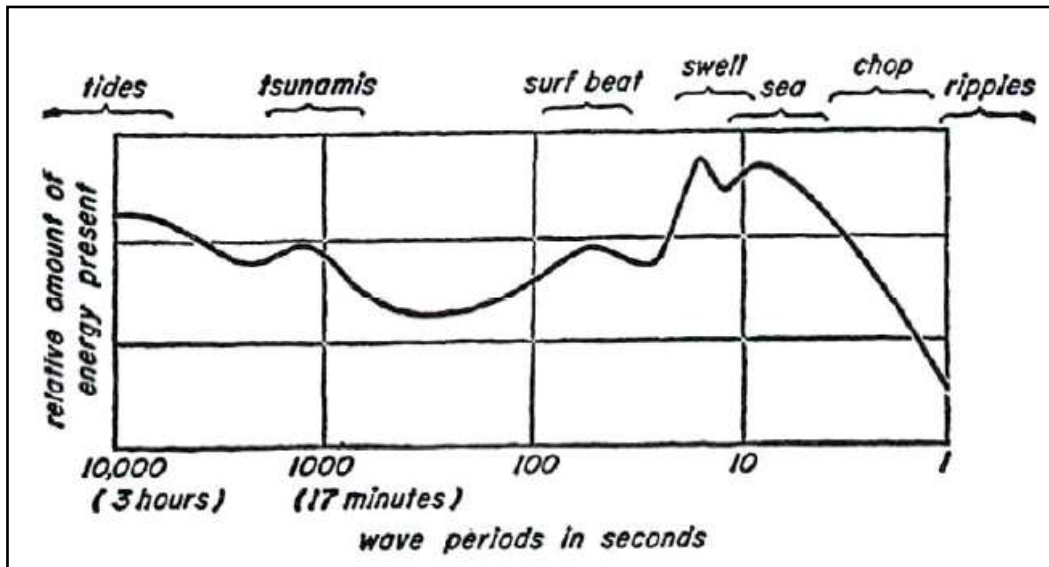


Figure 2-2: Ocean wave spectrum (Bascom, 1980)

In the development of this thesis, swells in shallow water will be analysed using linear wave theory which offers an idealistic approach that simplifies the investigation of the incident waves on an OWC device. These simplistic wave forms have been utilised during the theoretical simulation of the air flow model in an OWC device model. The equation for a regular wave function with two variables is given in equation 2-1 (Krogstad and Arntsen, 2000).

$$\eta(x, t) = a \sin\left(\frac{2\pi}{T_p} t - \frac{2\pi}{\lambda} x\right) \quad (2-1)$$

Where a is the amplitude, $\frac{2\pi}{T_p}$ is the angular frequency ω , $\frac{2\pi}{\lambda}$ is the wave number k , T_p is wave period and λ is the wavelength.

During the propagation of waves in shallow water, where the water depth D is less than half of the wavelength λ , the surface particles of the waves follows a trace resembling that of an ellipse. So for the description of incident waves to an OWC in shallow water, the wave's motion can be envisaged by this elliptic oscillating motion. The oscillatory motion has a certain speed in the wave's

propagation direction, and so for shallow waves this velocity is known as the wavefront velocity (phase velocity), which is given as the celerity c in equation 2-2.

$$c = \sqrt{\frac{g\lambda}{2\pi} \tan \frac{2\pi D}{\lambda}} \quad (2-2)$$

For shallow water swells, a key feature of ocean wave theory is wave breaking, which takes place when its structural form can no longer support its top. This occurs when the wave height H_w is greater than 80% of the water depth D .

2.1.2 Ocean wave power

When considering the power available from the ocean's waves, the energy transported in the wave motion should first be analysed. The energy density of waves (E_w) is the amount of energy that is transported in an area of horizontal wavefront, perpendicular to the wave direction which is given by equation 2-3.

$$E_w = \frac{\rho g H_w^2}{16} \quad (2-3)$$

The energy density of waves is transported by waves propagating through the ocean at a specific transport velocity, known as the group velocity c_g , and is calculated from equation 2-4, where h also refers to the wave height H_w . This velocity differs from the wavefront velocity in that the group velocity takes into account a train of waves.

$$c_g = \frac{g \tanh kh}{2\omega} \left[1 + \frac{2kh}{\sinh 2kh} \right] \quad (2-4)$$

Equation 2-5 defines the power flux (wave energy flux) of the waves P_w calculated from the product of the average energy density of waves along the wavefront and the group velocity c_g . The wave energy flux provides the power per metre of wavefront (kW/m). If, for example, the incident wave power capacity P_{iw} on a width of an OWC device's opening is desired, the wave energy flux P_w should be multiplied with the opening width b to determine the power (kW). By utilising the incident wave power P_{iw} (Mendes & Monteiro, 2007), the total average incident wave power over a wave period T_p can be solved by using equation 2-6.

$$P_w = E_w c_g \quad (2-5)$$

$$P_{T,inc} = \frac{1}{T} \int_0^T P_{iw} dt \quad (2-6)$$

2.2 Energy conversion - wave to pneumatic energy

When analysing the proposed OWC model for energy conversion from the medium of water (waves) to the medium of air (pneumatic), a suitable theory

must be applied to the system. This is to ensure that throughout the analysis of the application, the measurement of the rate of energy into and out of an OWC model is performed accurately.

2.2.1 Energy balance

In the energy conversions from the waves to pneumatic power, there must be an energy balance of the system, so that the various energy components can be accounted for. In this section, the wave energy conversion to pneumatic energy is firstly described by the law of conservation and then the energy equation is utilised to investigate the energy in the air chamber.

The law of energy conservation is applied to the system so that it takes into account the energy entering and leaving the OWC due to the waves. Tseng (2000) encompasses the use of the law of energy conservation for the OWC application by equation 2-7.

$$E_I = E_W + E_R + E_L \quad (2-7)$$

Where: E_I – The incident-wave energy

E_W – The energy transmitted to the pneumatic chamber

E_R – The reflected wave energy

E_L – The frictional energy loss due to viscosity and turbulent motion of the waves

Equation 2-7 states that the energy of the incident waves to an OWC device will be distributed into three divisions of energy forms: reflected wave energy (E_R) in the water, frictional energy (E_L) in the walls of the OWC and sea bed and the most important energy form for the air flow measurement: the pneumatic energy (E_W).

The incident waves to the OWC device diverge into three movements when in contact with the device. Figure 2-3, adapted from Wavegen (2002), shows a diagrammatic description of these three divisions according to the energy transmission described in equation 2-7.

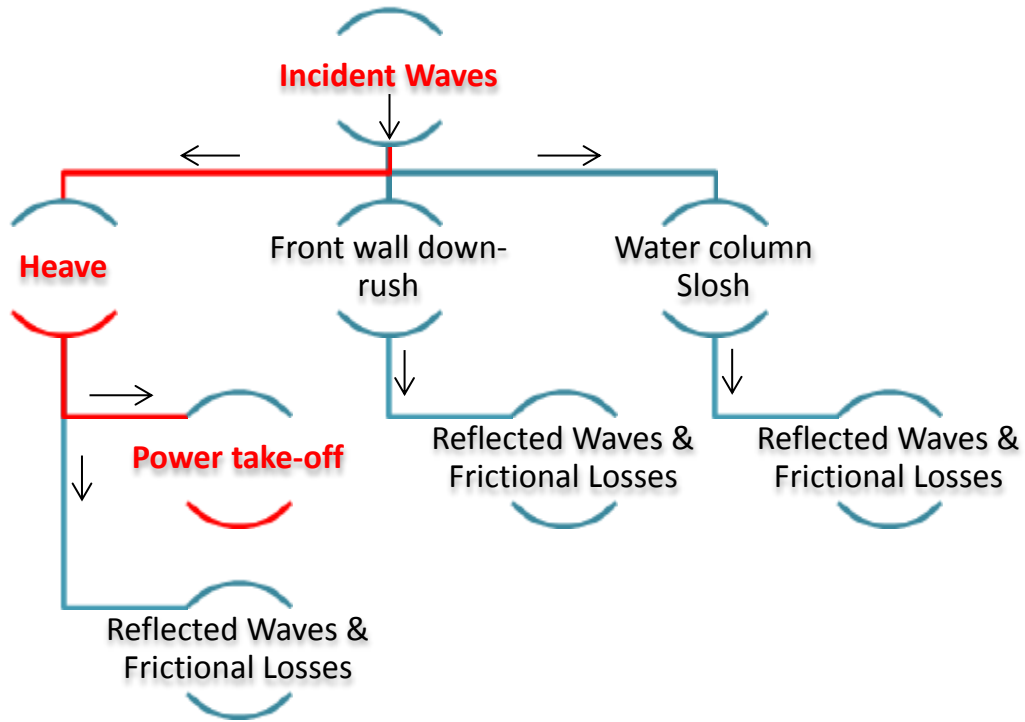


Figure 2-3: Description of wave energy distribution in an OWC (Wavegen, 2002)

The process flow from incident waves to heave (marked in red in Figure 2-3) is the previously described segment of wave energy which contributes to the energy transfer to the air chamber. The heave motion of the waves is the upward lift of the water column in an OWC device, which contributes to the compression of the air in the pneumatic chamber. This would then provide energy for the PTO process.

For the design of the air flow measurement system, the understanding of the flow characteristics in an OWC air chamber has to be analysed in a simulation model. This is achieved in the research study through the application of the energy equation shown as equation 2-8, which looks at the energy balance between two points in a pipe flow (Fox et al, 1999).

$$\frac{p_1}{\rho g} + \frac{v_1^2}{2g} + z_1 + W_{pump} = \frac{p_2}{\rho g} + \frac{v_2^2}{2g} + z_2 + W_{turbine} + h_L \quad (2-8)$$

The first three terms of either side of the energy equation respectively represent the potential energy, the kinetic energy and the relative height of the flow at two distinct points in the system. The head loss (h_L) takes into account the frictional losses due to viscous flow. The terms of the work done by a pump (W_{pump}) and to a turbine ($W_{turbine}$) will not be considered in the theoretical model of the air flow since there will no pump work or turbine work present in the control volume of the applications air flow.

The application of the energy equation will be referred to in detail in the air-flow model of this thesis.

2.2.2 Pneumatic power

As mentioned before, the primary performance analysis of an OWC device is based upon the power of the air flowing out of and into the air chamber. Essentially, this is an air-flow exchange between the air in the pneumatic chamber and the atmosphere outside of the OWC chamber. This flow path control volume would involve the air volume from the free water surface in the OWC's air chamber to the top of the OWC structure where the resultant air flow would enter and exit the turbine chamber in an air-duct. For accurate measurement of the power of the air flow, the necessary measurement components for pneumatic power need to be defined.

Firstly, the instantaneous power $P_i(t)$ is defined by equation 2-9.

$$P_i(t) = \int p(t) \frac{x}{t} dA \quad (2-9)$$

Where: $p(t)$ - Air pressure in the air chamber relative to the atmosphere

$\frac{x}{t}$ - Velocity of air through the turbine

$\int dA$ - The area through which the volume of air flows

Equation 2-10 gives the instantaneous pneumatic power from an OWC device.

$$P_i(t) = p(t) \int v(t) dA \quad (2-10)$$

Where: $v(t)$ - Instantaneous air flow velocity of air through duct of area A at time t

The instantaneous air power P_i , given by equation 2-11, can be translated to a total average absorbed power $P_{T,abs}$ by measuring P_i over a time interval T (Thiruvankatasamy, 1997).

$$P_{T,abs} = \frac{1}{T} \int_0^T p(t) Q(t) dt \quad (2-11)$$

From the above derivation of the total average absorbed power $P_{T,abs}$ in an OWC device, it can be established that the pressure drop over the turbine and the volumetric flow rate $Q(t)$ through the turbine are the fundamental components in measuring the pneumatic power that is delivered to a turbine. This resultant power of the air flow can be used for the efficiency calculations of the system.

In the concepts and design stage of the air flow measurement system, the pressure and volumetric flow rate measurement techniques and equipment will be investigated.

2.2.3 Efficiency of the OWC system

The term efficiency is a fundamental aspect to any system because it describes how well a system is performing under the given conditions. In terms of an OWC device the pneumatic efficiency is defined as the power available to the turbines with respect to the power delivered to the system by the incident waves. This efficiency η is shown below by equation 2-12.

$$\eta = \frac{\text{Total Absorbed Power}}{\text{Total Incident Power}} = \frac{P_{T,abs}}{P_{T,inc}} \quad (2-12)$$

2.3 Particulars of OWC devices

2.3.1 Principle of operation

The analysis of the operation of an OWC device incident to ocean waves is detailed in this section. Figure 2-4 describes a generalised setup and operation of a terminator OWC device during its interaction with incident waves. The figure shows the resultant water column movement when a crest of a wave, trough of a wave and still water conditions is incident to the device.

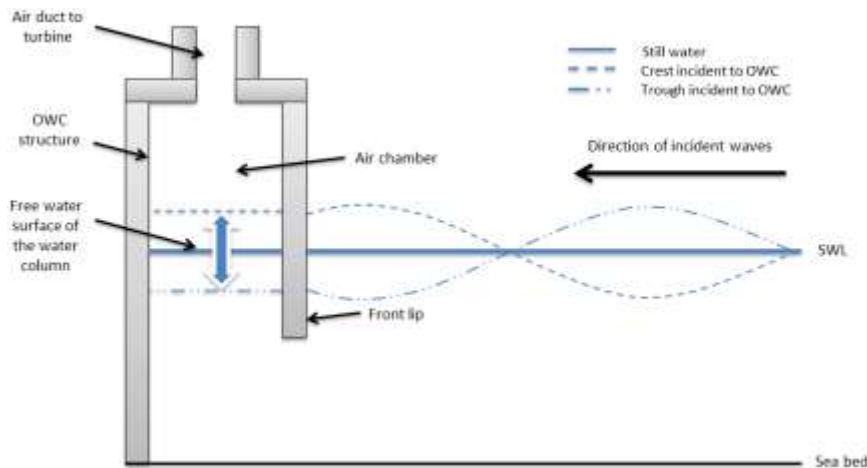


Figure 2-4: Diagram of a generalised OWC device during operation

When a crest of a wave is incident to an OWC device, the water column trapped by the OWC structure rises in the caisson. This results in the compression of the air chamber and a resultant increase of the air pressure in the chamber. The pressure increase creates a differential pressure between the air chamber and the atmosphere outside of the box. The potential energy due to the pressure increase is converted to kinetic energy through the air flow out of the air duct and into the atmosphere. In the case of a wave trough incident to the device, the water column falls in the caisson and the air pressure decreases in the air chamber. This phenomenon is known as rarefaction of the air chamber. As a result, air flows into the air chamber through the air duct due to higher ambient pressures outside of the box relative to the air chamber. During still water conditions, there is no oscillatory motion of the water column or air-flow through the air-duct.

The resultant oscillatory motion of the air chamber can be viewed as an inhalation and exhalation process of air through this chamber. Consequently this induced, bidirectional air-flow can be utilised to drive an air turbine in the duct of the OWC structure. For the experimental model testing of an OWC device, there would be no physical turbine present in the model structure. The orifice of the air duct, known as the dissipator, would be a representation of the turbine due to its ability to resist the flow of the air to and from the air chamber. Mendes and Monteiro's (2007) work on the modelling of a turbine as a dissipator showed the important effects of the dissipator type and size on the amount of energy dissipation of the OWC system.

The functional elements of an OWC, from the waves, to the water column and to the air chamber are at different pressure levels depending on the operation of the OWC. These various pressures can be measured from the static pressure on the sea-bed to the air pressure drop over the dissipator. These measurements can be utilised during model testing to monitor the OWC model's operational performance.

2.3.2 OWC structure

Referring to the structural aspects shown in Figure 2-4, it is understood that there can be various geometric arrangements of an OWC device to derive optimum energy efficiencies of the system. This could include variations to the front lip submergence depth, opening width of the OWC device entrance to the incident waves, geometry of the base of the water column from the entrance and the air chamber geometry.

Horko (2007) performed a computational fluid dynamics (CFD) analysis on the OWC structure while focussing on the effects of the front wall geometry and front wall aperture shape of an OWC. He concluded that the front wall aperture shape provided a substantial improvement on the efficiency of the device if the lip of the front wall is rounded or the thickness of the front wall is increased.

For this research study, the simple OWC structural design shown in Figure 2-4 is implemented so that the designed pneumatic power measurement system can first be validated. Thereafter the measurement platform can be applied to future model tests of OWC concept designs for verification of optimum geometry.

2.4 SWEC and the ShoreSWEC

2.4.1 The SWEC

The deployment of the Stellenbosch Wave Energy Converter (SWEC) concept came about in 1979 by Professor Deon Retief and Mr Johan Muller of the Ocean Energy Research Group (OERG) at Stellenbosch University. This idea was conceptualised as a result of the oil crisis in the late 1970's. The SWEC was

designed so that it incorporates a rectified air flow intake from the incident waves rather than the direct PTO from a typical OWC air chamber. This notion was achieved by designing a structure that integrated multiple OWC modules in a V-shaped entity so that each individual module contributed its own absorbed pneumatic energy to a single power train located at the head of the V-formation. Figure 2-5 shows the design of one of the V-shaped structures rated at 5 MW that would form part of an array of WEC's.

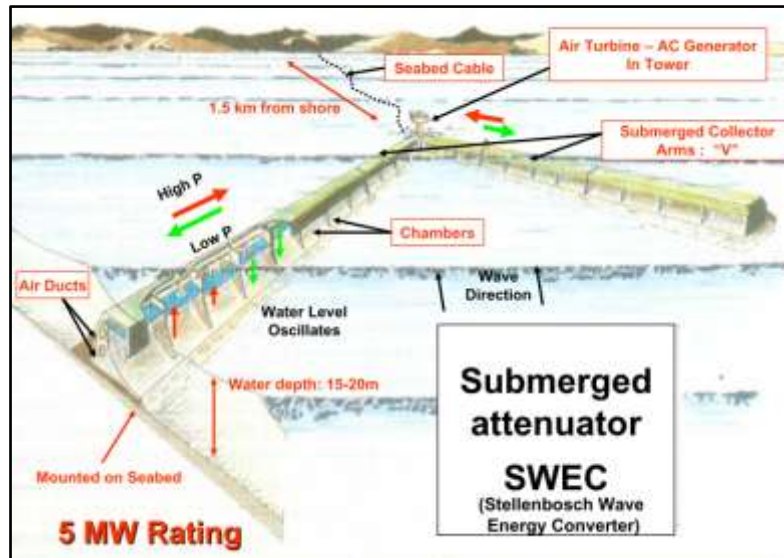


Figure 2-5: Design of the SWEC's V-shaped structure (Retief, 2006)

Since the chambers of the SWEC are underwater, the requirement for an air pump was noted in the prototype design to maintain a preferred air volume in the air circuit and to control initial water column levels. This air pump would also cater for the air losses that could be incurred in the system during operation. The concept of the air pump was not added into the model studies.

The SWEC is still in the development phase and is yet to be implemented as a demonstration unit

2.4.2 Air flow in the ShoreSWEC

The ShoreSWEC design introduces a different operational scheme compared to a general OWC design with regards to the wave energy entering the water column. The device is designed to allow orthogonal waves to pass the structure's opening which enables the difference in static pressures of the water column and passing wave to be the driving force. The ShoreSWEC system uses the same fundamental aspects as the SWEC with regard to the rectified flow of air from multiple OWC chambers to a central PTO unit where the electricity is generated. The ShoreSWEC design, based on the SWEC system, was patented by Professor JL van Niekerk and Professor G de Fallaux Retief.

The advantages of having the ShoreSWEC operate with the rectified flow of air is that it allows the smooth flow of air to the turbine, hence delivering less extreme variance in turbine operation. The control of the rectified air flow is achieved through high and low pressure valves according to the compression or expansion of the air pocket.

2.5 Experimental air flow measurement in OWC models

The air-flow in an OWC device's air chamber has been studied in detail over the years. This research ranges from numerical simulation of the air-flow to experimental testing of the chamber; the latter being relevant to this research study. This section deals with the experimental tests performed on OWC models, while paying close attention to the air-flow measurement techniques.

The pneumatic power measurement in the closed-loop air flow system of the SWEC model, involved the use of a volumetric gas flow gauge and a differential pressure sensor (Retief, 1982). The gas flow gauge measured the volumetric flow rate of the air from the high to low pressure manifolds, while the pressure transducer measured the pressure drop over the flow gauge. The rise and fall of the water column due to oscillatory motions were monitored using resistance probes.

The efficiency analysis of a Multi-resonant OWC (MOWC) wave energy caisson in an array for a breakwater application was looked at by Thiruvenkatasamy (1997). Each caisson comprised of an OWC chamber, a dome in the air chamber to concentrate the flow and a duct for the turbine placement. The efficiency of the MOWC model in the wave tank was defined for the pneumatic efficiency which required the pneumatic power flowing through the air chamber to be known. This was achieved using an inductive-type pressure transducer with a ± 0.5 bar measuring range and the velocity fluctuations of the oscillating water column, measured by a wave probe. The pressure transducers were positioned in inner portions of the top of the dome of the caisson. In this experimental analysis, the volumetric flow rate of air flowing through the air duct was calculated using the water column velocity.

During the physical OWC model testing performed by Mendes & Monteiro (2007), they calculated the airflow rate through the exhaust orifice using the water column velocity, as seen in Thiruvenkatasamy (1997). However this was performed using a video camera to record successive movements of the water column through each oscillation. An adjustable tripod holding the camera was placed facing the glass wall of the wave tank adjacent to the OWC model. The real-time recordings from the camera were uploaded onto a separate computer for water column motion analysis. Individual frames of the water column movement were utilised for the volumetric flow rate of air through an AutoCAD analysis. The governing equation of this analysis is shown in equation 2-13.

$$Q_{air} = \frac{\text{Volume of water column}_{frame 2} - \text{Volume of water column}_{frame 1}}{\text{time}_{frame 2} - \text{time}_{frame 1}} \quad (2-13)$$

The single frames of the water column movement along with the pressure readings in the OWC chamber were shown in real time on a digital multimeter. The pressure readings were measured using a pressure transducer with a working range of ± 6.9 kPa (1 psi).

In earlier OWC experimental tests, Sarmento (1992) performed wave flume experiments on OWC models to compare the theoretical and experimental curves for the efficiency and the reflective and transmission coefficients. It was noted that the rate at which the water column is displaced cannot be used for the volumetric flow rate of air through the turbine due to the effects of air compressibility (Sarmento, 1992). Furthermore for scale model testing, Sarmento and Falcão (1985) explained that for a full sized WEC plant, the air compressibility effect plays a substantial factor in the performance analysis. Given this information, the volumetric flow rate of air through the air chamber for these tests was determined by measuring the instantaneous pressure in the air chamber as a result of calibrated filters. Ten filters, of synthetic carpet material were utilised, each being calibrated at approximately ten different velocities. The relationship between the pressure drop over the filter is given by the second-order polynomial of the mean velocity through the filter shown in equation 2-14.

$$p = \mu C_1 v + \rho C_2 v^2 \quad (2-14)$$

Where μ is the air viscosity, C_1 and C_2 are the calibration coefficients, v is the air velocity and ρ is the air density.

The accuracy of the filter's calibration was achieved through calculation of the average percentage deviation of the calibration pressure differences to the measured pressure differences. The accuracy results showed a 2 % deviation. A key parameter of these experimental tests depicting the represented linear turbine, is the air-flow-to pressure-drop-ratio K , where $K = Q/p$. The pneumatic pressure of the air chamber was measured using a differential manometer.

Other methods involving the measurement of the volumetric flow rate of air generated from the oscillating air chamber is the use of an air rotameter. Basically, this equipment is made up of a scaled and transparent tapered tube which contains a 'float' (Hayward, 1979). When there is no flow present, the 'float' rests at the base of the tube and as the flow increases the float ascends in the tube which results in a wider flow opening for the moving fluid. The flow rate of the fluid can be determined from the risen height of the float which can then be directly read off the appropriate scale on the tapered tube. Dizadji and Sajadhan (2011) utilised an air rotameter for flow rate measurement in their experimental analysis of the geometry of an OWC model. In all their experiments, the compression or either the expansion of the air chamber were only investigated therefore a rotameter was an appropriate selection given its ability to only

measure the flow in one direction. They also measured the air pressure at the top of the air chamber using a Pitot tube connected to a digital manometer. Furthermore, the flow rate readings allowed the calculation of the Reynolds Number (Re) of the exit air flow so that the flow regime could be evaluated.

During the model studies on an OWC caisson, Tseng et al (2000) calculated the pneumatic power of the WEC model by utilising pressure measurements along with the rotational velocity of a 48-blade air turbine at the top of the model. This turbine rotated in one direction, despite the bidirectional flow of air. A steel shaft and a 3 cm aluminium thread roller protruded above the turbine, from which a load of various weights were suspended via a pulley system. The operation of this velocity measurement system was that as the air turbine rotated, the attached load would rise a certain height in a measured time frame; therefore allowing the velocity of the air through the turbine to be calculated. The air pressure was measured in the air chamber and the front orifice of the air turbine using two differential pressure transducers. The pressure measurements were taken with respect to the ambient pressure conditions. Figure 2-6 shows the experimental set-up along with the pneumatic power measurement system of the differential pressure sensors and the moving load due to the air turbine.

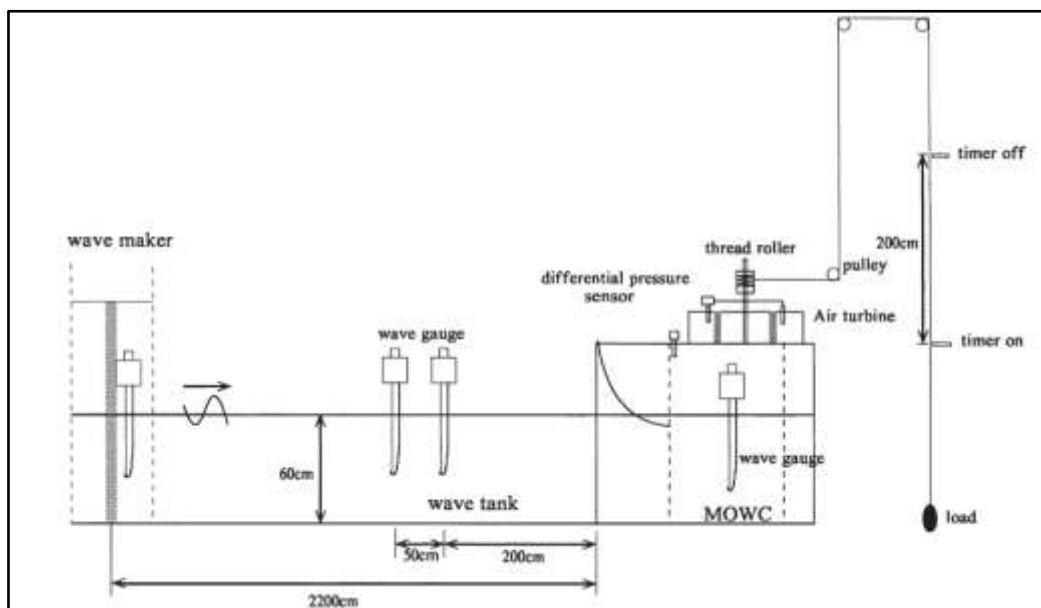


Figure 2-6: Experimental set-up of caisson model and pneumatic power measurement system (Tseng et al, 2000)

In some OWC model tests, the pressure in the air chamber is the sole parameter used to evaluate the operational performance of the WEC. Liu et al (2011) performed wave tank experiments on an OWC caisson model in proposal of a new OWC caisson breakwater, similar to the MOWC. The capture effect and structural stability of the model was determined through the measurement of successive pressures in and on the chamber. Twenty pressure locations on the

model were used for wave pressure measurements on and in the caisson and an extra two pressure transducers determined the air pressure in the air chamber.

Ram et al (2010) performed a peculiar experimental analysis on a fixed OWC model in a two-dimensional wave tank to analyse the air flow characteristics. The airflow patterns were analysed using Particle Image Velocimetry (PIV) of the air chamber, during which no turbine was present. The PIV system utilised in these experimental tests composed of a Diode-Pumped Solid State continuous light laser and a high-speed camera, which captured the effects of the air flow on the imposed particles. Olive oil was the selected compound that was atomised into 1 μm particles and then subjected to the OWC's air flow for analysis. The laser light highlighted the influence of the air flow on the particles, which was subsequently captured on the high speed camera. In addition to the evaluation of the air flow characteristics, the pressure in the specially designed OWC model was measured using a digital Micromanometer. This was performed to measure the changes in pressure through the narrowing air chamber geometry as the air flow oscillated. Figure 2-7 shows the experimental set-up of the PIV measurement system on the OWC model in the wave flume. The results showed that the airflow through the air chamber was much stronger during the compression stage of the air pocket compared to the airflow during the rarefaction stage. Further results revealed the necessity of an air flow regulator due to the low air flow characteristics between the oscillatory stages.

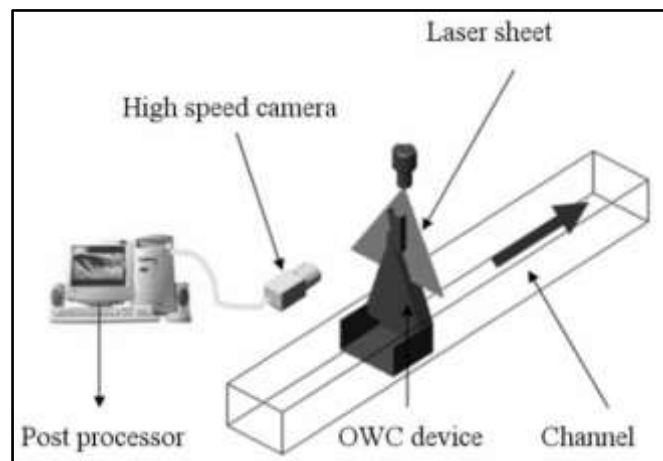


Figure 2-7: Experimental set up of PIV system in the wave flume (Ram et al, 2010)

2.6 Additional air flow measurement techniques

A substantial factor in the volumetric flow rate measurement in an OWC model is the bidirectional and oscillating flow through the air chamber. Therefore for the pneumatic power measurement system, it is necessary to investigate methods for accurately quantifying this air flow.

Jayashankar et al (1997) created a unique probe to measure the variation in air flow velocities into and out of a Well's turbine. These experiments formed part of

WEC studies. The probe comprised of 4 small differential pressure transducers, each being placed at predetermined distances from the end of the probe. The probe allowed radial stagnation pressure measurements of the oscillating air flow, which is essentially the sum of the static and dynamic pressures. Heeley (2005) describes the stagnation pressure to be the pressure when the fluid is decelerated to zero during an isentropic process. For the stagnation pressures to be measured, the probe was aligned so that the transducers faced the air flow. A hole in a common chamber in the probe exposed the transducers perpendicularly to the air flow, which allowed static pressure measurement. Equation 2-15 shows how the air flow velocity in the duct can be calculated from the air density and the measured stagnation and static pressures. Figure 2-8 describes the design of the probe, where S1 to S4 denotes the pressure transducers.

$$p_{stagnation} = \frac{1}{2}\rho v^2 + p_{static} \quad (2-15)$$

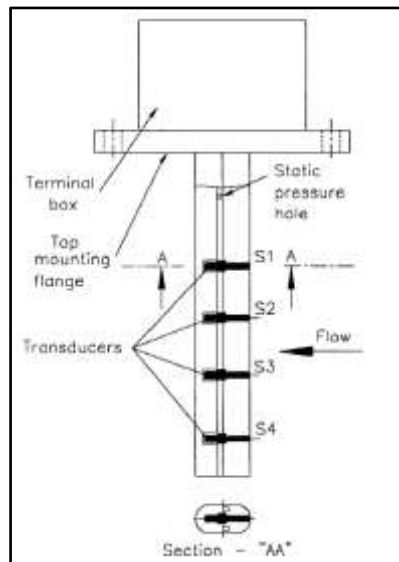


Figure 2-8: Probe design for oscillating air flow velocity (Jayashankar et al, 1997)

The oscillating air conditions for the experimental tests were achieved using a controlled butterfly valve in a blower, which was set at a frequency of 0.1 Hz. The pressure transducers were selected at a measurement range of 2 psi, $\pm 0.1\%$ accuracy and a frequency response of 1 kHz. The frequency response was an especially important factor in this experiment due to the oscillating flows. The 1 kHz specification was sufficient for this application relative to the low frequency air oscillations of 0.1 Hz.

The calibration of the novel probe design by Jayashankar et al (1997) was performed by a pre-calibrated hot wire probe with a constant temperature anemometer (CTA) circuitry. During calibration, the hot wire probe was inserted into the flow, parallel to the probe and placed at the front of each transducer. Measurements were taken during steady flow at three different temperatures, where the air velocities were stepped up from 0 m/s to 35 m/s. During the

testing phase, measurements from the probe were taken for velocities varying up to 35 m/s. The hot wire probe was again used at this stage as a reference anemometer. Test results showed that the designed probe had an accuracy of $\pm 2\%$ with respect to the performed calibration.

Lu and Lau (2008) used the same concept as Jayashankar et al (1997) by measuring the difference between the stagnation pressure and the static pressure to calculate the air flow velocity. They however, measured the bidirectional flow of air at constant air flow rates. The flow sensor was made up of two back-to-back Pitot tubes, where the tube facing the flow measured the stagnation pressure and the tube away from the flow measured the static pressure. A differential pressure transducer computed the difference in these values to obtain the dynamic pressure, from which the air flow velocity could be calculated. It was noted that there is a quadratic relationship between the voltage output from the pressure transducer and the calculated volumetric flow rate.

During the design phase for testing the sensor, variables such as material, sensor placement, pipe dimensions and geometry were all taken into account to improve the accuracy of the transducers readings. The following parameters were maintained during the testing phase:

- The back-to-back Pitot tubes were placed in the centre of the pipe cross section due to it being the point of highest flow stream.
- The tubes were placed as close together as possible to decrease the differences in the static pressure readings during bidirectional flow.
- The inner diameter of the pipe was kept at minimum width so that the flow velocity was increased while also taking into account the losses of air flow through small diameters.

Figure 2-9 shows the design of the flow pipe and the placement method of the bidirectional flow sensor in the pipe.

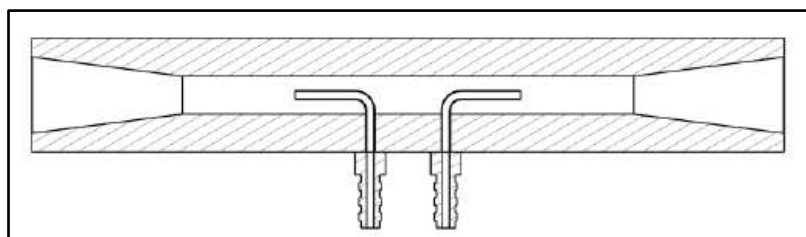


Figure 2-9: Cross-sectional view of the flow pipe design and the Pitot tube placement (Lu and Lau, 2008)

The calibration of Lu and Lau's (2008) sensor was performed against a RespiCal Timeter Calibration Analyser. The calibration allowed a coefficient C to be determined which related the output voltage to the actual flow velocity. Final testing of the bidirectional flow sensor showed that the measurements followed the quadratic relationship for higher flow rates but deviated from the curves during low flow velocities.

The low cost bidirectional air flow sensor was tested to have an accuracy of $\pm 10.4\%$ over an operating temperature of $0 - 50\text{ }^{\circ}\text{C}$. At constant testing temperatures and more precise handling of low flow rates, the sensor would be able to achieve a substantially higher level of accuracy.

In terms of simple volumetric flow rate measurement, Carrington et al (1981) measured the air flow volume from a fined-tube heat exchanger ventilated by fans, through the inflation time of a large polythene film bag. The bag was properly sealed and then attached to the evaporator orifice. The output air flow velocity of the evaporator was also measured in a rectangular duct by a vane anemometer and hot-wire anemometer, which were compared with the results of the polythene film bag tests. Comparative analysis of the results showed that the simple bag tests proved to be within $0.02\text{ m}^3/\text{s}$ range ($\pm 2\%$) of the anemometer results.

2.7 Model testing

The benefit of model testing is that the system at hand can be tested on a smaller scale and the results can be attributed to the full scale system. This proves to be a cheaper and more straightforward method for testing the performance of a system, especially in the case of large designs.

For the application of the pneumatic power measurement system of an OWC model, the dimensions of the full scale prototype would have to be scaled down from the designed dimensions to a suitable scale for the testing environment. On the other hand, a generalised OWC model is implemented in the experimental stage of this research study which could be scaled up to a suitable scale using the scaling laws. This would allow the analysis of the structural dimensions and the pneumatic power capabilities at a prototype level.

2.7.1 Scaling laws

White (2008) states that the flow conditions realised in model testing would be entirely similar if all the applicable dimensionless parameters have the same corresponding magnitudes for the model and the full scale system. Therefore the OWC models must conform to certain scaling laws to ensure that the performance of the air flow in the model is a representation of the full scale system.

These scaling laws pertinent to the model testing in this research study include geometrical similarity and dynamic similarity. Geometrical similarity arises when the structural dimensions of the model and the full scale system in all three coordinates have the same linear scale ratio (White, 2008). This allows the angles and flow directions of the model to be maintained. The OWC models and the designed system would be dynamically similar if they have the same time scale, length scale and mass scale ratio (White, 2008). The dynamic similarity would also

be dependent on the correlation of the Reynolds Number in the model and prototype.

2.7.2 Model testing of OWC designs

Torre-Enciso et al (2009) mentions the model testing that was performed on a three dimensional model of the Mutriku Wave Power Plant. The model tests allowed two selected concepts of the large breakwater structure to be tested in a wave tank. Various sea states were imposed on the structure for the selected location and thereafter the best performing model was chosen.

Two types of model studies were performed for the SWEC. The first was a 1:50 scale model of the system in a two-dimensional wave tank and the second test was performed in a three-dimensional wave tank using a 1:100 scale model. For the three dimensional test, the model was built to incorporate all the facets of the individual models of the designed SWEC including the high and low pressure conduits and valves. These conduits were however placed above-water to allow for easy monitoring of the air flow and to minimise the induced Reynolds scale effects (Retief, 1982). Another important aspect that one has to deal with when it comes to scale models is the scaling of the compressibility of air and its effects. The following section from Retief (1982) gives a brief insight regarding this concern:

“The compressibility of the air contained in the device cannot be scaled. It was found that the compressibility of the contained air did not influence the device’s power conversion capability but merely provided a damping effect on the higher frequency pressure fluctuations in the duct.”

Figure 2-10 shows the assembled three-dimensional model of the SWEC during the model testing studies.



Figure 2-10: Three-dimensional model of the SWEC (Müller & Retief, 2011)

2.8 Resonance

The optimum operation of an OWC system is achievable through the resonant motion of the enclosed water column. The resonance theories below allow the approximation of the resonance frequencies for the constructed OWC model.

McCormick (1981) presents an OWC model based on rigid body theory. The model defines the relationship for the natural frequency of the water column. This is based on the water column free surface being modelled as a piston, while also taking into account the concept of added mass. Equation 2-16 defines McCormick's relationship for the frequency at which resonance occurs, where L_1 is the SWL depth and L'_1 is the water column effective length due to added mass.

$$f_c = \frac{1}{2\pi} \sqrt{\frac{g}{L_1 + L'_1}} \quad (2-16)$$

The second theoretical model considered for the approximation of the natural frequency is an adaption of Evans & Porter (1995) model, developed for a larger oscillating water column by Veer & Thorlen (2008). This model takes into account the cross sectional area of the water which plays a role in the resonance estimation especially for devices with particularly larger water columns. Equation 2-17 gives the natural frequency approximation for this adapted theoretical approximation.

$$f_c = \frac{1}{2\pi} \sqrt{\frac{g}{L_d + 0.41S^{1/2}}} \quad (2-17)$$

Where L_d is the draught length of the water column (assumed as the water depth) and S is the cross sectional area of the water column.

The final model, described by Horko (2007), is an adaption from McCormick's discussion on the natural heave period of an undamped floating body. A piston analogy is used to approximate the natural frequency of an OWC device with a solid back wall. Equation 2-18 gives the relationship for this adapted approximation.

$$f_c = \frac{1}{2\pi} \sqrt{\frac{g}{d_{lip} + \frac{\pi B}{2}}} \quad (2-18)$$

Where B is the breadth of the water column.

Additionally, Evans & Porter (1995) proposes the theory where resonance is achieved when the ratio of water column width and lip submersion depth is minimised, which allows the water column to act more like a rigid body. Evans & Porter (1995) found that the larger the water column width, the lower the natural frequency found in the OWC.

2.9 Conclusion

The literature survey has presented vital information regarding an OWC device's operation in the presence of water waves and introduced existing OWC designs pertinent to this research study. The technology that has been utilised for pneumatic power measurement in OWC models and air-flow measurement in other applications has been investigated in detail. Relevant descriptions regarding scale model testing and resonance theories have also been described.

Previous research into the air-flow measurement in OWC devices and other applications has introduced methods such as back-to-back pitot-tube measurement, air rotameters and calibrated filters. It was established that the use of the water column velocity for the volumetric flow rate measurement of air was inaccurate due to air compressibility effects.

Literature studies showed that the techniques used for the pressure drop measurement were more of a mutual approach than those found for the volumetric flow rate measurement. These techniques include digital micromanometers, differential pressure transducers and gauge pressure transducers.

3. Development of the pneumatic power measurement device

The design of the pneumatic power measurement device is based on the characteristics of the volumetric flow rate of air and air pressure in an OWC device, which was documented in the literature studies. This chapter describes the concept designs, final design, construction and assembly of the pneumatic power measurement device from the concept to the final product stages.

3.1. Concepts for measurement device

As mentioned before, the measurements required for the calculation of the pneumatic power of an OWC device is the pressure drop over an orifice and the volumetric flow rate of air through the orifice. After the completion of the literature studies, it is evident that the measurement of the volumetric flow rate is the main concern and not the air pressure measurement which is more of a standard selection procedure. The volumetric flow rate of air in OWC devices are both unsteady and bidirectional which limits the types of flow meters one can apply to the model to ensure accuracy of the pneumatic power measurement.

Other factors which would affect the accuracy of the pneumatic power measurement are the range of the instrument, the frequency response, the percentage error and the type of output signal from the device. These additional factors will be dealt with later in this chapter and in chapter 5.

3.1.1. Volumetric flow rate measurement

Figure 3-1 was developed through the investigation of the various types of flow meters to help identify the correct equipment for the volumetric flow rate measurement. Hayward (1979) and Figliola & Beasley (2006) were used to generate a complete list of flow meters that could be utilised for the volumetric flow rate measurement of air. In addition to unsteady and bidirectional flow suitability, the air-flow meter would also have to be easily integrated with the OWC device.

The turbulent flow of air through an OWC device is categorised by the Reynolds number R_e defined by equation 3-1. This dimensionless number describes the flow in terms of a ratio of the inertial forces to the viscous forces of a fluid. Therefore a high Reynolds number indicates a dynamic fluid which is turbulent and a low Reynolds number describes a fluid where the viscous forces prevail; thereby being a laminar fluid. Turbulent flow takes place when the flow regime has a Reynolds number greater than 2000 and laminar flow would be categorised by a Reynolds number less than 2000.

$$R_e = \frac{\rho V D_p}{\mu} \quad (3-1)$$

Where V is the mean velocity, D_p is the pipe diameter and μ is the viscosity of the fluid.

The air-flow meters that are available on the market are usually available to cater for measurement in steady state conditions. Steady state conditions take place when the air-flow is unidirectional and flows with a constant velocity. The instruments that measure bidirectional and turbulent flow are highly specialised for their applications and tend to be expensive. Figure 3-1 gives a breakdown of the various types of flow meters that fall under turbulent air-flow measurement as well as a further classification level of the equipment that can be manipulated to measure bidirectional air-flow. Figure 3-1 makes it possible to eliminate the strictly unidirectional devices from the selection procedure.

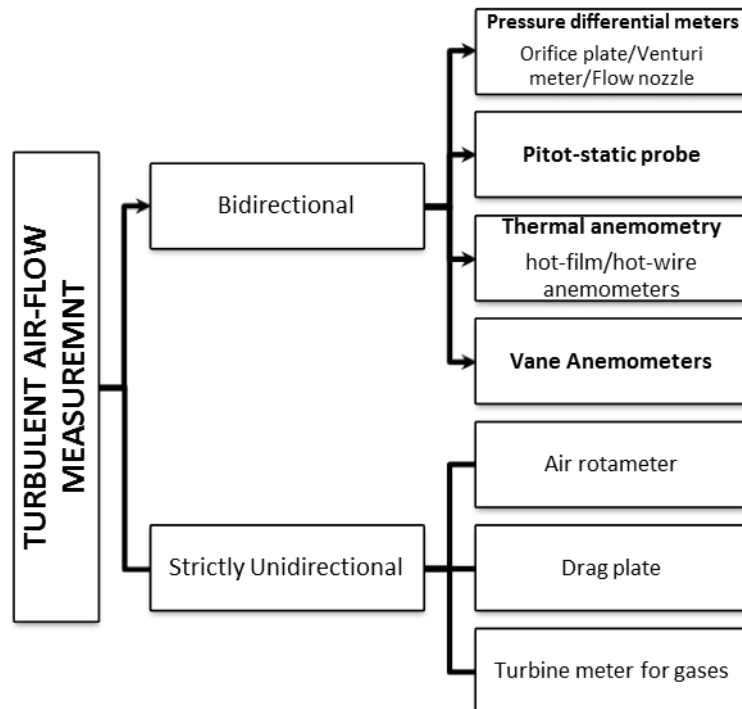


Figure 3-1: Selection diagram for the air-flow meter

The air-flow measurement instruments that were shortlisted for the concept designs as part of the pneumatic power measurement device were pressure differential meters, pitot-static probes, thermal anemometers and vane anemometers. The idea behind these selections was due to their potential ability to measure turbulent and bidirectional air-flow. The applicable list of air-flow meters that fall under the pressure differential meters category are the obstruction meters which are in-line volumetric flow rate meters that measure the pressure difference over a portion of its structure which is relative to the volumetric flow rate of the fluid. The air-flow velocity from a pitot-static tube is calculated from the dynamic pressure, which is derived from the stagnation and static pressure measurement. This instrument can also be applied to bidirectional flow systems by utilising two of these instruments in a back-to-back manner as performed by Lu and Lau (2008). The suitable flow meters from the thermal anemometers category are the hot-film and hot-wire anemometers. They work in the same manner where they measure the flow velocity of the air by the proportional heat

loss over its resistive element (hot-film or hot-wire) which is placed in the flow stream. Hot-film and hot-wire anemometers are not sensitive to the direction of the air-flow due to cooling of the resistive element taking place regardless of the direction of flow. Specialised instruments of this category are able to output an analog signal indicating the direction of the flow. The final instrument category for the concept design stage was the vane anemometer. These anemometers comprise of a rotating fan placed in the air-flow which outputs an electrical signal dependent on the speed of the fan.

From the selected concept designs for the volumetric flow rate meter, the advantages and disadvantages of the concept design instruments had to be weighed against each other for a final selection to be made. The sub-category of obstruction meters was the chosen flow meter classification due to its ability to be constructed (machined) according to a specific design that can be incorporated with the designed OWC model. These types of flow meters are also simple in design where there are no moving parts to facilitate malfunctions and there are a substantial amount of codes of practice to aid in the design of the flow meter (Hayward, 1979). The reasons for the other three concept designs not being chosen are highlighted in Table 3-1.

Table 3-1: Reasons for non-selection of the concept flow meters

Flow meter	Reasons for not being selected
Pitot-static tubes	The tube design results in a delay with the bidirectional measurement. The range of these devices is limited due to inaccuracies at low air velocities (Hayward, 1979)
Thermal anemometers	Recalibration of the probes necessary if accurate data is needed
Vane anemometers	Inertial losses are present during variation of fan rotation in bidirectional flow measurement

The three obstruction meters that can be used for flow measurement are orifice plates, flow nozzles and venturi flow meters. The use of flow nozzles cannot be incorporated into bidirectional flow systems and were therefore excluded from the selection process. Orifice plates are circular plates with an orifice (usually square-edged orifice) in its center. The plates are inserted in pipes where the orifice is concentric with the pipe inner diameter. Venturi flow meters are made of a converging pipe section to a throat section and then a diverging pipe section away from the throat. Figure 3-2 shows the pressure losses of the three obstruction meters as a function of their openings (orifices). It can clearly be seen that for the range of opening percentages, the Venturi has a much lower permanent pressure loss than the square-edged orifice plate due to the gradual design of the Venturi flow meter. The β value is a contraction ratio of the obstruction meter's orifice diameter to the entrance duct diameter.

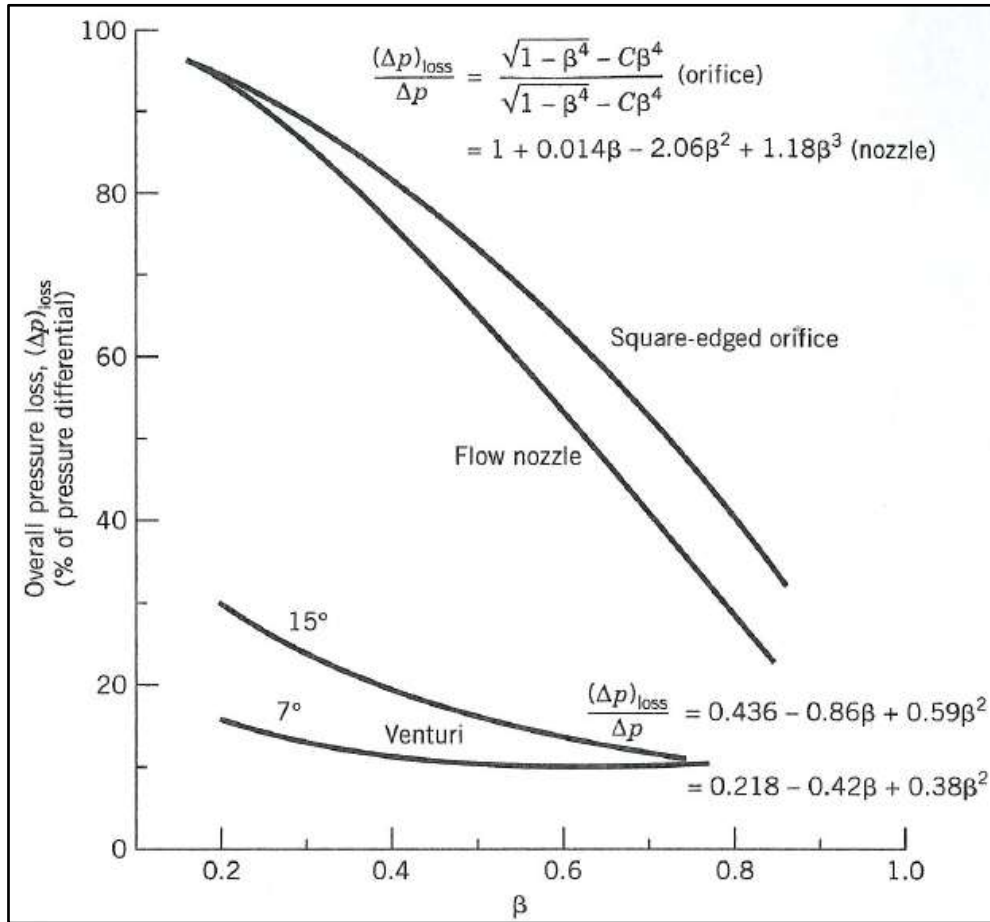


Figure 3-2: Permanent pressure loss for the obstruction flow meters (ASME, 1971)

The final selection of the specific flow meter type from the pressure differential meter category for the volumetric flow rate measurement for the pneumatic power measurement device was the venturi flow meter. This selection was primarily based on the venturi flow meter's relatively low pressure head loss.

3.1.2. Pressure measurement

Pressure measurement for calculating the pneumatic power is required in two scenarios. First is the measurement of the pressure drop over which the volumetric flow rate of air is measured and second is the pressure measurement in the selected venturi meter to calculate the volumetric flow rate of air through the OWC model. For this pressure measurement to be acquired, a suitable pressure transducer is required.

A pressure transducer converts a mechanical measurement into an electrical signal through the deflection of an elastic element such as a diaphragm or Bourdon tube. Pressure transducers are required in the physical experiments for their electrical output signal due to the recording of data during experiments, which is analysed later. The type of pressure transducer that is most commonly found on the market is the strain-gauge (diaphragm) based transducer, which has a

strain-gauge attached to a diaphragm and subsequently forms part of a Wheatstone bridge circuit. If the pressure in the system is increased, the diaphragm expands, deflecting the strain-gauge, resulting in a proportional voltage output signal. Figure 3-3 shows a schematic diagram of a diaphragm pressure transducer with the resistance strain gauges on the diaphragm.

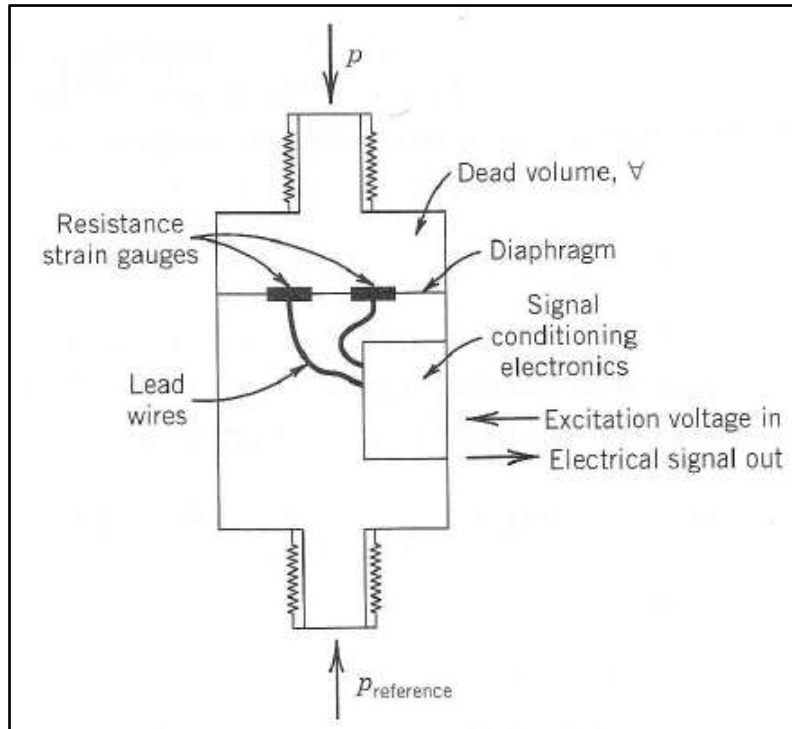


Figure 3-3: Sensing schematic of a diaphragm pressure transducer (Figliola & Beasley, 2006)

The considerations for the pressure measurement in an OWC model are two-fold. First is the location of measurement and second is pressure measurement scale required from a transducer. For the pressure drop measurement, the most common and practical position to perform measurements is on an OWC device's air chamber due to the pressure drop between the air chamber and the atmosphere, over the orifice, being the determining measurement in calculating the pneumatic power. Investigating the different possible pressure measurement locations aids the process of choosing which pressure measurement scale to use. Figure 3-4 below shows where possible pressure measurement can be performed on an OWC model. These include A – pressure difference between the air chamber and the atmosphere, B – pressure drop over the orifice, C – hydrostatic pressure to determine the water column height and D – the sea bed pressures from the incoming wave energy. To focus this research on the pneumatic power derived from the air chamber, only pressure measurements noted as A and B from Figure 3-4 will be taken into account. The water column height can be measured by available wave probes instead of using pressure transducers, which will be explained in chapter 5. Pressure measurement locations for the venturi meter will be explained in detail in the following sections.

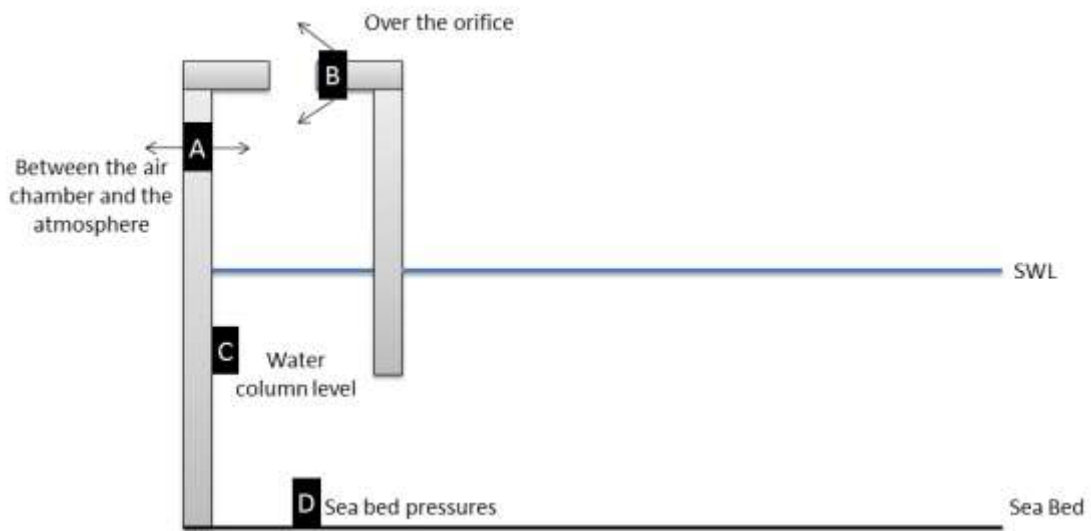


Figure 3-4: Possible pressure measurement locations (Islay Limpet Wave Power Plant, 2002)

The possible pressure transducer measurement scales are listed in Table 3-2. In terms of the pressure measurement for the pressure drop over an OWC model, either one of the three types of pressure measurement scales can be used. For the venturi meter, the first thought would be to use a differential pressure transducer to calculate the volumetric flow rate between the pressure differentials of the bidirectional flow. The problem arises in the tubes leading up to the differential transducer because there would be a substantial dead volume in the length of the connecting tubes for this OWC system application. This would result in delays in the capturing of measurements, consequently allowing inaccuracies in the measurements. This is especially pertinent since it is an unsteady system. Therefore for the pressure measurement in the venturi meter, an absolute pressure transducer or preferably a gauge pressure transducer is required so that the pressure measurement point is as close to the air-flow as possible. It has been noted that gauge pressure transducers are sometimes installed using connecting tubes but these transducers are not considered for this application.

Table 3-2: Description of the different pressure measurement scales

Pressure Measurement	Description
Absolute	Measured relative to the absolute zero pressure
Gauge	Measured relative to a certain absolute reference pressure (usually ambient pressure).
Differential	Difference in pressure between the two points in the system

Pressure measurements can be performed at three levels; total pressure, dynamic pressure and static pressure measurement. For the pressure variations in the air chamber of the OWC, the static pressure is used for the pressure drop

measurement. Fox et al (1999) state that the static pressure is the pressure that would be measured by an instrument moving with the air- flow; hence it would be measured perpendicular to the flow.

Although pressure measurement is only used for the pneumatic power measurement in this research, it must be noted that submersible pressure transducers can be utilised to measure the hydrodynamic pressure in the water column and measure the height of the oscillating water column.

3.2. The venturi flow meter

3.2.1. Design of the venturi flow meter

Since the standard venturi flow meter is normally used for unidirectional flow measurement, the design had to be altered according to the application with an OWC device. The typical design of the venturi shown by Figure 3-5 has a convergent section and a divergent section joined to a throat. The convergent entrance from the duct to the throat causes the pressure drop ($p_1 - p_2$) which measures the volumetric flow rate and the divergent outlet recovers the air pressure downstream on the way out of the flow meter. Thus there is a directly proportional relationship between the pressure drop and the ratio of the throat area over the duct area.

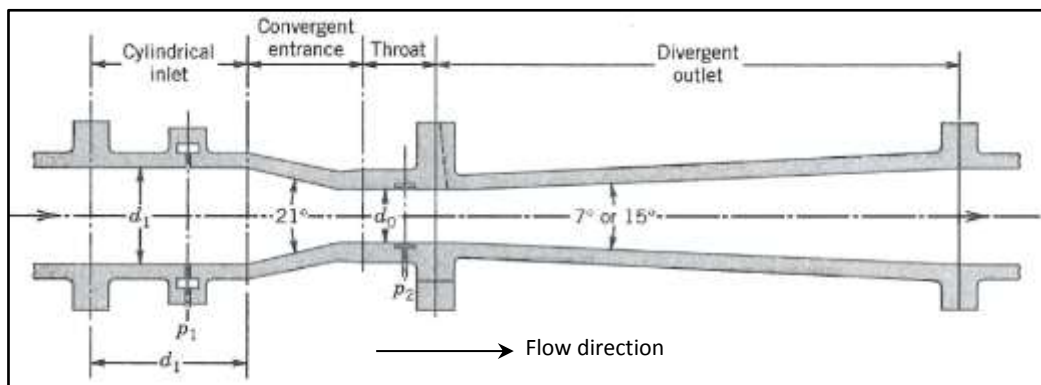


Figure 3-5: Typical layout of a venturi flow meter (Figliola and Beasley, 2006)

The design of the venturi flow meter as the volumetric flow rate meter in the pneumatic power measurement device is based on manipulating the original design by making it symmetrical for the bidirectional measurement. The subtended angle for the convergent section is usually 21° to ensure a high acceleration of the air-flow and for the divergent section it is between 7° to 15° depending on the pressure recovery desired. An equilibrium point of the subtended angles between the typical venturi meter design and the bidirectional venturi meter design had to be found for the new design. The notion behind this decision was to choose a midpoint between a high pressure drop (21°) and a maximum pressure recovery (7°). As a result, the subtended angle for the convergent and divergent sections of the bidirectional venturi flow meter was designed to be 14° .

The beta value β from Figure 3-2 determines the area ratio of the throat of the venturi flow meter to the air-duct. According to the venturi meter standards (ISO 5167-1:1991) the range of the beta value is 0.4 to 0.75 and it is used to determine the throat diameter d_t through equation 3-2. The predetermined inner diameter of the duct D_d is 0.14 m, calculated using a desirable area ratio between the duct area and the OWC model's air chamber area. Using equation 3-2, the inner diameter of the throat is calculated to be $d_t = 0.056$ m. The length of the throat is kept the same as the inner diameter of the throat.

$$\beta = \frac{d_t}{D_d} \quad (3-2)$$

Figure 3-6 shows the computer-aided design (CAD) drawings and the dimensions of the designed bidirectional venturi meter. The top left block is a single section of the venturi meter which is duplicated and joined by a flange to form the full venturi meter. The air-ducts joining the venturi meter to the OWC model and also joining it from the atmosphere to the venturi meter were designed to be greater than the standard entrance cylinder length prescribed by ISO 5167-1:1991.

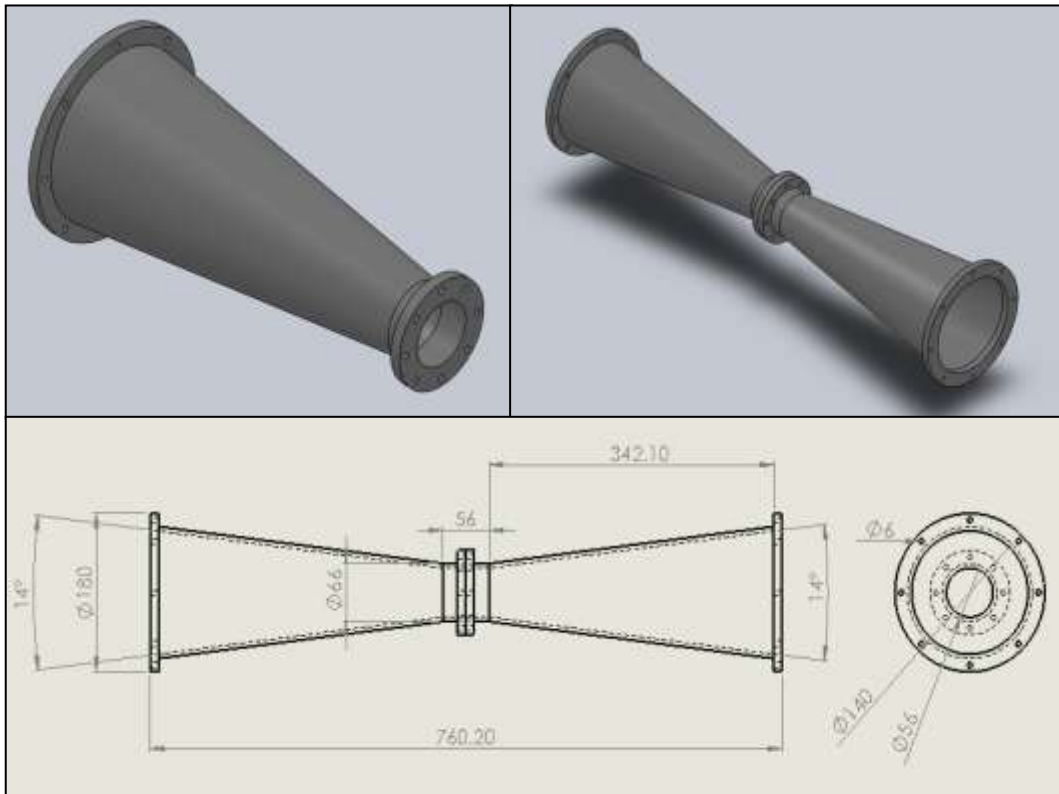


Figure 3-6: Design and dimensions of bidirectional venturi flow meter (dimensions in mm)

Equation 3-3 describes the non-linear relationship between the volumetric flow rate Q of air and the pressure drop $\Delta p_{i,o}$ in the venturi flow meter. The coefficient of discharge C_d is a correction factor for the measured flow rate which is determined during calibration. The square relationship shown by equation 3-4 results in inaccurate readings at low volumetric flow rates due to the pressure

drop being close to zero for a range of low flow rates (red block in Figure 3-7). These inaccuracies had to be catered for by an additional flow meter to measure the volumetric flow rate accurately at low flow rates. The chosen flow meter would have to be placed at the throat of the venturi where the air-flow velocities are the highest.

$$Q = C_d A_d \sqrt{\frac{2\Delta p_{i,o}}{\rho(t) \left(\left(\frac{A_d}{A_t} \right)^2 - 1 \right)}} \quad (3-3)$$

Where, A_d is the area of the air-duct
 A_t is the throat area of the venturi flow meter
 $\Delta p_{i,o}$ is the pressure drop between the air-ducts and the throat

$$Q^2 \propto \Delta p \quad (3-4)$$

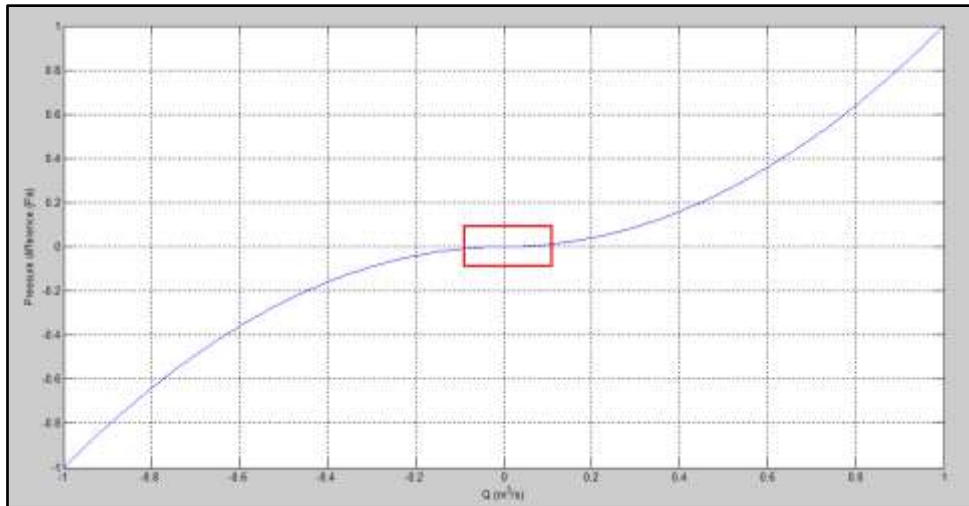


Figure 3-7: Non-linear relationship between volumetric flow rate and pressure drop in differential pressure flow meters

A decision was made for a hot-film anemometer to be incorporated with the venturi flow meter because it has a linear relationship between the output voltage and the air-flow velocity, a high frequency response to suit the oscillations of the air-flow in an OWC model and has a small probe which can be easily incorporated into the designed venturi flow meter. The main reason for selecting a hot-film anemometer over a hot-wire anemometer is due to its rugged nature and its ability to survive in turbulent flow environments (Figliola & Beasley, 2006). Brumbley and Arbas (1979) concluded that there is frequent damage to a hot-wire sensing probe when it is exposed in turbulent flow.

The hot film anemometer operates through a resistive temperature device (RTD), which is part of one leg of a Wheatstone bridge circuit, being placed in the flow stream. The probe of the hot-film anemometer has the RTD (filament) at its tip which is inserted into the air-flow stream. Most thermal anemometers utilise the CTA circuitry which defines its operation. When there is no air-flow, the bridge is

in equilibrium; therefore no voltage difference across its diagonal. When the air-flow velocity increases, the filament resistance tends to decrease resulting in an error signal from the bridge balance, which is sent to the current regulating amplifier. Consequently, the current in the circuit is increased which heats the hot-film filament and increases its resistance until balance is restored on the bridge. The voltage drop across the Wheatstone bridge represents the hot-film probe's current. The heat loss from the RTD is directly proportional to the squared output voltage which is used to determine the air-flow velocity (Jorgensen, 2002).

3.2.2. Construction and assembly

The bidirectional venturi flow meter was machined in the mechanical workshop at Stellenbosch University. The material used to construct this flow meter is polyvinyl chloride (PVC) since it can be machined quite easily to a smooth finish for minimal friction losses during use. The design of the venturi flow meter as two symmetrical pieces facilitated the machining process by allowing the machining tool to easily reach each section of the venturi meter especially the small diameters of the throat. Additionally, it ensured that each piece was smoothly machined to an acceptable level.

The two symmetrical pieces of the venturi flow meter were joined together by the designed flanges and fixed together using M6 bolts. To ensure that the flange connections were airtight, black gasket silicone was placed in between the flanges before they were joined.

The air-ducts leading from the OWC model to the venturi and then from the venturi to the atmosphere were Perspex cylinders, ordered as off-the-shelf components. Flanges were machined from sheets of Perspex and glued to the air-ducts using Tensol™ no. 17 adhesive. The flange connections made it easy to assemble the venturi meter as a full-length system and join it to the OWC model's roof. The full venturi meter with the air-ducts would stand vertically on top of the roof of the OWC model during the wave flume experiments. Figure 3-8 shows an image of the constructed and assembled venturi flow meter, attached to the air-ducts and the roof of the OWC model by means of flange connections.

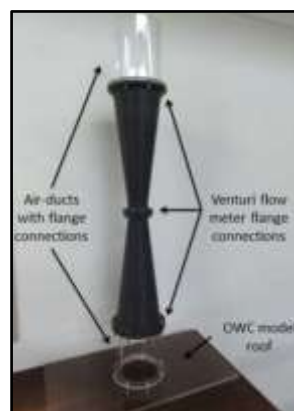


Figure 3-8: Image of venturi flow meter with attached air-ducts and OWC model roof

The pressure tapings for the pressure measurement were holes of diameter 4.5 mm (ISO 5167-1:1991). The pressure connections over the pressure tapings were machined from small PVC blocks. The connections were machined with a center hole, threaded to the size specified by the selected pressure transducers. The curvature of the air-duct and the venturi throat were machined at the bottom-end of the connections so that they could be glued to the device. Clear epoxy adhesive was used to glue the connections to the venturi and the air-ducts. Figure 3-9 illustrates the pressure transducer connections on the venturi flow meter system.

3.2.3. Measurement locations

The set locations for the pressure differential measurement of the bidirectional venturi meter were at the two air-ducts and at the throat (Figure 3-9). The distance of the pressure tapping from the convergent section of each air duct was set at half the inner diameter of the duct D_d which is 0.07 m (ISO 5167-1:1991).

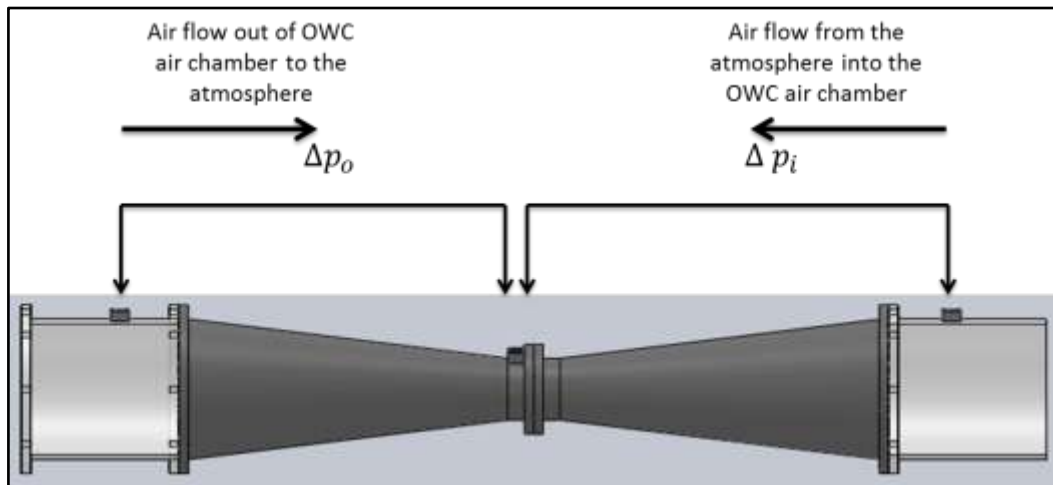


Figure 3-9: Horizontal layout showing the pressure tapings on the venturi flow meter

3.3. Summary of equipment required

The details of the measurement equipment required for the pneumatic measurement device will be specified in chapter 5. The following information is a summary of the equipment type and quantity that was needed for the complete pneumatic power measurement device.

The venturi flow meter required 3 gauge pressure transducers to measure the pressure drops in the venturi due to the compression and expansion of the air chamber. A hot-film anemometer with a small probe diameter was needed for insertion into the throat of the venturi flow meter.

For the measurement of the air-chamber pressure, a gauge or differential pressure transducer was required for direct placement onto the OWC model.

Hayward (1979) mentions five important factors to pay attention to when selecting the measuring equipment for experiments.

The five factors are:

1. Accuracy
2. Repeatability
3. Linearity
4. Discrimination
5. Range and Rangeability

Accuracy and repeatability are related in the sense that if measurements are accurately performed, they are repeatable, but saying they are repeatable does not necessarily mean they are accurate. Linearity is the extent to which the calibration curve of an instrument deviates from the best fit straight line. Discrimination is a measure of the resolution of an instrument. Range and rangeability describes the measurement range within which the results have an acceptable level of accuracy. Frequency response times should also be added to the factors, especially in the case of this research where sufficient response to the air-flow oscillations are mandatory.

3.4. Conclusions

This chapter provides the details behind the development of the pneumatic power measurement device from the concept stages to the final assembled system. Relevant literature on the experience with working with various flow meters and pressure transducers helped in the decision making process. International standards also facilitated the design of the venturi flow meter. The bidirectional venturi flow meter is essentially the pneumatic power measurement device because it can measure both the pressure drop over its throat and the volumetric flow rate of the bidirectional air-flow to calculate the pneumatic power.

4. Simulation of the pneumatic power from an OWC model

This chapter of the thesis describes the analytical model of the air chamber's operation and the pneumatic power in an OWC model. The three models described in this chapter define an OWC model with a closed roof, a roof with an orifice and lastly the primary model which describes an OWC model with the designed venturi flow meter on its roof.

The aim of the simulated models is to predict the air chamber pressures and the pneumatic power as a result of the OWC model's operation. The forcing function of the air chamber, which is the water column displacement, is modelled as a sinusoidal wave to facilitate the operation of the simulation models. The idea behind this forcing function is that it acts as a piston which compresses and expands the air chamber as the water column oscillates. The assumption for the water column acting as a piston is that it maintains a plane surface during operation. The experimental recordings of the water column displacement are additionally used as an input to the forcing function in the simulation model. Details of these tests are documented in chapters 5 and 6. Factors such as reflection and diffraction of waves were ignored for all the models to simplify the simulations.

The simulated models were used in the comparative analysis with the results obtained from the testing of a pneumatic power measurement device. The air-flow models were derived using the theoretical methods of Holtz (2007) which he used for the modelling and design of an air-spring for a suspension seat. These methods make use of the ideal gas law and the first law of thermodynamics to obtain state equations for the air chamber oscillations. Detailed derivations of the three air-flow models are described in Appendix A.

4.1. Design of OWC model

For the application of the air-flow model, a simple OWC device needed to be designed so that it could be easily implemented in the air-flow models. Figure 4-1 shows the basic design of the OWC model. The 'box' design was chosen for the OWC model due to it being the easiest to apply in a simulation environment and replicate it as a constructed OWC model during wave flume experiments. Previous research on wave flume experiments has also revealed the use of this simple 'box design'. The exact dimensions of the OWC model used for the wave flume experiments are detailed in chapter 5.

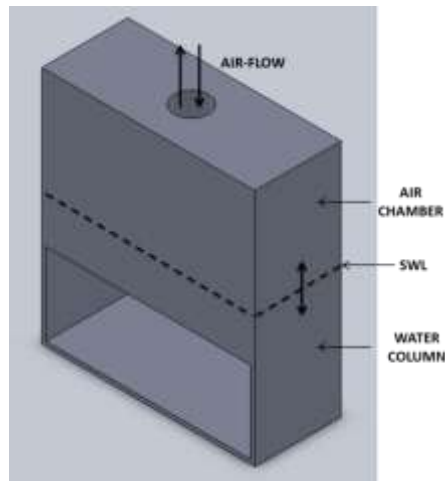


Figure 4-1: CAD drawing of the simple OWC model design (SolidWorks, 2010)

4.2. Laws of fluid mechanics

4.2.1. Ideal gas law

Gases which obey ideal gas behaviour are ones where the particles only exhibit elastic collisions and where no intermolecular forces are present. These criteria would be followed when the gas pressures are substantially lower and temperatures are substantially higher with respect to the critical points. The critical points for ideal gas behaviour are the critical pressure $p_{cr} = 3.77$ MPa and the critical temperature $T_{cr} = 132.5$ K. All applications of the air-flow models are considerably below critical pressure and above critical temperature; therefore the ideal gas law could safely be applied.

The ideal gas law combines the relationship between the pressure p , the volume v and the temperature T of a gas given by the equation of state for an ideal gas in equation 4-1. This equation of state of an ideal gas shows that the pressure p and volume v are directly proportional to the temperature T .

$$pv = mRT \quad (4-1)$$

Where:

p	is the absolute gas pressure	(Pa)
v	is the gas volume	(m ³)
m	is the mass	(kg)
R	is the Universal gas constant	(J/kg.K)
T	is the gas temperature	(K)

4.2.2. First law of thermodynamics

The first law of thermodynamics describes the conservation of energy for a system and is used in the energy balance to find the theoretical pneumatic power

in an OWC models. Fox et al (1999) state the first law of thermodynamics as equation 4-2.

$$\dot{Q} - \dot{W} = \left(\frac{dE}{dt} \right)_{system} \quad (4-2)$$

Where, \dot{Q} is the rate of heat transfer into the system
 \dot{W} is the rate of work done by the system

4.3. Air-flow models

The first model is a closed chamber model where the OWC model has no orifice on its roof; hence there is no mass flow of air in the chamber. The second model describes the OWC model with an orifice of a chosen diameter and the last model has the pneumatic power measurement device connected to the orifice. All the models are predicted to be adiabatic since the perspex structure is assumed to be a good insulator, the frequency of oscillations are rapid enough not to allow temperature changes or when there is air-flow, the temperature in the box does not vary.

4.3.1. Constants

The constants that are used in the three air-flow models are listed in Table 4-1. A design ambient temperature condition of 15°C was chosen since it was the actual ambient temperature of the wave flume building during experimental testing.

Table 4-1: Constants used for the air-flow models

Description	Constant	Value	Units
Universal gas constant	R	287	J/kg.K
Specific heat at constant pressure	C_p	1,005	J/kg.K
Specific heat at constant volume	C_v	718	J/kg.K
Ambient Temperature @ 15°C	T_a	288	K
Atmospheric Pressure @ 15°C	P	101,325	Pa
Density of air at ambient conditions	ρ	1.23	kg/m ³
Viscosity of air at ambient temperature	μ	1.79E-5	N.s/m ³

4.3.2. Closed-roof OWC model

The closed chamber model (model 1), shown in Figure 4-2, describes the generalised design of the OWC model, where the roof of the structure has no orifice for the mass flow of air. The control volume 1 (CV₁) represents the oscillating air chamber of the OWC model. Model 1 denotes the scenario where the maximum damping level is imposed on the air chamber. However, the damping level is not catered for in this model.

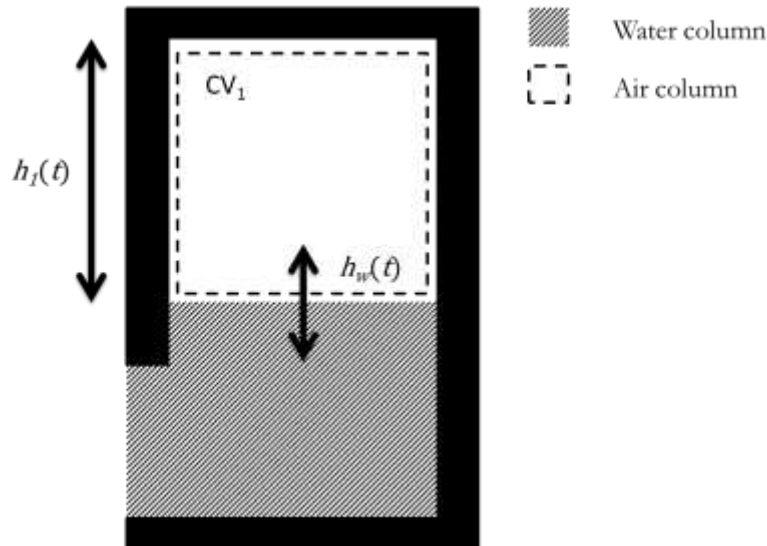


Figure 4-2: Sectional view of the closed chamber OWC model

Where: $h_1(t)$ is the air chamber length

$h_w(t)$ is the water column displacement

The assumptions for the theoretical analysis of this model are as follows:

- The system is adiabatic and reversible (i.e. isentropic)
- The air of the OWC model's air chamber is treated as an ideal gas
- There are no losses due to friction

For the closed chamber model of CV_1 , the theory of continuity of mass is applied. Since no mass flow rate will be present in this model the following continuity of mass is known:

$$\frac{dm_1}{dt} = \dot{m}_{1,in} - \dot{m}_{1,out} = 0 \quad (4-3)$$

$$\text{Therefore, } \dot{m}_1 = 0 \quad (4-4)$$

Using the ideal gas law of equation 4-1 on CV_1 , the rate of air pressure change can be described from equation 4-5.

$$\dot{p}_1(t) = \frac{\dot{m}_1(t)RT_1(t)}{A_1h_1(t)} + \frac{m_1(t)RT_1(t)}{A_1h_1(t)} - \frac{h_1(t)p_1(t)}{h_1(t)} \quad (4-5)$$

The energy balance for the closed chamber system can be solved by applying the law of conservation of energy.

$$E(t) = Q(t) - W(t) \quad (4-6)$$

The state equation for the rate of pressure change in the air chamber is simplified to:

$$\dot{p}_1(t) = - \left[1 + \frac{R}{c_v} \right] \frac{\dot{h}_1(t)p_1(t)}{h_1(t)} \quad (4-7)$$

The following table (Table 4-2) describes the state equations defined for model 1.

Table 4-2: State equations for model 1

State equations for the model 1	
Pressure	$\dot{p}_1(t) = - \left[1 + \frac{R}{c_v} \right] \frac{\dot{h}_1(t)p_1(t)}{h_1(t)}$
Air chamber height	$h_1(t) = L_a - h_w(t)$
	$h_w(t) = A \sin \omega t$ $L_a =$ Initial height of air chamber $A =$ Amplitude of water column displacement
Air chamber speed	$\dot{h}_1(t) = -A\omega \sin \omega t$
States	$\dot{p}_1(t), h_1(t), \dot{h}_1(t)$

4.3.3. OWC model with an orifice

The second model (model 2) describes a general OWC model with an orifice on its roof as shown in Figure 4-3. The two control volumes which are analysed in this model are the air chamber, represented by control volume 1 (CV₁) and the orifice volume, represented by control volume 2 (CV₂). The air chamber has an area A_1 and the orifice has an area A_2 . The diameter of the orifice determines how much damping is placed on the volumetric flow rate of air into and out of the chamber. The size of the orifice can be varied to determine the level of damping due to viscous losses at the orifice (Evans & Porter, 1995).

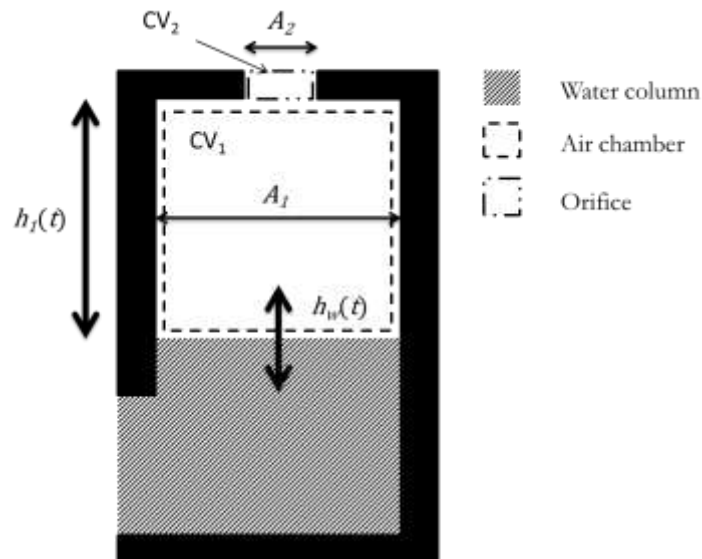


Figure 4-3: Diagram of the OWC model with an orifice on the roof

The assumptions for the theoretical analysis of this model are as follows:

- The system is adiabatic and reversible (i.e. isentropic)
- The air of the OWC model's air chamber is treated as an ideal gas
- Mass flow of air present in the model
- There are no losses due to friction
- Unsteady flow

For CV₁, the theory of continuity of mass is applied.

$$\text{Expansion of air pocket: } m_i = \Delta m_{cv1} \text{ or,} \quad (4-8)$$

$$\text{Compression of air pocket: } -m_o = \Delta m_{cv1} \quad (4-9)$$

$$\text{Therefore, } \frac{dm_{cv1}}{dt} = \pm \dot{m}_1 \quad (4-10)$$

Equation 4-5 is derived again by differentiating the ideal gas law and using the new continuity of mass relation for model 2.

Examining the law of conservation of energy from equation 4-6, $E(t)$ is the energy of the system which is the internal energy $U(t)$ summed with the energy of the mass that is exchanged from the control volume ($\Delta E(t)$).

The law of conservation of energy now becomes:

$$U(t) - \Delta E(t) = Q(t) - W(t) \quad (4-11)$$

$$\text{Where: } U(t) = m_1(t)C_v\Delta T_1(t) \quad (4-12)$$

$$\Delta E(t) = \Delta m_1(t)C_pT_1(t) \quad (4-13)$$

$$Q(t) = 0 \quad (4-14)$$

$$W(t) = p_1(t)A_1\Delta h_1(t) \quad (4-15)$$

Substituting these terms into the energy balance equation and solving for the rate of temperature change enables the simplification of the state equation for pressure.

$$\dot{p}_1(t) = \left[1 + \frac{C_p}{C_v}\right] \frac{\dot{m}_1(t)p_1(t)}{m_1(t)} - \left[1 + \frac{R}{C_v}\right] \frac{\dot{h}_1(t)p_1(t)}{h_1(t)} \quad (4-16)$$

The energy equation for pipe flow derived from equation 2-8 is applied to CV₂ to determine the mass flow rate of air through the orifice.

$$\frac{p_1 - p_2}{\rho g} + \frac{\Delta(V^2)}{2g} + \Delta z = h_L \quad (4-17)$$

Since the change in kinetic energy $\Delta(V^2)$ and potential energy Δz in the orifice (CV₂) is small compared to the pressure difference over the orifice, they will be

omitted from the energy equation. The thickness of the orifice is small relative to the size of the air chamber therefore it is assumed that the air-velocity through the orifice volume V_2 is constant. The energy equation simplifies to equation 4-18, where the pressure p_2 is signified by the atmospheric pressure p_a .

$$h_L = \frac{p_1 - p_a}{\rho g} \quad (4-18)$$

The head losses h_L of the air-flow comprises of the major and minor losses.

$$h_L = h_{L,major} + h_{L,minor} \quad (4-19)$$

$$h_{L,major} = f \frac{L_{duct}}{D_2} \frac{V_2^2}{2g} \quad (4-20)$$

$$\text{Where,} \quad f = \frac{1}{\left[-0.86 \ln \frac{\varepsilon}{3.7 D_2}\right]^2} \quad (4-21)$$

The major losses for this model of the OWC model will be negligible due to the roughness ε of the OWC model's design material (perspex) being zero (Çengel & Cimbala, 2010). On the other hand, the minor losses are applicable for the contraction losses K_c and expansion losses K_e of the air-flow into and out of the orifice volume (CV₂). An additional loss coefficient, the auxiliary losses K_{aux} , is introduced into the minor losses equation to account for differences between the simulated and experimental results. Holtz (2007) used this additional loss coefficient to accommodate the unknown losses through the flow restriction of the orifice.

$$h_{L,minor} = K_c \frac{V_2^2}{2g} + K_e \frac{V_2^2}{2g} + K_{aux} \frac{V_2^2}{2g} \quad (4-22)$$

The energy equation can now be used to find an expression for the air-velocity through CV₂.

$$V_2 = \sqrt{\frac{|p_1 - p_a|}{\rho(t) \left(f \frac{L_{duct}}{D_2} + K_c + K_e + K_{aux} \right)}} \quad (4-23)$$

The mass flow rate $\dot{m}_2(t)$ of air is defined for CV₂ as the product of the density of the air $\rho(t)$ with the air-velocity through the orifice $V_2(t)$. The direction of the mass flow rate is defined by the sign of the pressure drop ($p_1 - p_a$), thus positive for mass flow into the CV₂ and negative for mass flow out of it. If the mass flow rate for CV₁ is required, the sign term has to be changed to ($p_a - p_1$).

When $\dot{m}_1 = -\dot{m}(t)$ then $\dot{m}_2 = \dot{m}(t)$

$$\dot{m}_2(t) = \rho(t) A_2 V_2(t) = \rho(t) A_2 \sqrt{\frac{|p_1 - p_a|}{\rho(t) \left(f \frac{L_{duct}}{D_2} + K_c + K_e + K_{aux} \right)}} \cdot \text{sign}(p_1 - p_a) \quad (4-24)$$

The pneumatic power $P(t)$ is calculated from the product of the volumetric flow rate $Q_2(t)$ with the pressure drop over the orifice.

$$P(t) = |p_1(t) - p_a| A_2 \sqrt{\frac{|p_1(t) - p_a|}{\rho(t) \left(f \frac{L_{duct}}{D_2} + K_c + K_e + K_{aux} \right)}} \cdot \text{sign}(p_1 - p_a) \quad (4-25)$$

Where the density of air is calculated as: $\rho(t) = \frac{p_1}{RT_1(t)}$ (4-26)

The following table (Table 4-3) describes the state equations defined for model 2.

Table 4-3: State equations for model 2

State equations for model 2	
Pressure	$\dot{p}_1(t) = \left[1 + \frac{C_p}{C_v} \right] \frac{\dot{m}(t)p_1(t)}{m_1(t)} - \left[1 + \frac{R}{C_v} \right] \frac{\dot{h}_1(t)p_1(t)}{h_1(t)}$
Mass flow rate	$\dot{m}(t) = \rho(t)A_2 \sqrt{\frac{ p_1(t) - p_a }{\rho(t) \left(f \frac{L_{duct}}{D_2} + K_c + K_e + K_{aux} \right)}} \cdot \text{sign}(p_a - p_1(t))$
Air chamber height	$h_1(t) = L_a - h_w(t)$
	$h_w(t) = A \sin \omega t$ $L_a =$ Initial height of air chamber $A =$ Amplitude of water column displacement
Air chamber speed	$\dot{h}_1(t) = -A\omega \sin \omega t$
States	$\dot{p}_1(t), h_1(t), \dot{h}_1(t), \dot{m}(t)$

4.3.4. OWC model with pneumatic power measurement device

The final model (model 3) describes the air-flow in the OWC model with the designed pneumatic power measurement device connected to the orifice defined in model 2. Model 3 simulates the pneumatic power using the pressure drop over the venturi flow meter and the volumetric flow rate through it. Figure 4-4 shows the diagram of the OWC model with the adjoined venturi flow meter. Control volume 1 (CV₁) is maintained from the other models as the air-chamber volume and control volume 2 (CV₂) covers the entire venturi device. The volumetric flow rate is calculated for two scenarios which make up the bidirectional air-flow. This would be using the pressure drop from the orifice to the venturi throat Δp_o for the upward air-flow and the pressure drop from the top of the venturi to the venturi throat Δp_i for the downward air-flow. The area of the throat of the venturi flow meter is given as A_t .

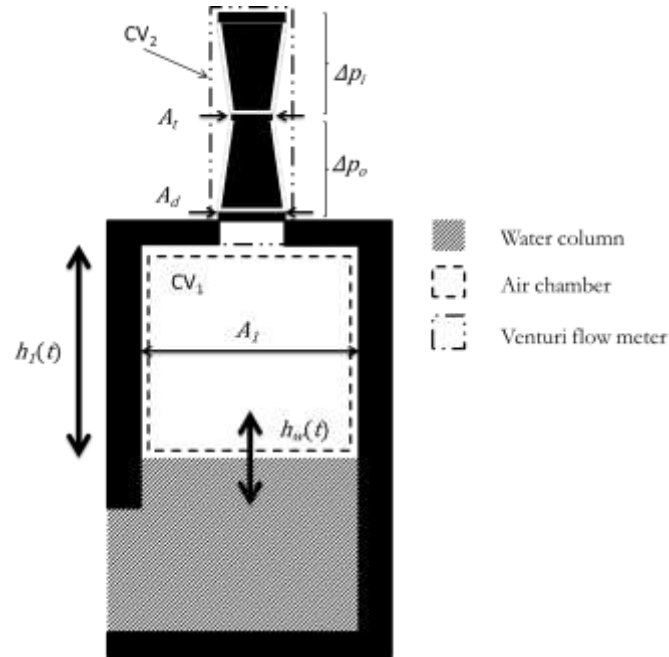


Figure 4-4: Diagram of the OWC model and the pneumatic power measurement device (venturi flow meter)

The assumptions for model 3 are the same as model 2. The state equation for the pressure differential is the same as model 2 (equation 4-16).

The mass flow rate through CV_2 is calculated from the volumetric flow rate equation of a venturi flow meter (equation 3-3). The velocity through the throat of the venturi flow meter V_t is calculated using equation 4-27.

$$V_t = \frac{A_d}{A_t} \sqrt{\frac{2\Delta p_{i,o}(t)}{\rho \left(\left(\frac{A_d}{A_t} \right)^2 - 1 \right)}} \quad (4-27)$$

Where: A_d is the area of the air-duct connected to the venturi
 A_t is the area at the throat of the venturi
 $\Delta p_{i,o}$ is the pressure differential between the air-ducts and venturi throat

The mass flow rate through CV_2 is calculated using the volumetric flow rate through the venturi flow meter.

$$\dot{m}_2(t) = \rho(t)A_t V_2(t) = \rho(t)A_d \sqrt{\frac{2\Delta p_{i,o}(t)}{\rho(t) \left(\left(\frac{A_d}{A_t} \right)^2 - 1 \right)}} \cdot \text{sign}(p_1 - p_a) \quad (4-28)$$

The pneumatic power through the venturi flow meter can be calculated using the pressure differential over the device and the volumetric flow rate.

$$P(t) = (p_1(t) - p_a)A_d \sqrt{\frac{2\Delta p_{i,o}(t)}{\rho(t)\left(\left(\frac{A_d}{A_t}\right)^2 - 1\right)}} \quad (4-29)$$

The following table (Table 4-4) describes the state equations defined for model 3.

Table 4-4: State equations for model 3

State equations for model 3	
Pressure	$\dot{p}_1(t) = \left[1 + \frac{C_p}{C_v}\right] \frac{\dot{m}(t)P_1(t)}{m_1(t)} - \left[1 + \frac{R}{C_v}\right] \frac{\dot{h}_1(t)P_1(t)}{h_1(t)}$
Mass flow rate	$\dot{m}(t) = \rho(t)A_d \sqrt{\frac{2\Delta p_{i,o}(t)}{\rho(t)\left(\left(\frac{A_d}{A_t}\right)^2 - 1\right)}} \cdot \text{sign}(p_a - p_1(t))$
Air chamber height	$h_1(t) = L_a - h_w(t)$
	$h_w(t) = A \sin \omega t$ $L_a =$ Initial height of air chamber $A =$ Amplitude of water column displacement
Air chamber speed	$\dot{h}_1(t) = -A\omega \sin \omega t$
States	$p_1(t), h_1(t), \dot{h}_1(t), \dot{m}(t)$

4.3.5. Selection of loss coefficients

The selection of the contraction and expansion coefficient K is determined from the prescribed curve from Çengel and Cimbala (2010) shown in Figure 4-5. Using the ratio of the orifice diameter (d) and the air-chamber diameter (D), the resultant contraction coefficient K_c and expansion coefficient K_e can be obtained.

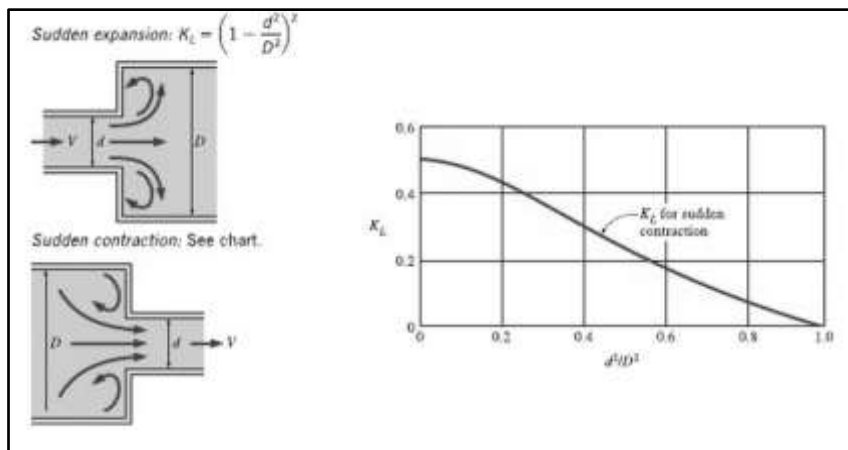


Figure 4-5: Selection of contraction and expansion coefficients (Çengel and Cimbala, 2010)

The selection of the auxiliary loss coefficient K_{aux} is selected by a trial-and-error method during the simulation tests and is discussed in detail in chapter 6.

4.4. Conclusions

Three analytical air-flow models have been documented in this chapter which describe the air-chamber pressure, volumetric flow rate of air and pneumatic power under various OWC model conditions. The air-flow models utilise derivations from applicable laws of fluid mechanics to predict the operation of the air chamber. The simulated air-flow models provide a platform for comparative analysis with the experimental results from the OWC model wave flume tests.

For the three models, the water column displacement $h_w(t)$ is assumed to be sinusoidal according to wave heights used in the experimental testing. However in the results chapter (chapter 6), the recorded water column displacement from the experimental tests will be additionally used as the forcing function input to the models.

The values of the loss coefficients K_c , K_e and K_{aux} described in model 2 are given in chapter 6. The auxiliary loss coefficient K_{aux} is investigated in detail in the chapter on results where the exact value varies according to the test conditions.

Detailed derivations and Simulink block-diagrams for the air-flow models are shown in Appendix A.

5 Testing: calibration and experiments

This chapter explains the details of the calibration testing of the pneumatic power measurement device in the vertical wind tunnel and the wave flume experiments to test the designed measuring device on an OWC model. The chapter begins with the description of all the equipment used for the pneumatic power measurement device and in the wave flume, then the details of wind tunnel calibration of the device and lastly the details of the wave flume and OWC model experimental setup.

5.1. Measuring equipment

The measurement equipment that was selected for the pneumatic power measurement tool comprised of the pressure transducers used for pressure drop and volumetric flow rate measurements in an OWC model and the hot-film anemometer for the low volumetric flow rate measurements. In addition to the transducers, a DAQ unit was required to handle the recording of the measurements and transfer them to the laptop for analysis. Figure 5-1 describes the schematic layout of the measurement system from the transducers in the wave flume to the recorded data on the laptop.

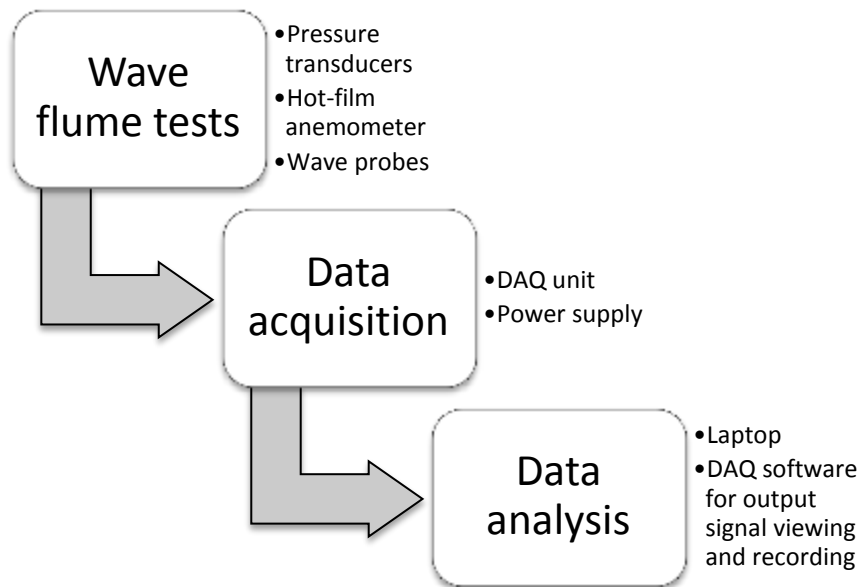


Figure 5-1: Layout of the complete measurement system

For the venturi flow meter, the three pressure transducers that were selected were gauge-type pressure transducers with a measurement range of -5 kPa to 5 kPa. These selected low pressure transducers have an accuracy of 2.5 % of the full-scale output (FSO). As mentioned before, the pressure transducers were used for the volumetric flow rate measurement and the pressure drop measurement over the throat of the venturi flow meter.

The pressure transducers utilised for the monitoring of the oscillating pressures in the air chamber of the OWC model were differential pressure transducers. A differential pressure transducer was used due to its ability to measure more accurately than the gauge pressure transducers selected for the venturi flow meter. These differential pressure transducers have an operating range of -2.5 kPa to 2.5 kPa.

The selected hot-film anemometer is the SCHMIDT® SS 20.400 flow sensor. This hot-wire anemometer has the capability of measuring bidirectional flow rates and measuring air velocities down to 0.05 m/s. This made it a suitable selection for the application at the throat of the venturi flow meter. Another critical specification of this anemometer is its relatively fast frequency response of 0.01s which allows it to sample the oscillations of the air velocities at a suitable rate.

The DAQ unit handles the analog data received from the pneumatic power measurement device on the OWC model and transmits it to the laptop where it can be viewed and analysed. The Eagle USB MicroDAQ unit with 16 analog inputs was selected for the measurement system. This unit was specifically chosen for its sampling rate of 250 kHz which allowed simultaneous sampling of the output signals from all the pressure transducers and the hot-film anemometer. Having the entire equipment inventory of the pneumatic power measurement device on the same MicroDAQ unit had the benefit of having all the measurements on the same time series.

The measurement of the wave heights in the wave flume and the water column oscillations in the OWC was performed by the HR Wallingford EQ009 wave probes. These wave probes are made up of two stainless steel rods joined by a plastic head and foot connection. They operate by measuring the current through the two stainless steel rods when immersed in water. The output voltage, measured from the current, is directly proportional to the immersion depth.

Table D-1 shows further specifications and relevant details on the complete measurement system that was used for the calibration tests and during the wave flume tests.

5.2. Calibration of the pneumatic power measurement tool

The calibration of the pneumatic power measurement device was performed in a vertical wind tunnel at the Mechanical and Mechatronics Department's heat transfer lab. The calibration tests involved the comparison of the actual volumetric flow rate Q_a of the wind tunnel to the measured volumetric flow rate Q_m of the venturi flow meter and hot-film anemometer at steady state.

5.2.1. The vertical wind tunnel

The vertical wind tunnel was constructed as part of a research study, performed by a doctorate student. It operates in such a manner that the system's fan creates

a pressure drop over its structure resulting in air-flow being drawn into it from the atmosphere. A pre-calibrated elliptical nozzle with pressure differential measurement is used to measure the actual volumetric flow rate through the tunnel. The pressure drop is measured upstream and downstream of the elliptical nozzle by a plenum chamber. Three differential pressure transducers, pre-calibrated using a Betz micromanometer, are utilised to measure the mass flow rate in the tunnel. Two of these pressure transducers have an operating range of 0-2.5 kPa range and one of them has an operating range of 0-25 kPa.

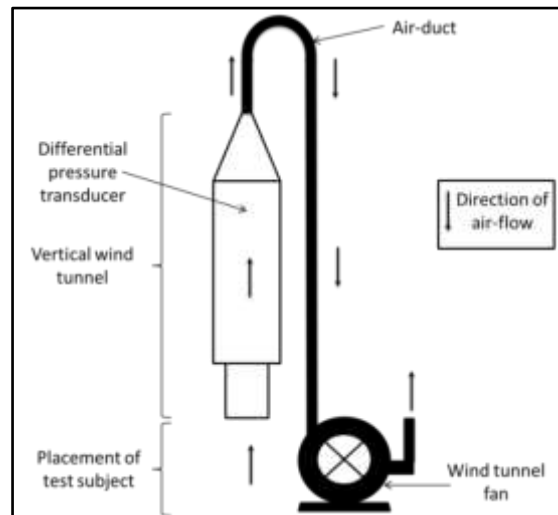


Figure 5-2: Schematic diagram of the vertical wind tunnel

The accuracy of the wind tunnel is based on the estimated mass flow error which ranges from 1 – 4 % depending on the flow rate (Allen, 2012). A 4 % error would be apparent at the lowest mass flow rate in the wind tunnel and decreases as the flow rate increases. The actual volumetric flow rate through the wind tunnel was calculated from the measured mass flow rate using the measured air density, determined during each test. Figure 5-2 describes the setup of the vertical wind tunnel.

5.2.2. Calibration setup and testing

The venturi flow meter was placed vertically in the tunnel with the OWC model's roof attached so that the calibration tests resembled the experimental setup during the wave flume tests. The connection to the wind tunnel was achieved using a wooden plank, with an orifice cut-out, fixed onto the air-duct of the venturi flow meter. The plank was sealed onto a foam pad of the vertical wind tunnel by clamping it to a pair of hinges. This was done to ensure that the venturi flow meter was air-tight which maintained the air-flow path in achieving accurate results. Figure 5-3 illustrates the calibration test setup with the venturi flow meter connection to the entrance of the vertical wind tunnel.

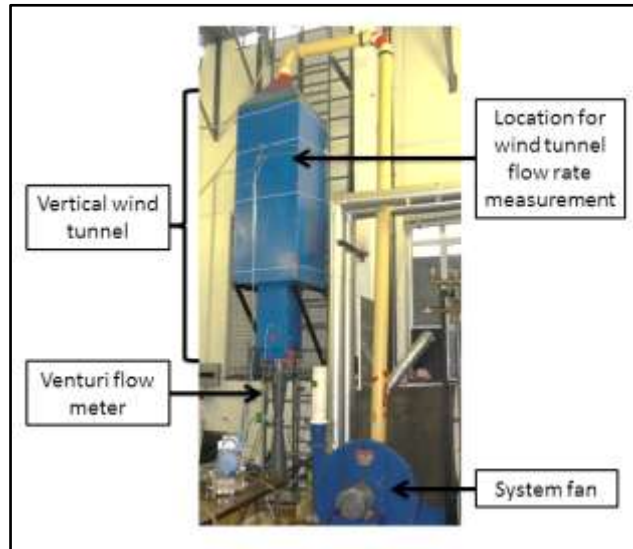


Figure 5-3: Setup of the calibration tests at the vertical wind tunnel

The purpose of the calibration tests was to verify that the measured volumetric flow rate of the venturi flow meter combined with the hot-film flow meter was accurate. Any differences in the measured and actual values would be compensated by a suitable correction factor. Two sets of tests were carried out during the calibration in the vertical wind tunnel. The first test measured the velocity from the hot-film anemometer in the throat of the venturi meter only. The second test measured the volumetric flow rate by the venturi flow meter from its pressure transducers, while the hot-film anemometer was inserted at the throat. Two separate tests were carried out so that smaller increments of the lower volumetric flow rates could be analysed for the calibration of the hot-film anemometer.

The calibration tests were performed by incrementing the volumetric flow rate through the wind tunnel, then recording the measured and actual volumetric flow rate at each increment. Each measurement was logged, for at least 30 seconds, once steady state had been reached. The range of flow rates that were tested during calibration were chosen to be higher than the range of operating flow rates forecasted for the wave flume experiments. The coefficient of discharge C_d is the correction factor applied to the measured volumetric flow. Equation 5-1 describes the coefficient of discharge C_d as a ratio of the actual volumetric flow rate Q_a to the measured volumetric flow rate Q_m . A C_d value of 1 shown in figures 5-4, 5-5 and 5-6 indicates the raw measured data from the venturi flow meter and hot-film anemometer.

$$C_d = \frac{Q_a}{Q_m} \quad (5-1)$$

In addition to the calibration tests for the volumetric flow rate, a 'block' test was performed on the venturi flow meter to assess if there were any air-leaks in the system. This was done by firmly blocking the entrance of the venturi flow meter's

air-duct (end connected to the OWC roof) with polystyrene. Subsequently, the fan of the wind tunnel was activated at a certain speed to develop a pressure drop over the system. The pressure transducers of the wind tunnel were then checked for any pressure drop over its elliptic-nozzle flow meter, which would indicate the presence of air-leaks in the venturi flow meter. The blocked tests confirmed that the combination of the venturi flow meter and the hot-film anemometer had no air-leaks.

5.2.3. Results of the calibration tests

The measured volumetric flow rate from the hot-film anemometer was calculated by multiplying the velocity readings by the area of the venturi flow meter's throat. The first calibration test results for the hot-film anemometer at the throat of the venturi are shown in Figure 5-4. The four curves describe the actual volumetric flow rate readings of the wind tunnel, Q_a , and the volumetric flow rate from the hot-film anemometer Q_m with three coefficients of discharge ($C_d = 1, 1.05$ and 1.09). The correction factors are applied so that the calibrated curve covers the range of wind tunnel volumetric flow rates from a zero reading until the hot-film anemometer reaches its maximum velocity reading of 20 m/s. This takes place at a volumetric flow rate (Q) of approximately $0.05 \text{ m}^3/\text{s}$.

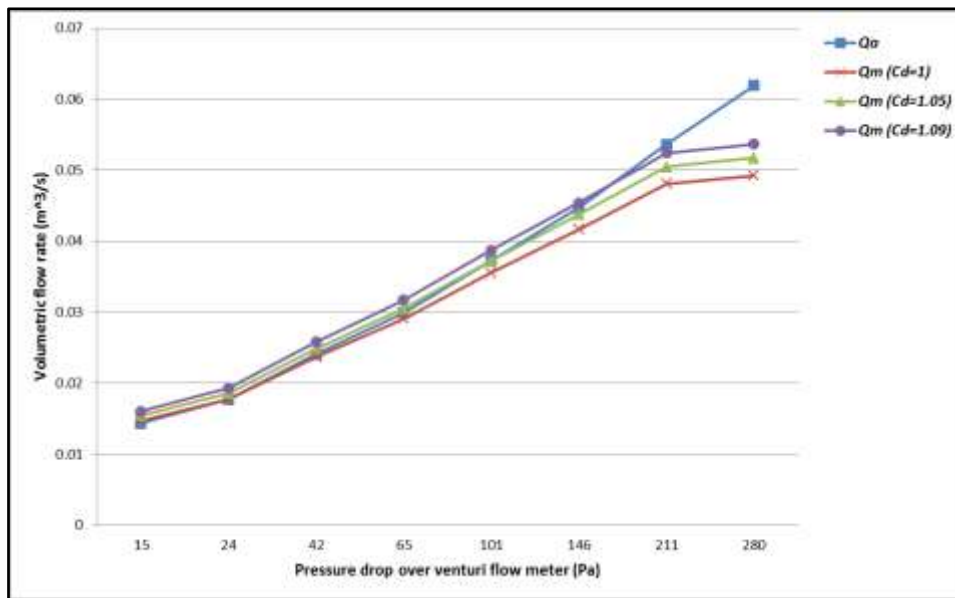


Figure 5-4: Calibration curve for the hot-film anemometer

The second calibration test results for the venturi flow meter are shown in Figure 5-5. The actual volumetric flow rate Q_a was compared against four coefficient of discharge values ($C_d = 1, 0.89, 0.93$ and 0.98) for the range of volumetric flow rates tested. From Figure 5-5, it is clear to see that the volumetric flow rates measured by the venturi flow meter are considerably inaccurate at low flow rates. However the corrected curves start to follow the actual volumetric flow rate curve at around 141 Pa.

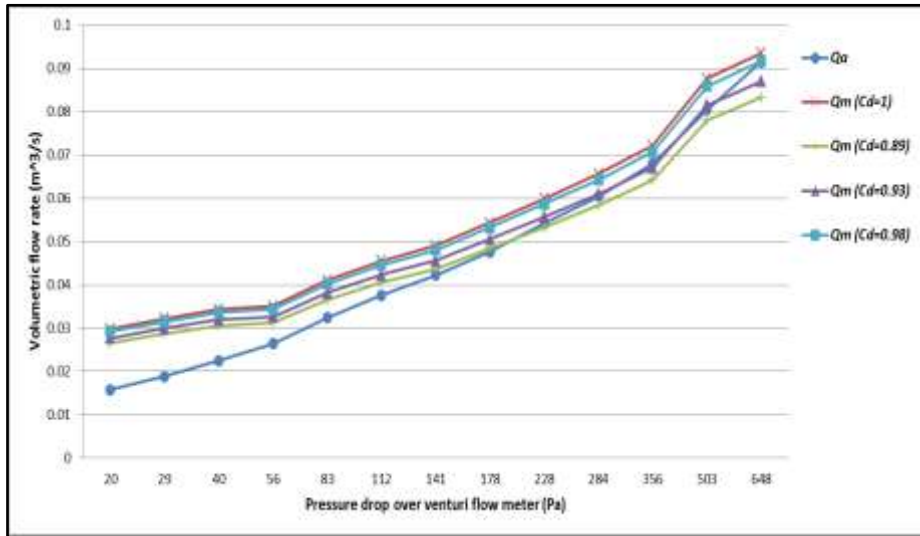


Figure 5-5: Calibration curve for the venturi flow meter

From the two sets of calibration tests performed, a summary table (Table 5-1) was developed which describes the volumetric flow rate ranges with its corresponding coefficient of discharge. The flow rate ranges are designated for either the hot-film anemometer or the venturi flow meter that was used to calculate the corrected volumetric flow rate. The correction factors for each flow rate range were determined under a condition that the calibrated curve didn't vary more than 3 % from the actual volumetric flow rate curve. From Table 5-1, it can be seen that the lower volumetric flow rates up until $0.048 \text{ m}^3/\text{s}$ would be measured by the hot-film anemometer and from there on the venturi flow meter would be used. The coefficient of discharge values for the venturi flow meter increase as the measured volumetric flow rate increases and reaches a value close to unity ($C_d = 0.98$) at the upper end of the flow rate scale. The summary of the calibration tests confirms the design for the incorporation of the hot-film anemometer with the venturi flow meter to cater for the inaccuracies at lower flow rates.

Table 5-1: Summary of the calibration results for the hot-film anemometer and the venturi flow meter

Range of volumetric flow rate Q (m^3/s)	Coefficient of discharge (C_d)	Flow meter used
0-0-029	1.0	Hot-film anemometer
0.029- 0.042	1.05	Hot-film anemometer
0.043-0.048	1.09	Hot-film anemometer
0.049-0.063	0.89	Venturi flow meter
0.064-0.088	0.93	Venturi flow meter
Greater than 0.089	0.98	Venturi flow meter

The average coefficient of discharge for the hot-film anemometer is 1.05 and for the venturi flow meter, 0.93. ASME (1985) and ASME (1971) recommend a coefficient of discharge of 0.995 for a typical machined venturi flow meter. The compromise on the C_d value for the designed venturi flow meter is satisfactory considering the variations in the venturi flow meter design for the bidirectional air-flow system. The calculated average coefficient of discharge value for the complete pneumatic power measurement device is 1.18.

Figure 5-6 shows the calibrated volumetric flow rate curve with the actual volumetric flow rate curve for the full range of fan frequencies used for both the venturi flow meter and the hot-film anemometer calibration tests.

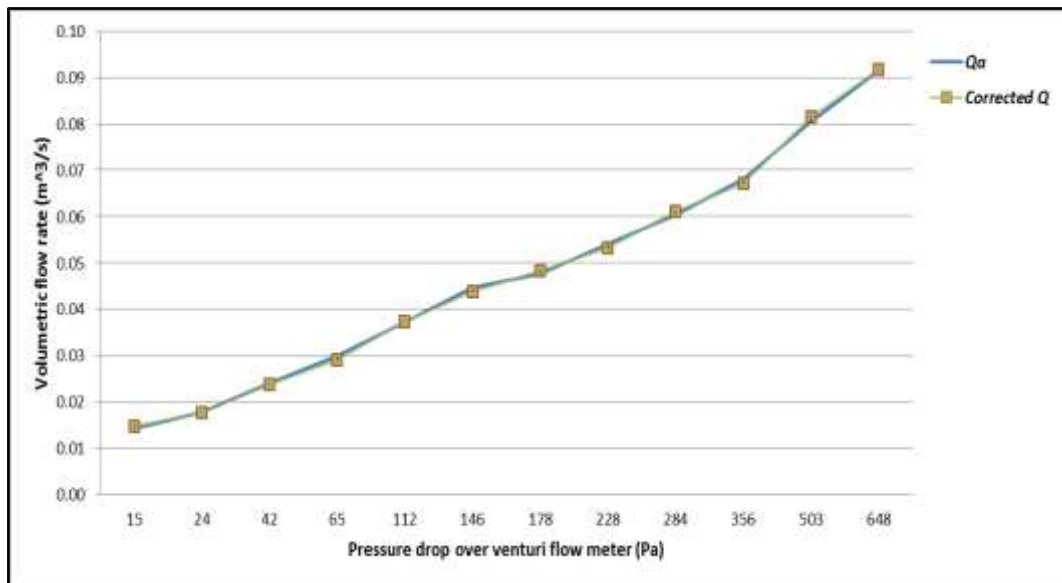


Figure 5-6: Calibration curve of the pneumatic power measurement device

To analyse the goodness-of-fit of the calibrated volumetric flow rate curve with the actual wind tunnel curve, the residuals ($Q_m - Q_a$) between the volumetric flow rate measurements were calculated. The percentages of the residuals are shown in Table 5-2 against the range of pressure drop over the venturi flow meter. The greatest percentage error of 2.8 % between the calibrated curve and the wind tunnel curve at 65 Pa falls within the established 3 % error margin specified for the calibration test. This calibration accuracy compares well with the $\pm 2\%$ accuracy of Jayashankar et al's (2007) air velocity probe. Any significant residuals found at lower frequencies are noticeable as a percentage value due to their low relative volumetric flow rate values.

Table 5-2: Percentage residuals of the calibration tests

Pressure drop over venturi flow meter (Pa)	Percentage residual (%)
15	2.6
24	0.2
42	1.5
65	2.8
112	0.2
146	2.0
178	1.6
228	1.6
284	0.9
356	1.3
503	1.4
648	0.2

The ambient conditions recorded during each calibration tests are shown in Table 5-3. These conditions signify the average of the ambient temperatures, pressures and air densities that were recorded.

Table 5-3: Ambient conditions during calibration tests

Average ambient temperature (°C)	18.2
Average ambient pressure (Pa)	100,650
Average air density (kg/m ³)	1.204

5.3. Wave flume experiments

The wave flume at the Department of Civil Engineering at Stellenbosch University was the location where the experimental tests of the OWC model with the pneumatic power measurement device were performed. The purpose of the wave flume experiments was to test the operation of the designed pneumatic power measurement device with an OWC model operating under various wave conditions. This section describes the wave flume system, the set-up of the equipment and the testing procedure of the pneumatic power measurement device.

5.3.1. Overview of the wave flume

The location for the experimental testing of the pneumatic power measurement tool is the glass wave flume which uses the HR Wallingford EQ1021 wave maker. The wave flume has a length of approximately 30 m, width of 1 m and a depth of 1.2 m which uses a piston paddle, driven by a small electric AC servomotor to generate waves. At the downstream side of the wave flume, the artificial 'beach' absorbs unwanted reflections returning towards the wave maker.

The signal-generation computer with the HR Wavemaker software controls the paddles to generate the wave types that are defined by the user. The specifications of the EQ1021 wave maker allow it to generate waves at a maximum water depth of 0.8 m with a maximum wave height of approximately 0.3 m. The wavemaker has the ability to generate numerous wave heights at different frequencies as long as it obeys the theoretical performance curves for the applied water depth. The

wave flume system also has the capability of dynamic wave absorption, which prevents reflected waves from the OWC model being reflected back by the wave maker's paddle (HR Wallingford, 2010).

The wave probes of the wave flume are measured by a custom HR Wallingford DAQ unit, known as the HR DAQ. The input signals to the HR DAQ unit can be viewed as water level displacements on the HR DAQ software.

5.3.2. Experimental setup

The OWC model used to test the pneumatic power measurement device was constructed out of perspex sheets and glued together using Tensol™ no. 17 adhesive. Before the OWC model was placed in the wave flume, clear silicone was placed on all the joints of each section of perspex to prevent any leaks in the water column chamber and the air chamber. The dimensions of the perspex box are shown in Figure 5-7 along with an image of the experimental setup in the wave flume. The OWC model was designed so that it covered the whole width of the wave flume. The thickness of the box was maintained at 10 mm for all the sides except for the front wall which is 20 mm thick. This was done to strengthen the front wall from the force of the incoming waves. Two threaded rods (stiffeners) were placed between the front wall and the back wall to stabilise the box and to minimise the contraction and expansion of the model during operation in the wave flume. The diameter of the orifice on the roof of the OWC model is the same as the air-duct's inner diameter D_d of the venturi flow meter.

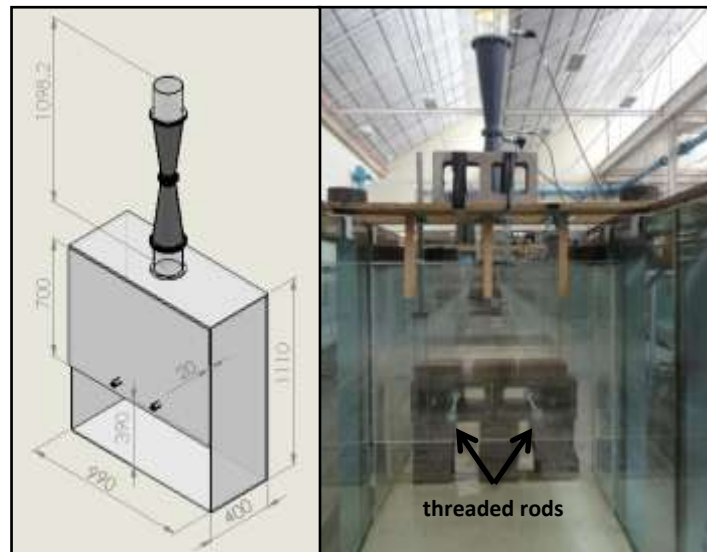


Figure 5-7: Dimensions of the OWC model (mm) and image of the experimental setup

Figure 5-8 shows the experimental setup of the OWC model with the pneumatic power measurement device attached in the wave flume. The OWC model should be placed at least two wavelengths away from the wave maker so that fully developed waves are incident to the OWC box (Rea, 2008). As a result, the model was positioned 11 m from the wave maker which allowed for fully developed

waves to be formed for the range of selected wave frequencies. Three wave probes are used during the wave flume testing; two of them were placed before the OWC model to analyse the incoming wave conditions and one of them was placed in the box to measure the water column displacement inside the OWC chamber.

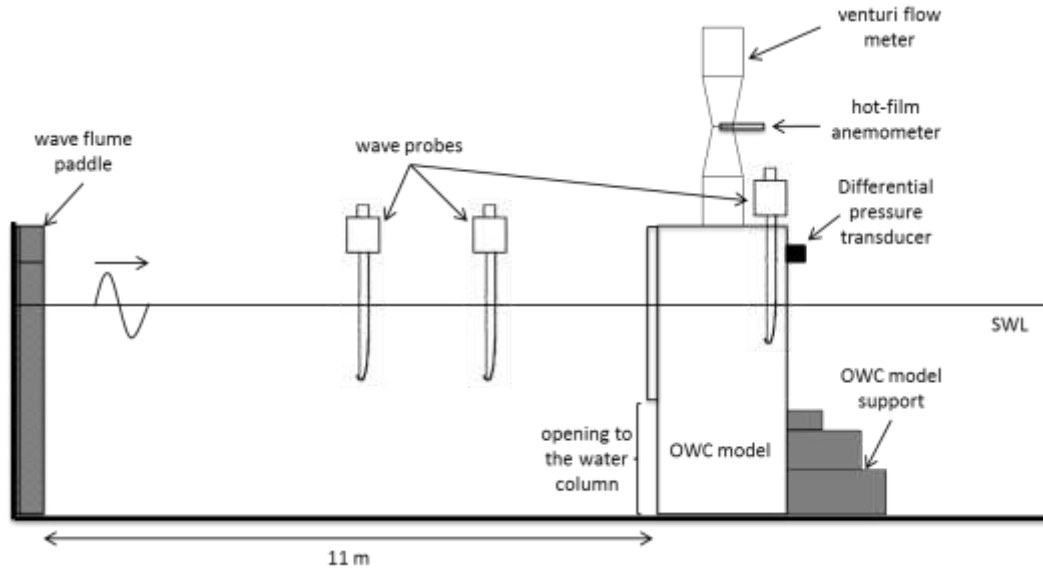


Figure 5-8: Experimental setup in the wave flume

An arrangement of bricks was placed behind the OWC model for structural support so that any backward movement during testing would be prevented. Figure 5-9 shows images of the front support and the back support of the OWC model, which prevented horizontal movement of the box.



Figure 5-9: Supports for the OWC model in the wave flume

The careful wiring of the measuring equipment from the wave flume setup to the respective DAQ units was an important step in ensuring that the output signals

were matched to their respective transducers. The grounding of all signals at a common ground (power supply ground) stabilised the analog output signals. Appendix C shows a wiring diagram of the transducers to the MicroDAQ and the HR DAQ.

5.3.3. Test schedule

The testing schedule for the pneumatic power measurement device was performed for various wave conditions, which comprised of 34 tests in total. The wave height and wave frequency was varied for three different water depths D . Two crest-to-trough wave heights H_w were tested (for most tests) and the wave frequencies f ranged from 1 Hz to 0.33 Hz, depending if they obeyed the theoretical performance curve of the wavemaker. The dependent variables for the wave flume experiments were the wave height H_w , the wave frequency f and the water depth D . The independent variables were the air chamber pressure p_a , the pressure at the three measurement locations of the venturi flow meter $p_{1,2,3}$, the venturi flow meter throat velocity V and the oscillating water column displacement h_w . Table 5-4 summarise the range of dependent variables, used for the three water depths, which were used as the wave flume testing parameters for the experimental tests.

Table 5-4: Experimental test parameters

Water Depth D (m)	Wave Heights H_w (m)	Wave Frequencies f (Hz)
0.5	0.05	0.67 0.57 0.50 0.44 0.40 0.30
0.6	0.05 0.1 0.125 0.15	1.00 0.67 0.57 0.5 0.44 0.40 0.30
0.7	0.05 0.1	1.00 0.67 0.57 0.50 0.44 0.40 0.30

The testing of the pneumatic power measurement device involved the recording of measurements for 30 seconds once steady oscillations were observed in the OWC model. These exclude separate tests of a closed-box OWC model and an OWC model with an orifice, which did not include the designed pneumatic power measurement device. The ambient temperature and air density was also monitored to assess if there were any drastic changes between successive test days.

The software that was used to record the measured data during the experiments is WaveView for Windows which was supplied with the MicroDAQ unit. WaveView allowed the real-time viewing of the output signals from the transducers and saved the data directly to file. The equations for calculating the measured value from the analog output signals are shown below. Equation 5-2 gives the pressure value from the gauge pressure transducers on the venturi flow meter and equation 5-3 gives the air-velocity value from the hot-film anemometer. The hot-film anemometer output is specified at 0-10 V but was assessed during the calibration tests to be 5-10 V due to additional resistance in the MicroDAQ unit.

$$\text{Pressure (Pa): } y_1 = 6250 x_1 - 7500 \quad (5-2)$$

$$\text{Velocity (m/s): } y_2 = 4 x_2 - 20 \quad (5-3)$$

Where: x_1 is the output signal in millivolts (mV)
 x_2 is the output signal in volts (V)

The calibration of the wave probes was performed once at the beginning of every day of testing and at the beginning of every test where there was a change in the water depth. This was carried out using the HR Wallingford HR DAQ software, where a calibration curve was prepared for a specific test. The calibration procedure involved the recording of at least three points on the immersed wave probe to prepare a goodness-of-fit using the Least Squares Method. These points included the datum point (zero wave height), above the datum and below the datum point. The calibration curve for this differential pressure transducer was obtained using a Betz micromanometer.

Due to the OWC model covering the whole width of the wave flume, there was a substantial amount of reflected waves off the front wall of the OWC model. The dynamic wave absorption of the wavemaker was adjusted for each variation in the wave frequency at each tested water depth so that reflected waves could be minimised by the wavemaker. This was achieved using the absorption gain input of the wavemaker. The comprehensive testing schedule is detailed in Appendix E.

5.4. Conclusions

This chapter has described the various measuring equipment which were involved with the pneumatic power measurement device; from the transducers in the wave flume to the signal-viewing software on the laptop. The setup, procedure and results of the crucial calibration tests were explained and it was established that the calibrated curve for the volumetric flow rate measurement had an error of less than 3 % relative to the actual wind tunnel volumetric flow rate curve. A key objective of the calibration tests was to prove that there were no air-leaks in the pneumatic power measurement device. The blocked tests confirmed that the pneumatic power measurement device had no air-leaks present.

The experimental setup in the wave flume described the dimensions of the OWC model designed to cover the full width of the flume. The force of the incident waves resulted in the requirement of front and back support of the model during wave flume testing. The complete wave flume testing of the pneumatic power measurement device involved a total of 34 tests.

6. Results and discussion

To accomplish the objectives of this research study, a number of experimental tests were performed in the wave flume utilising the OWC model with the pneumatic power measuring device. The fundamental areas of interest from these experiments are the water column oscillations, the air chamber pressure, the pressure drop over the venturi flow meter and the volumetric air-flow rate through the venturi flow meter.

This chapter of the thesis discloses the results from the wave flume experimental tests, focusing on comparisons of the experimental results with the simulation models described in chapter 4. The comparison of the experimental results with the simulation of the analytical air flow models in the Matlab Simulink program creates a platform to highlight any fundamental differences between the two results. This is an opportunity to account for the differences and propose recommendations for future research. In addition to the comparative analysis, the results from the various tests are independently analysed with regards to the test parameters, such as water column resonance and average pneumatic power analysis.

6.1. Overview of experimental tests

6.1.1. Test procedure

The wave flume testing was performed according to the testing schedule described in Appendix E for the experimental setup shown in chapter 5. The testing schedule was developed in a way to measure the pneumatic power over a suitable range of varying wave parameters.

Tests which included the two larger wave heights of 0.125 m and 0.15 m shown in Table 5-4 for a water depth $D=0.6$ m and for wave frequencies of $f=0.5$ Hz and $f=0.44$ Hz were performed at the end of the wave flume experiments. This was done to test the upper limits of the pneumatic power that could be measured with the OWC model. The water depth of $D=0.5$ m only allowed for the small wave height $H_w=0.05$ m due to the prevention of inlet broaching. At this water depth, air-chamber pressures were low due to the small water column activity; therefore it is not used in the comparative analysis with the simulation models.

Before and during each test, there were certain checks which were carried out to ensure optimum test conditions were maintained. These include tests such as checking whether the:

- Water depth decreased in case there were any severe leaks in the wave tank,
- Measurement equipment were securely connected to the OWC model,
- Equipment output signals were correctly being displayed on the laptop,
- Roof was securely on the OWC box so that no air leaks are present,
- Generated wave periods in the wave tank were the same as the input,

From the basic test inspections, it was concluded that no fatal flaws were present during the wave tank experiments. The wave heights in the wave tank could not be checked for consistency with the input wave heights directly from inspecting the wave tank due to the presence of reflection.

6.1.2. Damping

The damping involved with the PTO of the air system played a substantial role in the conversion efficiency of the OWC device. The damping of the air chamber is dependent on the size of the smallest orifice in the pathway of the air oscillations, which was distinctly defined by the throat diameter of the venturi flow meter. The throat diameter was determined according to the air duct diameter so that the venturi ISO standards were satisfied. Accordingly, the air duct diameter was based upon a satisfactory area ratio between the air duct and the air chamber. The functionality of the OWC model is primarily based on the optimum oscillations of the water column therefore larger orifices were not accommodated due to insufficient generation of pressure in the air chamber. With reference to the induced damping from the specified orifice diameters, Sarmiento (1992) suggests that in some cases the air compressibility effect can be ignored for small models.

6.1.3. Closed roof tests

During the wave flume experiments, additional observation tests were performed without the pneumatic power measurement device. Prior to the measurement of the pneumatic power from the OWC model with an orifice, a basic test was performed to view the effect of a closed roof model on the behaviour of the water column. These tests were performed at a water depth of $D=0.7$ m and for a random set of wave heights and wave periods. Results showed that the excessive damping caused by the closed roof gave rise to high air chamber pressures but limited the water column activity in the OWC model, which is the driver of air-flow activity.

6.1.4. Basic post processed results

The required results for pneumatic power measurement include the pressure drop over the venturi flow meter and the volumetric flow rate through the venturi. The post processing of the volumetric flow rate results involved the necessary adjustments from the calibration test results, summarised in Table 5-1. Additional measurements which were also recorded were the water column displacement, the wave height, wave frequency and the pneumatic pressure of the air chamber. An example of the post processed pneumatic power results from the experimental tests in the wave flume is shown in Appendix E.

6.2. Equipment accuracy & resolution

Ahead of the comparative analysis of the experimental results with the simulation model results, the accuracy evaluation of the measuring equipment is investigated.

This allows a means to justify the results relative to the equipment used during the wave flume testing.

The degree of accuracy of the experimental testing results is fundamentally based on the resolution of the measuring equipment of the pneumatic power measurement device. In other words, the difference between the measured values of the pressure and velocity flow rate equipment and their actual values, defined by their theoretical operation, is based on their respective resolution. Figliola & Beasley (2006) define the resolution of the measuring equipment as the smallest increment in the measured value that can be correctly determined. The resolution of the utilised measuring equipment is calculated using equation 6-1, developed from the definition stated by Figliola & Beasley (2006) above, which utilises the full-scale output (FSO) and the rated accuracy percentage of the equipment.

$$\text{Resolution} = \text{FSO} \times \text{Rated accuracy \%} \quad (6-1)$$

Table 6-1 details the resultant measuring resolution from the measuring equipment whose values are used in the pneumatic power calculations.

Table 6-1: Resolution of measurement equipment

Measuring Equipment	Rated Accuracy Percentage (%)	Full Scale Measurement Range	Measurement Resolution
Gauge pressure transducer	2.5	-2.5 kPa to 2.5 kPa	125 Pa
Hot-film anemometer	3.0	0-20 m/s	0.6 m/s
Differential pressure transducer	1.0	0 kPa to 2.5 kPa	25 Pa

The total rated accuracy percentage for the key equipment of the full pneumatic power measuring device is summed to be 6.5 %, based solely on the resolution of the equipment. The degree of resolution for the measuring equipment, in particular the hot-film anemometer and the differential pressure transducer, can be considered suitable for attaining accurate measurements. The gauge pressure transducer has a large resolution relative to the differential pressure transducer which provides room for inaccuracy measurements but there is substantial reasoning for selecting this equipment. The gauge pressure transducer was selected due to it catering for the peak pressure values, which made it especially difficult to size the equipment with an extremely fine resolution due to the wide-ranging wave heights being tested. Additionally, the venturi flow meter uses gauge pressure measurements which had high values during peak volumetric flow rate of the air-flow oscillations. Even though differential pressure transducers have lower ranges of measuring equipment and finer resolution levels, it would limit the testing range and not cater for especially high oscillation peaks.

Bringing together the conclusions from the calibration tests (chapter 5), the error percentage established from the calibration tests was determined to be less than 3%. This is considered to be satisfactory and in-line with the undertaking to develop an accurate pneumatic power measurement device. As previously noted,

the calibration tests were performed in steady state conditions as opposed to the air-flow due to the wave tank tests which is turbulent and bidirectional. This is a key factor which drives the comparison of the experimental results with the simulation results, in an effort to highlight any critical discrepancies.

6.3. Comparative analysis of the pneumatic power measurement device

The comparative analysis procedure makes use of selected experimental results along with the simulation models detailed in chapter 4. From a preliminary screening, selected wave frequencies for two wave heights (H_w) and two water depths (D) were chosen for this analysis. Table 6-2 details the test parameters that were selected for the comparative analysis of the pneumatic power measurement device. These parameters were selected so that the low and high frequency spectrum of the wave testing parameters are analysed over a low to high wave height and water depth.

Table 6-2: Test parameters for the comparative analysis

Test Parameters for Validation Process		
Frequency f (Hz)	Wave Height H_w (m)	Water Depth D (m)
0.44	0.05	0.6
0.67	0.1	0.7

The water depth was not exclusively accounted for in the simulation models, due to added mass, from the water depth, not being part of the simulation model scope. The water depth did however play an indirect role in the simulation model through the change in initial air column height L_a (at SWL) when the water depth is varied. When the water depth $D=0.7$ m the air column height is 0.4 m and when the water depth $D=0.6$ m the air column height is 0.5 m.

The comparison of the experimental results with the simulation models is performed for models 2 and 3 described in chapter 4. Three scenarios have been analysed for comparative analysis. These include two scenarios for model 2 and 1 scenario for model 3. The same tests are compared in each scenario so that consistency is maintained through the process.

For the comparison of the selected experimental results with model 2, the scenarios comprise of a sinusoidal OWC displacement and then the OWC displacement recorded during the experimental results. The final scenario from model 3, which is the pneumatic power measurement device on the OWC model, is used to analyse the complete measurement device through the comparison of the pneumatic powers.

The auxiliary loss coefficient K_{aux} , used in model 2, is selected by a trial-and-error method during each simulation comparison. This allows the simulated results to

be adjusted according to the experimental results, in an effort to account for amplitude variations between the two curves.

6.3.1. Scenario 1 – Model 2 (Sinusoidal water column input)

This section compares the experimental results from the pneumatic power measurement tests with simulation of air-flow model 2, which is the OWC model with the orifice on the roof. The sinusoidal input into the model matches the amplitude of the wave height and the wave frequency tested in the wave tank. The sinusoidal water column displacement provides an ideal input into the OWC system along with the air-flow through the orifice representing the air-flow through the venturi flow meter. The orifice diameter in model 2 is kept the same as the throat diameter of the venturi flow meter so that similar damping levels are maintained.

The first comparison is for the lower test frequency $f=0.44$ Hz, which was visually seen to deliver the optimum motion of the water column. Figure 6-1, Figure 6-2 and Figure 6-3 show the comparison of the pressure, volumetric flow rate and pneumatic power respectively with model 2, for wave height $H_w=0.1$ m and frequency $f=0.44$ Hz for the two water depths.

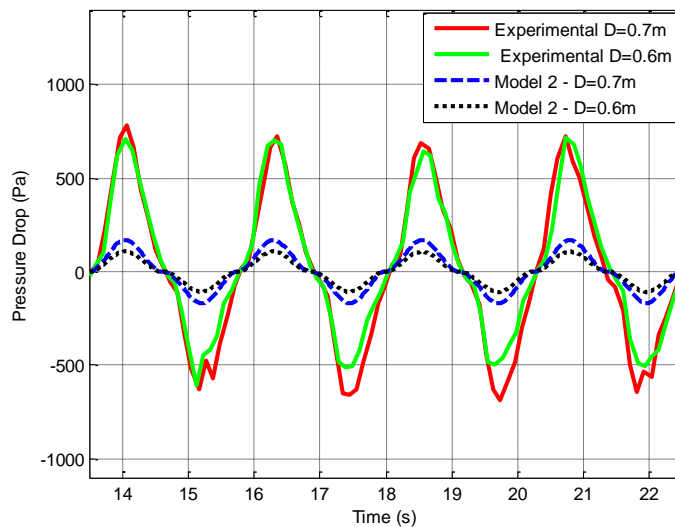


Figure 6-1: Pressure drop over venturi throat for test $f=0.44$ Hz and $H_w=0.1$ m (scenario 1)

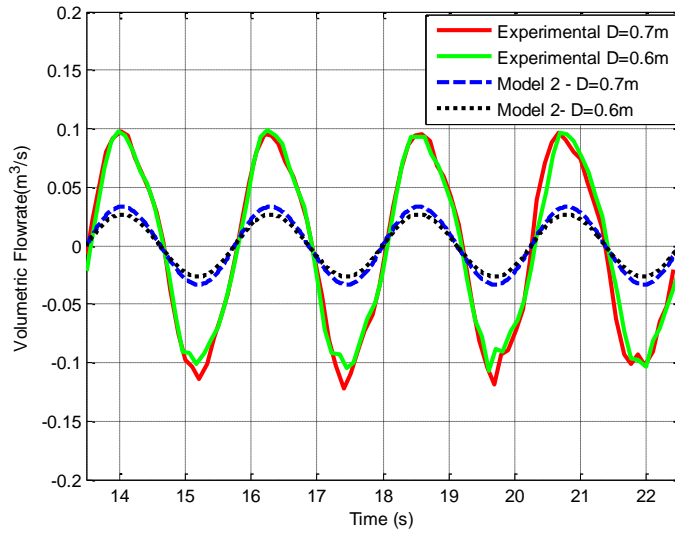


Figure 6-2: Volumetric flow rate for test $f=0.44\text{Hz}$ and $H_w=0.1\text{m}$ (scenario 1)

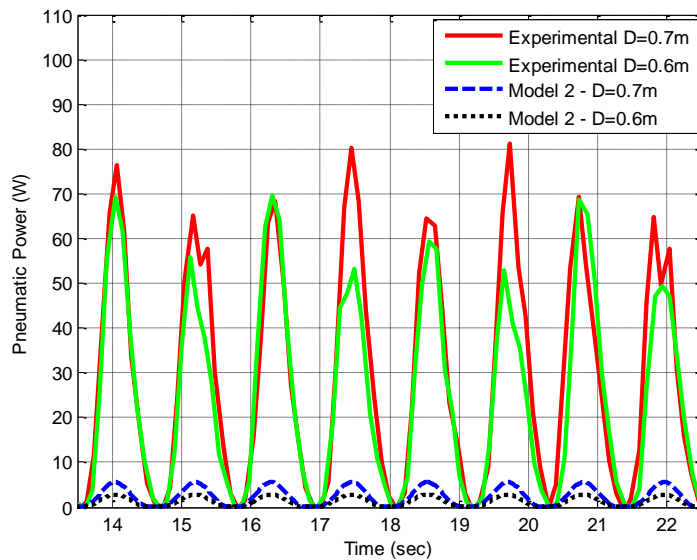


Figure 6-3: Pneumatic power for test $f=0.44\text{Hz}$ and $H_w=0.1\text{m}$ (scenario 1)

Looking at the comparisons of the pressure drop and the volumetric flow, it can be seen that the simulated results are substantially underestimated compared to the experimental results. A potential reason for these lower predictions is the larger damping provided by the orifice in model 2 than that experienced over the venturi flow meter. This is due to the experimental air flow having stages of decreased area from the air chamber to the venturi duct then through the venturi throat and vice versa. Despite the underestimation, the trend between the two water depths is maintained in the two sets of results.

The lower predictions of the pressure drop and volumetric flow rate compounds to a substantially lower pneumatic power comparison by the simulated model, shown in Figure 6-3. However the shape of the curves, especially with regards to the pressure drop is maintained between the experimental and simulated results. The adjustment of the simulated pneumatic power curve to match the experimental curve is a matter of scaling, which can be catered for using the loss coefficient K_{aux} . This will be dealt with at the end of this section.

Figure 6-4 below, shows the comparison between the simulated pneumatic power and the experimental pneumatic power for the lower wave height of $H_w = 0.05$ m. This comparison shows the significant underestimation of the simulated pneumatic power which is anticipated in knowledge of the decrease in wave power levels at the lower wave height. Section 6.3 discussed the issue of lower accuracy levels inherited from the low resolution of the gauge pressure transducers which are most prevalent at lower power ranges. The results shown in Figure 6-4 are substantially lower than the experimental pneumatic power results shown in Figure 6-3, making it more questionable in terms of the accuracy.

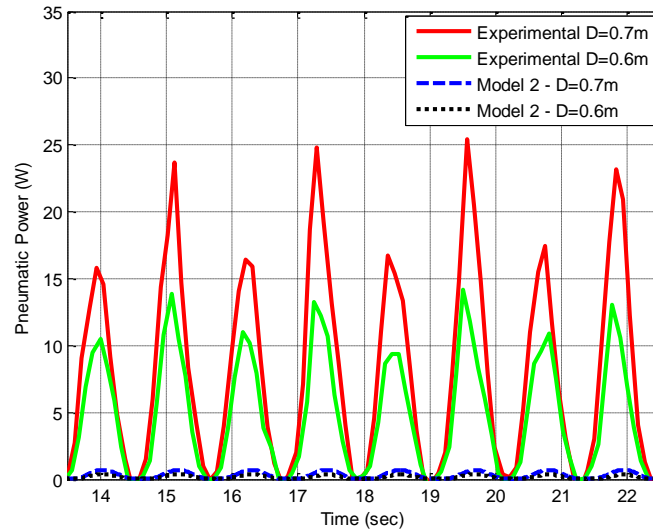


Figure 6-4: Pneumatic power for test $f=0.44$ Hz and $H_w=0.05$ m (scenario 1)

The second comparison discussed is for the higher test frequency of $f = 0.67$ Hz. Figure 6-5, Figure 6-6 and Figure 6-7 show the comparison of the pressure, volumetric flow rate and pneumatic power respectively with the simulation of model 2, for wave height $H_w=0.1$ m and frequency $f = 0.67$ Hz for the two water depths.

The results for the pressure drop and volumetric flow rate show a much closer correlation between experimental and simulated results, compared to that shown in Figure 6-1 and Figure 6-2 for the lower test frequency. There is a close comparison between the pressure drop results for the higher water depth without the presence of any scaling factors. This contributes to the close visual correlation

between the pneumatic power results for the higher water depth. The greater negative amplitudes compared to the positive amplitudes, witnessed especially for the experimental volumetric flow rate curve at $D=0.6$ m is likely due to the greater rate of air flowing back into the OWC box than that flowing out. This phenomenon was witnessed in the PIV testing by Ram et al (2010).

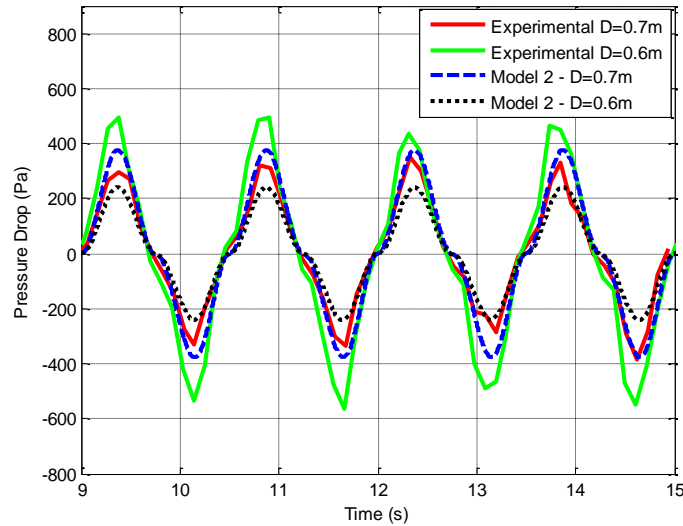


Figure 6-5: Pressure drop over venturi throat for test $f=0.67\text{Hz}$ and $H_w=0.1\text{m}$ (scenario 1)

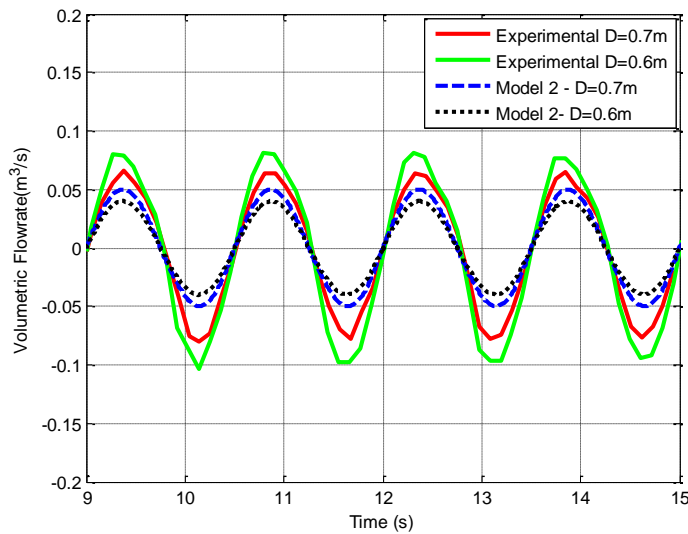


Figure 6-6: Volumetric flow rate for test $f=0.67\text{Hz}$ and $H_w=0.1\text{m}$ (scenario 1)

On analysis of Figure 6-7, it can be seen that the relative difference in pneumatic power results for the two water depths varies between the experimental and simulated results. This is not witnessed in any other results; therefore could be attributed to altered experimental conditions for this test set. Additionally, pneumatic power results for wave frequency $f=0.67$ Hz shows that the

experimental power measurement values are highest for water depth $D=0.6$ m whereas the simulated pneumatic power values are lowest for this water depth.

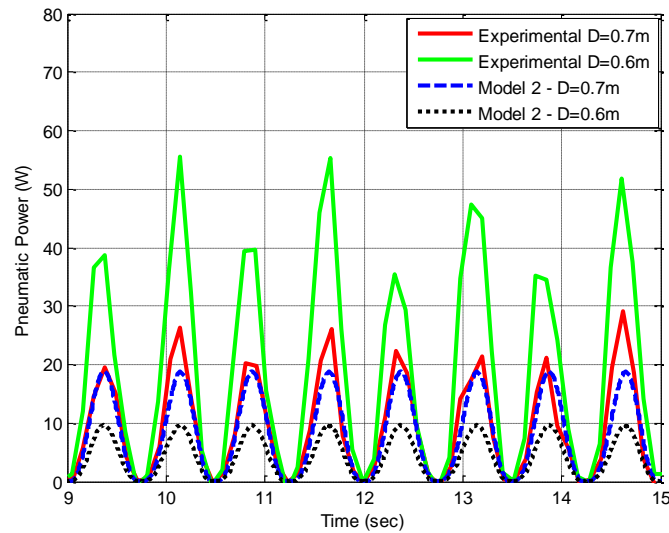


Figure 6-7: Pneumatic Power for test $f=0.67\text{Hz}$ and $H_w=0.1\text{m}$ (scenario 1)

Figure 6-8 below, shows the comparison between the simulated pneumatic power and the experimental pneumatic power for the lower wave height of $H_w=0.05$ m. Similarly to Figure 6-4, the simulated model heavily overestimates the pneumatic power for the lower test wave height.

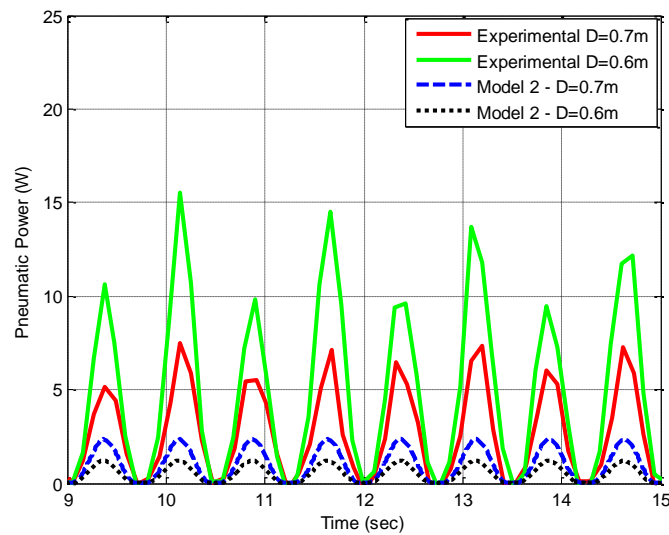


Figure 6-8: Pneumatic power for test $f=0.67\text{Hz}$ and $H_w=0.05\text{m}$ (scenario 1)

To build from the comparison of the simulated pneumatic power results of model 2 with that of the experimental results, the selection of the auxiliary loss coefficient K_{aux} for the adjustment of the simulated pneumatic power is discussed. The coefficient K_{aux} is sourced from Holtz (2007), where it was used

to account for unknown experimental flow losses in the simulation model. The effect that K_{aux} has on the simulated curves is that a positive value scales up the amplitude and a negative value scales down the amplitude. From the pneumatic power results shown above for scenario 1, it can clearly be seen that the simulated pneumatic power curves of model 2 are underestimated therefore a positive scaling factor is required. The shape of the curve is maintained through the implementation of the auxiliary loss coefficient. An acceptable range of the K_{aux} will be developed from the following analysis. When the experimental pneumatic power results have differences in amplitude within each oscillation, the K_{aux} value is selected to cater for an average between the two amplitudes.

For the simulated pneumatic power results of the lower test frequency, the values of K_{aux} applied ranged from 18.0 to 35.0 for the higher wave height. Even though there is an acceptable correlation between the experimental and simulated curves, shown in Figure 6-9, the large scaling range is an impractical method of accounting for the higher damping levels of the simulated model. The large range of the applied K_{aux} values is also witnessed for the lower wave height of the lower test frequency.

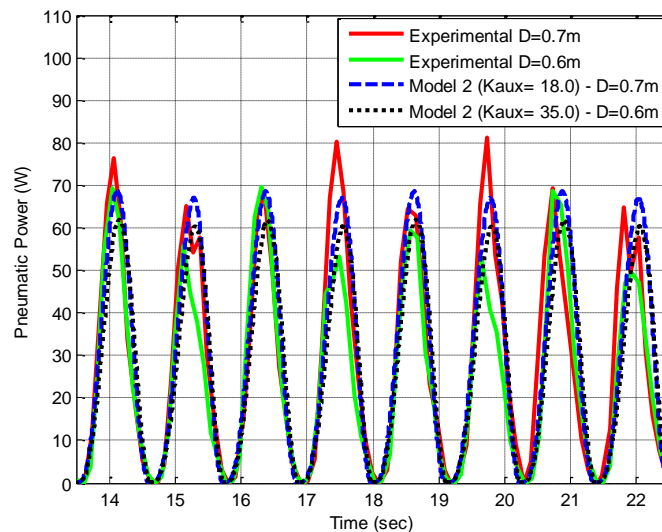


Figure 6-9: K_{aux} application on pneumatic power for test $f=0.44\text{Hz}$ at $H_w=0.1\text{m}$ (scenario 1)

Figure 6-10 and Figure 6-11 show the pneumatic power graphs for the higher frequency test parameter with a selected optimum K_{aux} value. For the water height $H_w=0.1\text{ m}$ the selected K_{aux} range is 0.4 to 4.0 for water depths $D=0.7\text{ m}$ and $D=0.6\text{ m}$ respectively. This is deemed to be an acceptable range for the scaling of the simulated pneumatic power results seeing that Holtz (2007) used a range of 0 to 2.0 in a more controlled and stable testing environment. For the water height $H_w=0.05\text{ m}$ the selected K_{aux} range is 2.6 to 13.0 for water depths $D=0.7\text{ m}$ and $D=0.6\text{ m}$ respectively. The significantly high K_{aux} value for water depth $D=0.6\text{ m}$ is deemed as being out of the acceptable range as a scaling factor.

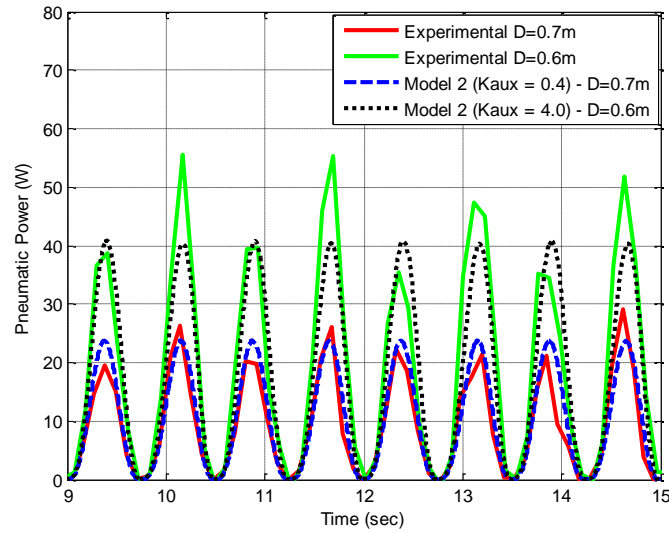


Figure 6-10: K_{aux} application on pneumatic power for test $f=0.67\text{Hz}$ at $H_w=0.1\text{m}$ (scenario 1)

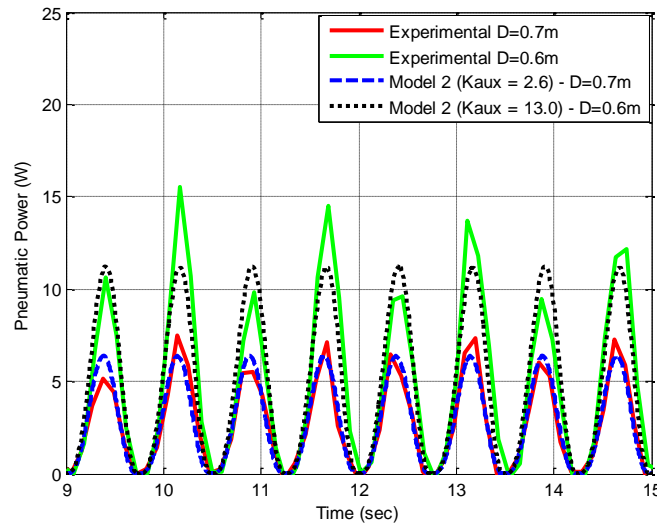


Figure 6-11: K_{aux} application on pneumatic power for test $f=0.67\text{Hz}$ at $H_w=0.05\text{m}$ (scenario 1)

As a summary for the scaling of the simulated pneumatic power curves, the high level of underestimation for the simulated pneumatic power at the lower wave frequency parameters is quite substantial for an acceptable K_{aux} value to be implemented. For the higher wave frequency parameters, a closer correlation between the experimental and simulated pneumatic power curves rendered a lower and more satisfactory K_{aux} scaling range. The K_{aux} range of 0.4 to 4.0 was considered to be appropriate for the application with the simulated air-flow model. Further observation showed that larger K_{aux} values were required to adjust the simulated pneumatic power results for water depth $D=0.6$ m compared to water depth $D=0.7$ m. From this basic analysis of the K_{aux} implementation, it

is possible for a trial and error method to be used on the simulation results so that the amplitude difference between the simulated and experimental curves are minimised. This is a high level approach to accounting for the unexpected losses which have not been catered for in the simulation models.

6.3.2. Scenario 2 – Model 2 (Experimental OWC input)

In scenario 2 of the comparative analysis, model 2 is compared with the experimental pneumatic power results using the experimental water column displacement to replace the sinusoidal input $h_w(t)$. The auxiliary coefficient values for scenario 2 are re-analysed for each test performed in the analysis.

The following figures (Figure 6-12 and Figure 6-13) show the experimental water column displacement curves according to the two input wave heights and two water depths for the test frequencies selected in the comparative analysis.

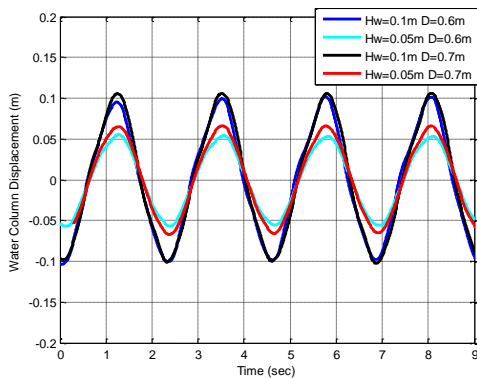


Figure 6-12: Experimental water column displacement for $f=0.44\text{Hz}$

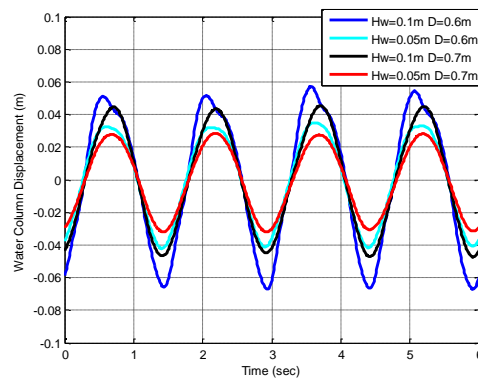


Figure 6-13: Experimental water column displacement for $f=0.67\text{Hz}$

The graphs above show that for the lower frequency, there is resonance present where the measured water column displacement is almost double the input wave height to the wave maker. For this lower wave frequency, there is no significant difference between the measured wave heights over the two water depths. For the higher frequency of $f=0.67\text{ Hz}$, the measured wave heights are representative of the input wave heights to the wave maker. Over the two water depths, there is a higher wave height recorded for the lower water depth $D = 0.6\text{ m}$.

The results of the comparative analysis for scenario 2 are shown below in Figure 6-14 and Figure 6-15 for the lower and higher frequencies tested in the wave flume. Only, the larger wave height $H_w=0.1\text{m}$ test results are compared in this scenario due to the prevailing inaccuracies associated with the measurement ranges at lower wave heights.

From Figure 6-14, there is a considerable distortion of the simulated pneumatic power curve for the lower wave frequency coupled with the larger water column displacement. Even though the amplitude of the pneumatic power can be aligned between the experimental and simulated values, there is a significant difference

between the shape of the curves. The substantially higher experimental wave heights for wave frequency $f=0.44$ Hz, revealed in Figure 6-12, play a role in this distortion from the simulation model for this lower frequency only. The K_{aux} scaling values range from 0 to 3.5 for the higher wave height, shown below, and 1.0 to 4.0 for the lower wave height. This is in line with the acceptable scaling range previously discussed.

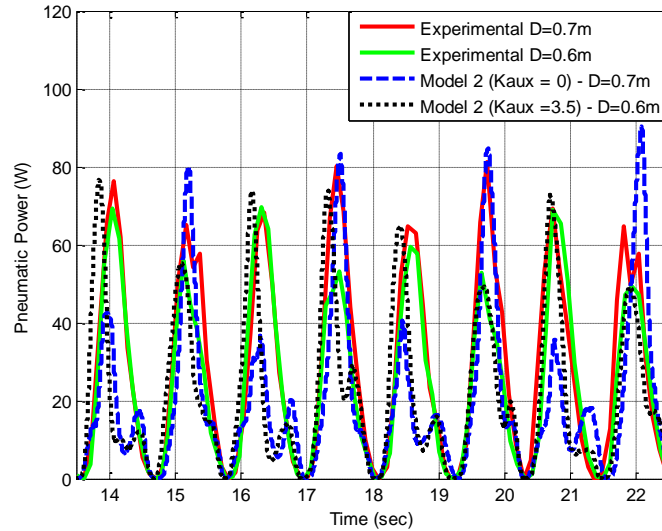


Figure 6-14: Pneumatic power comparison for test $f=0.44$ Hz and $H_w=0.1$ m (scenario 2)

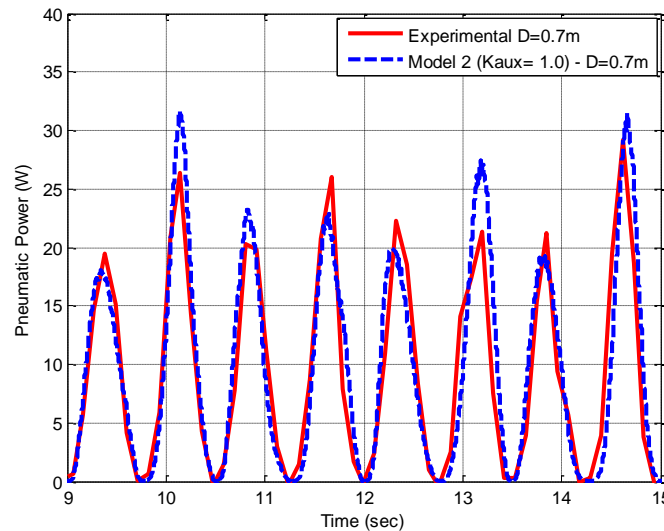


Figure 6-15: Pneumatic power comparison for test $f=0.67$ Hz and $H_w=0.1$ m (scenario 2)

Results for wave frequency $f=0.66$ Hz at water depth $D=0.7$ m only, given in Figure 6-15, shows that no distortion is present in the simulated pneumatic power curve. There is also a close correlation in the shape of the curves but there is marginal variance in the power amplitude values, which is accounted for with a K_{aux} value of 1.0.

6.3.3. Scenario 3 – Model 3

This final scenario is the most developed of the simulated models which utilises the experimental water column input and the experimental difference in pressure over the venturi throat. However this model is an approximation of the venturi flow meter's operation due to no viscous and turbulent losses being taken into account. The same test parameters stated in scenario 2 are used in the comparative analysis of scenario 3. Additionally, the simulation of model 3 is performed without the use of the K_{aux} scaling factors, as seen in scenario 1 and 2, due to the venturi flow meter equation being applied in the model and not the pipe flow equation.

Comparative analysis from scenario 3 revealed a great variance in the simulated pneumatic power results with the input of the unsteady experimental pressure drop values and volumetric flow rate of the venturi flow meter equation. Figure 6-16 shows the comparison of the pneumatic power for frequency $f=0.67$ Hz at the higher wave height. Figure 6-17 shows how the simulated pneumatic power output varies in amplitude over each oscillation for both water depths of the lower test frequency. These results show the difficulty in finding good correlation between the curves given the constant change in amplitude. Additionally, the model doesn't take into account accuracy issues incurred at low flow rates, which the experimental design of the measurement device has catered for. A more detailed analytical model needs to be created to allow for better prediction of the venturi operation of the pneumatic power measurement device.

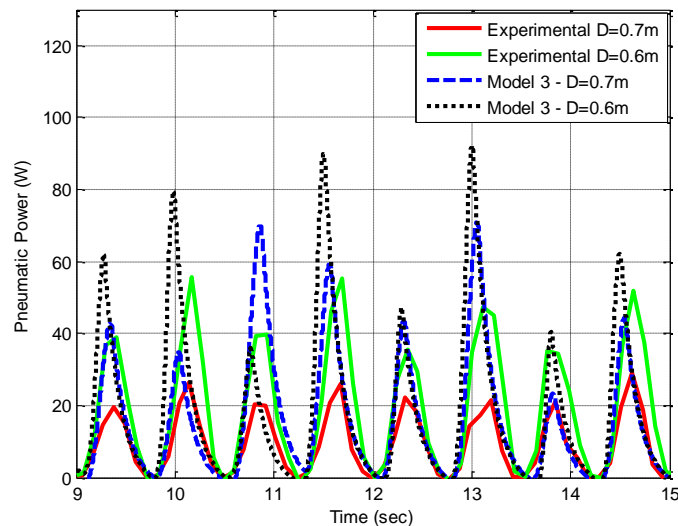


Figure 6-16: Pneumatic power for test $H_w=0.1m$ $f=0.67Hz$ (scenario 3)

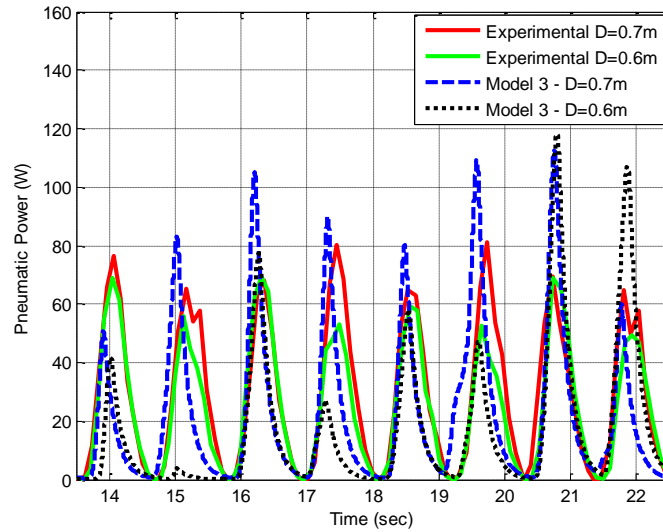


Figure 6-17: Pneumatic power for test $H_w=0.1\text{m}$ $f=0.44\text{Hz}$ (scenario 3)

6.4. Examination of the wave flume experimental results

Following the comparative analysis of the pneumatic power measurement device, the pneumatic power results for the range of the testing schedule is briefly examined below. Results excluded from the comparative analysis such as the results from water depth of 0.5 m and the larger wave height tests are included in this investigation.

6.4.1. Resonance

The selected theories behind water column resonance approximation, described in section 2-8, are utilised for natural frequency calculation. This allows theoretical approximations of the water column natural frequencies to be compared with the average pneumatic power analysis, which is to follow. Table 6-3 details the natural frequency approximation for the constructed OWC model according to three water depth encountered during the wave flume tests.

Table 6-3: Natural frequency approximation for OWC model

Natural frequency model	Water Depth D (m)	Natural Frequency f_c (Hz)
McCormick (1981) $f_c = \frac{1}{2\pi} \sqrt{\frac{g}{L_1 + L'_1}}$	0.5	0.54
	0.6	0.49
	0.7	0.46
Veer & Thorlen (2008) $f_c = \frac{1}{2\pi} \sqrt{\frac{g}{L_d + 0.415^{1/2}}}$	0.5	0.59
	0.6	0.55
	0.7	0.52
Horko (2007) $f_c = \frac{1}{2\pi} \sqrt{\frac{g}{d_{ip} + \frac{\pi B}{2}}}$	0.5	0.49
	0.6	0.46
	0.7	0.45

The three natural frequency models show an inverse relationship between the water depth and natural frequency. Veer & Thorlen's (2008) approximation shows a higher estimation range which can be attributed to the cross sectional areas being taken into account, for larger water columns.

6.4.2. Average Power

The average power output derived from the post-processed pneumatic power results is compared below. The average power was analysed for ten oscillations (nine oscillations if data not available) at each test so that an impartial comparison could be made between the testing parameters. Figure 6-18 shows the results of the average pneumatic power for the tests performed at water depths $D=0.5\text{m}$, $D=0.6\text{m}$ and $D=0.7\text{m}$ for the wave six wave frequencies between $f=0.67\text{ Hz}$ to $f=0.33\text{ Hz}$. Results for $f=0.3\text{ Hz}$ and $H_w=0.1\text{ m}$ are not taken into account for both water depths. This rendered unsatisfactory results due to intense sloshing experienced in the water column, which results from a greater front-lip submergence depth at the lower frequency.

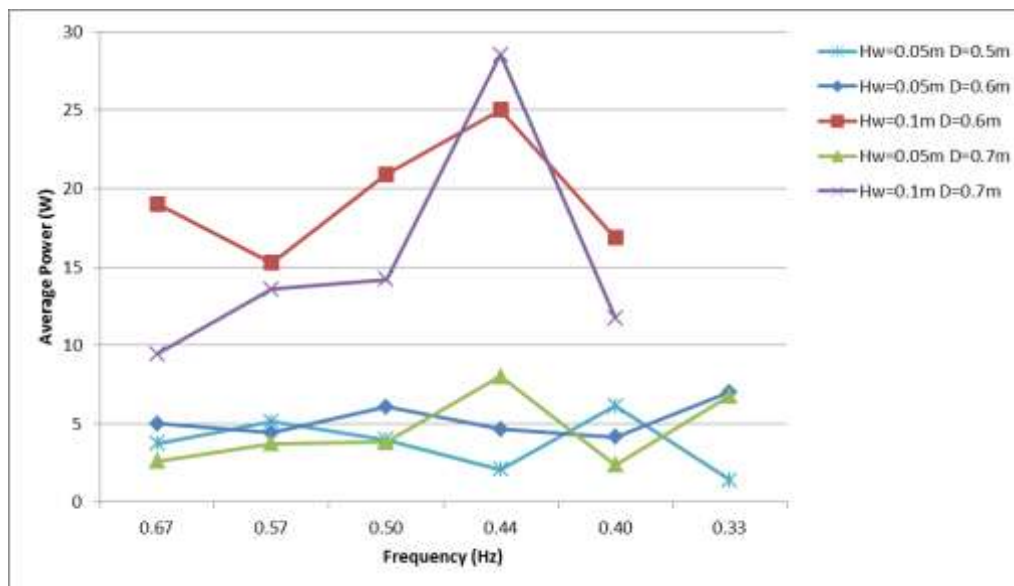


Figure 6-18: Comparison of the average pneumatic power

The comparison shows the different average pneumatic power ranges which are present for the change in water depth. The average pneumatic power values for the higher wave height ranges between 9 and 30 W and for the lower wave height between 1 and 8 W. Figure 6-18 reveals the trend of a higher pneumatic power result for water depth $D=0.6\text{ m}$ for each frequency over a constant wave height. This can be attributed to, specifically for the higher wave height, the energy being the greatest at the surface of the water, which applies to the lower water depth of 0.6 m. This facilitates energy entering the water column and it minimises reflection of the front wall.

In terms of resonant frequencies, the results for $H_w=0.1$ m show a clear peak in average pneumatic power for a frequency of 0.44 Hz. This is in the region of McCormick's (1991) and Horko's (2007) resonant frequency approximation for the two higher water depths. For $H_w=0.05$ m, there is no distinct resonant frequency trend present which can be attributed to the low pneumatic power values and the high effects of measurement inaccuracies at these low values.

For the larger wave heights ($H_w=0.125$ m and $H_w=0.15$ m) that were tested, the average pneumatic power was analysed for 8 oscillations. These extreme tests were performed for two wave heights and two frequencies. The selected frequencies were chosen from prior results recorded where resonant activity appeared to take place. These larger wave height tests proved to show significant amounts of sloshing in the water column, a high level of water reflection in the tank and wave overtopping of OWC model. The pneumatic power results for these larger wave heights are shown in Appendix F. Table 6-4 shows the average pneumatic power recordings for the larger wave heights. For $H_w=0.125$ m, the increase in average power from wave height $H_w=0.1$ m is 62 % for $f=0.5$ Hz and 44 % for $f=0.44$ Hz. The largest wave height tested during this research study showed a substantial increase in the average pneumatic power, with a 112 % increase compared to results at wave height $H_w=0.1$ m and 47 % increase compared to results at wave height $H_w=0.125$ m.

Table 6-4: Average Pneumatic Power for larger wave heights

Frequency f (Hz)	Average Pneumatic Power (W)	
	$H_w = 0.125$ m	$H_w = 0.15$ m
0.50	34	-
0.44	36	53

6.4.3. Efficiency

The wave to pneumatic efficiencies, shown in Table 6-5 below, are calculated using the measured average pneumatic power per oscillation and the calculated incident wave power on the 1m face of the OWC model. The efficiency is calculated using equation 2-12 for wave height $H_w=0.1$ m and water depth $D=0.6$ m.

Table 6-5: Efficiency calculation for $D=0.6$ m and $H_w=0.1$ m

Wave frequency (Hz)	Incident wave power at $D=0.6$ m (W)	Average wave power at $D=0.6$ m (W)	Efficiency (%)
0.67	16.5	1.9	12%
0.57	20.0	1.5	8%
0.50	14.1	2.1	15%
0.44	14.4	2.5	17%
0.40	29.1	1.7	6%

The efficiency results show an overall low energy conversion ratio which is common with OWC devices and is also shown in Mendes & Monteiro's (2007) overall efficiency results. The peak efficiency at frequency $f=0.44\text{Hz}$ correlates well with the resonant frequency estimations shown in Table 6-3.

6.5. Conclusions

The developed pneumatic power measurement device was tested in a wave flume with an OWC device for a range of testing parameters. The tests that were performed include closed roof tests, roof with an orifice tests and the primary tests which involved the measurement device placed upon the orifice of the OWC model. It was noted that the size of the orifice plays a major role in the damping of the air-flow system. The results from the wave flume tests were post-processed according to the measuring equipment specifications and the results from the calibration tests. These were then used for analysis and use with the simulation model results.

An important consideration in the development of the pneumatic power measurement device is the equipment accuracy which is shown to be within the satisfactory range of 3 % of the FSO. The resolution of the gauge pressure transducer has been highlighted as a source for error especially in low pressure drop situations. The selection of this type and rating of the pressure transducer has been justified due to the range of testing parameters being tested.

The comparative analysis provided a platform for comparing the experimental pneumatic power with the simulation of analytical models of growing complexity (scenario 1 to 3). Results from scenario 1 shows that most of the pressure drop and volumetric flow rate comparisons have substantial similarities in amplitude and shape. The pneumatic power curve shapes are maintained between the experimental and simulation models; however this is not the case regarding the amplitude. The auxiliary coefficient is added to the simulation system to provide scaling capabilities of the pneumatic power, which allows substantially better matching of the curves. Results from scenario 2 show how the water column displacement differs from the input wave height due to the presence of resonance. Average power analysis confirmed resonant activity at $f=0.44\text{ Hz}$. Scenario 3 shows how the simulation of the venturi system delivers varying pneumatic power results and has no basis for proper comparative analysis. This has been attributed to the lack of compensation for low flow rate inaccuracies in the simulation model and the absence of viscous and turbulent loss terms.

The results from the pneumatic power measurement device has shown that the pneumatic power in an OWC model can be measured but with a varying level of accuracy between test parameters. This is due to difficulty in accurately modelling the bidirectional and oscillating air-flow system of the OWC system, especially with a one dimensional analytical model. Considerable improvements in the simulation models could be achieved through analysing the air-flow system operation using CFD tools.

7. Conclusions and recommendations

A measurement platform for OWC model testing, with regard to the pneumatic power generated, is required to quantify its operational performance. This is achieved in the research study through the design, construction and assembly of a pneumatic power measurement device for an OWC model.

The design of the measurement device was intended for the unsteady and bidirectional air-flow characteristics found in OWC systems. The literature study allowed insight into previous OWC related air-flow measurement devices and additional air-flow devices used in experimental tests. This highlighted factors such as low-flow rate inaccuracies, correct selection of the pressure transducers and the suitability of flow meters to oscillating and bidirectional flow. The design of the pneumatic power measurement device is primarily based upon the venturi flow meter system which has been manipulated in accordance with international standards. The use of a single device to measure the pressure drop and volume flow rate simplifies the testing set-up and makes it possible for the device to be implemented on different OWC platforms.

The calibration of the pneumatic power measurement device before testing with the OWC model was a fundamental step in ensuring that the recorded measurements were processed accurately. It enabled the exact tuning of the measurement equipment before the wave flume testing stage. The conclusions from the calibration tests established that the calibrated curve for the volumetric flow rate measurement had an error of less than 3% relative to the actual wind tunnel volumetric flow rate curve. This was deemed satisfactory and in-line with calibration test results documented in the literature survey. The calibration tests also proved that there were no air-leaks in the pneumatic power measurement device.

The simple design of the Perspex OWC model allowed easy construction of the model and also facilitated the development of an analytical model of the air-flow in the constructed OWC model. The analytical models provided investigation of the air-flow through an OWC device but proved difficult to accurately do so due to the complex bidirectional and oscillating environment. The auxiliary loss coefficient K_{aux} provided a better correlation of the simulated pneumatic power to the experimental pneumatic power. An acceptable range of this scaling coefficient was deemed to be from 0 to 4.

The experimental results showed that the pneumatic power measurement device could measure the pneumatic power in the bidirectional and oscillating air-flow environment. Improvements to the system were noted, such as the resolution levels of the gauge pressure transducer, which brings about inaccuracies in the pneumatic power results. This phenomenon was seen during the comparative analysis shown in scenarios 1 and 2. The pneumatic power measuring device was designed to test at a variety of testing parameters therefore there was room for

inaccuracy at certain parameters, such as the lower wave heights. The pneumatic power measurement device is more suited to accurately measure the pneumatic power at higher wave heights due to the higher measurement ranges encountered.

In conclusion, the completion of this research study creates stepping stone for developing an accurate pneumatic power measuring device for the oscillating and bidirectional air-flow of an OWC model. Revised and validated versions of the designed, constructed and assembled measuring device can be advanced to facilitate the validation of future OWC concepts and determine whether they are worthy for further research and development.

Recommendations

The following points are recommendations for further research into the domain of pneumatic power measurement in OWC systems:

- The existing pneumatic power measurement device should be revised in terms of making it specifically designed for lower power and higher pneumatic power ranges. This should be in accordance with the characteristics of measuring equipment, such as the gauge pressure transducers, which can be changed to differential pressure transducers for substantially lower power measurements.
- Future OWC models should be designed and constructed so that the ratio of the width and the height of the water column are smaller. This promotes planar movement of the water column so that it better resembles a solid piston. The volume of the air chamber should also be minimised so that higher air pressure ranges are attained during experimental testing.
- CFD tools should be implemented for analysis of the complex air-flow system in an OWC device. The results of a CFD model and a secondary power measuring device can be incorporated with the revised pneumatic power measuring device so that a fitting validation platform can be created for the device.
- The revised and validated pneumatic power measurement device can be used to find an optimum geometry of a specific model during wave flume tests, according to the pneumatic performance of the OWC device/model.

8. References

- Ackerman, P.H. October 2009. *Air Turbine Design Study for a Wave Energy Conversion System*. Unpublished MSc Eng thesis. Stellenbosch University, Stellenbosch.
- ASME. 1971. *Flow Meters, Theory and Applications*. 6th Edition. American Society of Mechanical Engineers. New York.
- ASME. 1985. *Measurements of fluid flow in pipes using orifice, nozzle and venturi*. ASME standard MFC-3M-1985. American Society of Mechanical Engineers. New York.
- Allen, K. 2012. Personal Communication. August 2012, Stellenbosch University.
- Bascom, W. 1980. *Waves and beaches*. Anchor Books: New York.
- Boake, C. B, Whittaker, T.J.T, Folley, M & Ellen, H. 2002. May 2002. *Overview and Initial operational experience of the LIMPET Wave Energy Plant*. Paper presented at the 12th International Offshore and Polar Engineering Conference in Kitakyushu, Japan.
- Boud, R. 2003. *Status and Research and Development Priorities, Wave and Marine Accessed Energy*. UK Department of Trade and Industry (DTI) Report.
- Brumbley, D.R & Arbas, E.A. 1979. An inexpensive hot-wire anemometer suitable for behavioural research. *Comparative biochemistry and physiology*, 64A: 449-450.
- Carrington, C.G, Marcinowski, A & Sandle, W.J. 1981. A simple volumetric method for measuring airflow. *Journal of Physics E: Science Instruments*, 15.
- Çengel, Y. A. & Cimbala, J. M., 2010. *Fluid Mechanics: Fundamentals and Applications*. 2nd Edition. New York: McGraw-Hill.
- Dizadji, N. & Sajadian, S. E., 2011. Modeling and Optimization of the Chamber of OWC System. *Energy*, 36: 2360-2366.
- DME. 2003. *White paper on renewable energy*. Department of Minerals and Energy.
- Evans, D. V. & Porter, R. 1995. Hydrodynamic Characteristics of an Oscillating Water Column Device. *Applied Ocean Research*, 17: 155-164.
- Figliola, R.S & Beasley, D.E. 2006. *Theory and Design for Mechanical Measurements*. John Wiley & Sons, Inc.
- Fox, R.W, Pritchard, P.J & McDonald, A.T. 1999. *Introduction to fluid mechanics*. 7th Edition. Wiley: New York.

- Hayward, A.T.J. 1979. *Flowmeters*. The MacMillan Press LTD: London and Basingstoke.
- Heath, T.V. 2012. A review of oscillating water columns. *Philosophical transactions of the Royal Society A* 2012, 370: 235-245.
- Heeley, D. 2005. *Understanding pressure and pressure measurement*. [Online]. Available: http://www.freescale.com/files/sensors/doc/app_note/AN1573.pdf. [2012 March 20].
- Holtz, M.W. 2007. *Modeling and Design of a Novel Air-Spring for a Suspension Seat*. Unpublished MSc Eng thesis. Stellenbosch University, Stellenbosch.
- Horko, M. 2007. *CFD optimisation of an oscillating water column wave energy converter*. University of Western Australia.
- HR Wallingford. 2010. *Flume wave generation system EQ1021*. User manual prepared for Stellenbosch University.
- Islay Limpet Wave Power Plant*. 2002. The Queen's University of Belfast.
- ISO 5167-1:1991. 1991. Measurement of fluid flow by means of pressure differential devices Part 1. *International Organisation for Standardisation*.
- Jayashankar, V, Jagadeesh Kumar, V & Ravindram, M. 1997. *Probe for measurement of air velocity in oscillating flows*. Proceedings from IEEE Instrumentation and Measurement Technology Conference in Ottawa, Canada.
- Jorgensen, F.E. 2002. *How to measure turbulence with hot-wire anemometers*. [Online]. Available: <http://www.dantecdynamics.com/docs/support-and-download/research-and-education/practicalguide.pdf>. [2012, May 10]
- Krogstad, H.E & Arntsen, O.A. 2000. *Linear Wave Theory Part A – Regular Waves*. Norwegian University of Science and Technology.
- Liu, Y, Shi, H, Liu, Z & Ma, Z. 2011. Experiment study on a new designed OWC caisson breakwater. Proceedings from IEEE Power and Energy Engineering Conference in Asia Pacific.
- Lu, Z.C & Lau, A. 2008. *Low cost bi-directional flow sensor using back-to-back pitot tubes*. The University of Auckland undergraduate mechatronics research journal, Volume 1, pp. 16-20.
- Matlab. 2010. Matlab R2010a Simulink.
- Marsh, G. 2009. *Maximising the power of waves*. Renewable Energy Focus.

- McCormick, M. E. 1981. *Ocean Wave Energy Conversion*. New York: Wiley-Inter-Science.
- Mendes, A.C & Monteiro, W.M.L. 2007. *Performance analysis of a model of OWC energy converter in non-linear waves*. Proceedings from the 7th European Wave and Tidal Energy Conference in Porto, Portugal.
- Muetze, A & Vining, J.G. 2006. *Ocean Wave Energy Conversion – A Survey*. Electrical and Computer Engineering Department, University of Wisconsin-Madison.
- Müller, F.P.J. & Retief, G. 2011. Personal Communication. May 2013, Stellenbosch.
- OES-IA. 2009. *Ocean Energy Systems International Agreement: Annual Report 2009*.
- Patterson, C, Dunsire, R, Hillier, S. 2010. *Development of Wave Energy Breakwater at Siadar, Isle of Lewis*.
- Ram, K, Faizal, M, Rafiudin Ahmed, M & Lee, Y.2010. Experimental studies on the flow characteristics in an oscillating water column device. *Journal of Mechanical Science and Technology* 24(10): 2043-2050.
- Rea, M. 2008. Wave tank and wave maker design. *Springer: Ocean Wave Energy – Current status and future perspectives*. 147-159.
- Retief, G. de. F., Prestedge, G.K. & Müller, F, P, J, 1982. A Proposal for wave energy conversion near Cape Town. Proceedings from the *18th ICCCE conference* 1: 245-260, Cape Town, South Africa.
- Retief, G. 2006. *Wave power in the Western Cape* [Presentation].
- Ross, D. 1979. *Energy from the waves*. Pergamon Press Ltd.: Oxford, England.
- Sarmiento, A.J.N.A. 1992. Wave flume experiments on two-dimensional oscillating water column wave energy devices. *Experiments in fluids*, 12: 286-292.
- Sarmiento, A.J.N.A & Falcao, A.F. de O. 1985. Wave Generation by an Oscillating Surface Pressure and its Application in Wave Energy Extraction. *Journal of Fluid Mechanics*, 150: 467-485.
- SolidWorks. 2010. SolidWorks 2010 x64 Edition.
- South African Yearbook 2010/2011. 2011. *Energy*. [Online]. Available: <http://www.gcis.gov.za/sites/default/files/docs/resourcecentre/yearbook/chapter8.pdf>. [2012, October 27]

- Thiruvenkatasamy, K. & Neelamani, S. 1997. On the efficiency of wave energy caissons in array. *Applied Ocean Research*, 19: 61-72.
- Thorpe, T.W. 1999. *Wave power: moving towards commercial Viability*. Broadway House, London.
- Torre-Enciso, Y, Ortubia, I, Lopez de Aguilera, L.I & Marques, J. 2009. *Mutriku wave power plant: from the thinking out to the reality*. Proceedings of the 8th European Wave and Tidal Energy Conference in Upsala, Sweden.
- Tseng, R, Wu, R & Huang, C, 2000. Model study of a shoreline wave-power system. *Ocean Engineering*, 27: 801-821.
- Van Niekerk, J.L & Joubert, J.R. 2010. *Wave Energy Converters (WEC's)*. Centre for Renewable and Sustainable Energy Studies.
- Veer, R.v & Thorlen, H.J. 2008. *Added resistance of moonpool in calm water*. The ASME 27th International Conference on Offshore Mechanics and Arctic Engineering in Estoril, Portugal.
- Wavegen. 2002. *Research into the further development of the LIMPET shoreline wave energy plant*. DTI, V/06/00183/00/Rep.
- White, F.M. 2008. *Fluid Mechanics*. 6th Edition. New York: McGraw-Hill.
- Whittaker, T.J.T. 2006. *Energy 2100 Wave Power Technology* [Presentation]. The Queen's University of Belfast.

A. Derivation of air-flow models

The constants that are used in the three air-flow models are restated in Table A-1. The design ambient temperature conditions of 15°C was chosen since it was the actual ambient temperature of the wave flume building during experimental testing.

Table A-1: Constants used for the air-flow models

Description	Constant	Value	Units
Universal gas constant	R	287	J/kg.K
Specific heat at constant pressure	C_p	1005	J/kg.K
Specific heat at constant volume	C_v	718	J/kg.K
Ambient Temperature @ 15°C	T_a	288	K
Atmospheric Pressure @ 15°C	P	101 325	Pa
Density of air at ambient conditions	ρ	1.23	kg/m ³
Viscosity of air at ambient temperature	μ	1.79E-5	N.s/m ³

A.1. Model 1 - Closed-roof OWC model

The state equations are derived for the closed chamber model (model 1), where control volume 1 (CV₁), from figure A-1, represents the oscillating air chamber of the OWC model.

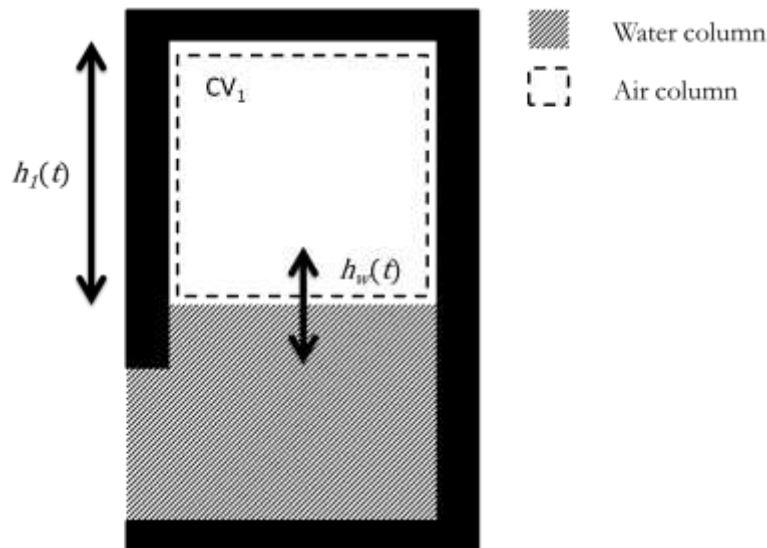


Figure A-1: Sectional view of the closed chamber OWC model

Where: $h_1(t)$ is the air chamber length

$h_w(t)$ is the water column displacement

The assumptions for the theoretical analysis of this model are as follows:

- The system is adiabatic and reversible (i.e. isentropic)
- The air of the OWC model's air chamber is treated as an ideal gas
- There are no losses due to friction

For the closed chamber model of CV₁, the theory of continuity of mass is applied. Since no mass flow rate will be present in this model the following continuity of mass is known:

$$\frac{dm_1}{dt} = \dot{m}_{1,in} - \dot{m}_{1,out} = 0 \quad (\text{A-1})$$

$$\text{Therefore, } \dot{m}_1 = 0 \quad (\text{A-2})$$

Using the ideal gas law of equation 4-1 on CV₁, the rate of air pressure change can be described.

$$p_1(t)v_1(t) = m_1(t)RT_1(t) \quad (\text{A-3})$$

Differentiating the ideal gas equation with respect to time and using the volume of the air chamber (equation A-4) yields equation A-5.

$$v_1(t) = A_1h_1(t) \quad (\text{A-4})$$

$$p_1(t)A_1\dot{h}_1(t) + A_1h_1(t)\dot{p}_1(t) = \dot{m}_1(t)RT_1 + m_1(t)R\dot{T}_1(t) \quad (\text{A-5})$$

Using the mass flow rate relationship from equation A-2 in equation A-5, the state $\dot{p}_1(t)$ is found:

$$\dot{p}_1(t) = \frac{m_1(t)R\dot{T}_1(t)}{A_1h_1(t)} - \frac{h_1(t)p_1(t)}{h_1(t)} \quad (\text{A-6})$$

The energy balance for the closed chamber system can be solved by applying the law of conservation of energy below.

$$E(t) = Q(t) - W(t) \quad (\text{A-7})$$

Where, $E(t)$ is the total energy of the system

$Q(t)$ is the thermal energy

$W(t)$ is the work done by the system

Assumed isentropic process therefore equation A-7 breaks down into the following (assuming change in potential and kinetic energy in CV₁ is zero):

$$\Delta E(t) = \Delta U(t) = m_1(t)C_v\Delta T_1(t) \quad (\text{A-8})$$

$$\Delta Q(t) = 0 \quad (\text{A-9})$$

$$\Delta W(t) = p_1(t)A_1\Delta h_1(t) \quad (\text{A-10})$$

$$\therefore m_1(t)C_v\Delta T_1(t) = -p_1(t)A_1\Delta h_1(t) \quad (\text{A-11})$$

Dividing the expression by Δt and letting the limit tend to zero to solve for expression for temperature $T_1(t)$:

$$T_1(t) = -\frac{p_1(t)A_1\Delta h_1(t)}{m_1(t)C_v} \quad (\text{A-12})$$

Substituting equation A-12 into equation A-6, the state equation for the rate of pressure change in the air chamber of model 1 is derived.

$$\dot{p}_1(t) = -\frac{R}{C_v} \frac{\dot{h}_1(t)p_1(t)}{h_1(t)} - \frac{\dot{h}_1(t)p_1(t)}{h_1(t)} \quad (\text{A-13})$$

$$\dot{p}_1(t) = -\left[1 + \frac{R}{C_v}\right] \frac{\dot{h}_1(t)p_1(t)}{h_1(t)} \quad (\text{A-14})$$

The following table (Table A-2) describes the state equations defined for model 1.

Table A-2: State equations for model 1

State equations for the model 1	
Pressure	$\dot{p}_1(t) = -\left[1 + \frac{R}{C_v}\right] \frac{\dot{h}_1(t)p_1(t)}{h_1(t)}$
Air chamber height	$h_1(t) = L_a - h_w(t)$
	$h_w(t) = A \sin \omega t$ L_a = Initial height of air chamber A = Amplitude of water column displacement
Air chamber speed	$\dot{h}_1(t) = -A\omega \sin \omega t$
States	$\dot{p}_1(t), h_1(t), \dot{h}_1(t)$

A.2. Model 2 - OWC model with an orifice

The second model (Figure A-3) describes a general OWC model with an orifice on its roof (model 2). The two control volumes which are analysed in this model are the air chamber, represented by control volume 1 (CV_1) and the orifice volume, represented by control volume 2 (CV_2). The air chamber has an area A_1 and the orifice has an area A_2 . The diameter of the orifice determines how much damping is placed on the volumetric flow rate of air into and out of the chamber. The size of the orifice can be varied to determine the level of damping due to viscous losses at the orifice (Evans & Porter, 1995).

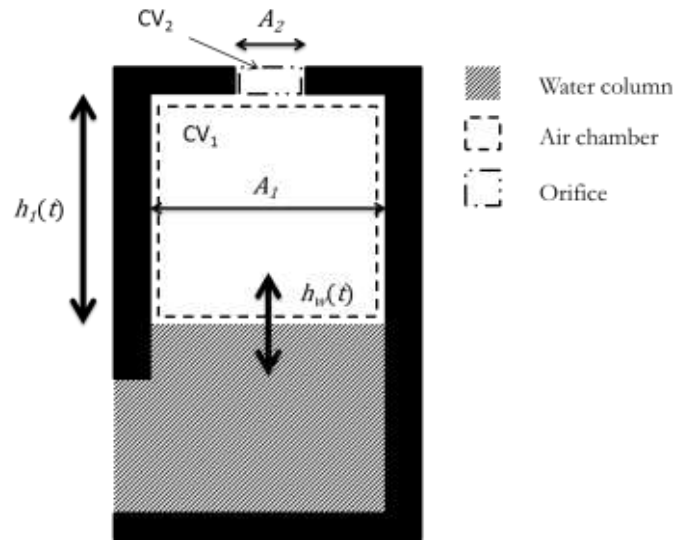


Figure A-3: Diagram of the OWC model with an orifice on the roof

The assumptions for the theoretical analysis of this model are as follows:

- The system is adiabatic and reversible (i.e. isentropic)
- The air of the OWC model's air chamber is treated as an ideal gas
- Mass flow of air present in the model
- There are no losses due to friction
- Unsteady flow

For CV_1 , the theory of continuity of mass is applied.

$$\text{Expansion of air pocket: } m_i = \Delta m_{cv1} \text{ or,} \quad (\text{A-15})$$

$$\text{Compression of air pocket: } -m_o = \Delta m_{cv1} \quad (\text{A-16})$$

$$\text{Therefore, } \frac{dm_{cv1}}{dt} = \pm \dot{m}_1 \quad (\text{A-17})$$

Equation A-6 is derived again by differentiating the ideal gas law and using the new continuity of mass relation for model 2.

$$p_1(t)v_1(t) = m_1(t)RT_1(t)$$

$$v_1(t) = A_1h_1(t)$$

$$p_1(t)A_1\dot{h}_1(t) + A_1h_1(t)\dot{p}_1(t) = \dot{m}_1(t)RT_1(t) + m_1(t)R\dot{T}_1(t)$$

$$\dot{p}_1(t) = \frac{\dot{m}_1(t)RT_1}{A_1h_1(t)} + \frac{m_1(t)R\dot{T}_1(t)}{A_1h_1(t)} + \frac{p_1(t)\dot{h}_1(t)}{h_1(t)} \quad (\text{A-18})$$

Substituting the relationship from the ideal gas equation (below) into equation A-18, the state $\dot{p}_1(t)$ is found:

$$\frac{RT_1(t)}{A_1h_1(t)} = \frac{p_1(t)}{m_1(t)}$$

$$\dot{p}_1(t) = \frac{\dot{m}_1(t)p_1(t)}{m_1(t)} + \frac{m_1(t)R\dot{T}_1(t)}{A_1h_1(t)} - \frac{\dot{h}_1(t)p_1(t)}{h_1(t)} \quad (\text{A-19})$$

Expanding from the law of conservation of energy given in equation A-7, $E(t)$ is broken up into the internal energy $U(t)$ summed with the energy of the mass that is exchanged from the control volume $\Delta E(t)$.

The law of conservation of energy now becomes:

$$U(t) - \Delta E(t) = Q(t) - W(t) \quad (\text{A-20})$$

Where: $U(t) = m_1(t)C_v\Delta T_1(t)$ (A-21)

$$\Delta E(t) = \Delta m_1(t)C_pT_1(t)$$

$$\Delta Q(t) = 0$$

$$W(t) = p_1(t)A_1\Delta h_1(t)$$

$$m_1(t)C_v\Delta T_1(t) - \Delta m_1(t)C_pT_1(t) = -p_1(t)A_1\Delta h_1(t) \quad (\text{A-22})$$

Dividing equation A-22 by Δt and letting the limit tend to zero to solve for an expression for temperature $\dot{T}_1(t)$:

$$m_1(t)C_v\dot{T}_1(t) = -p_1(t)A_1\dot{h}_1(t) + \dot{m}_1(t)C_pT(t) \quad (\text{A-23})$$

$$\dot{T}_1(t) = \frac{-p_1(t)A_1\dot{h}_1(t) + \dot{m}_1(t)C_pT(t)}{m_1(t)C_v} \quad (\text{A-24})$$

Substituting equation A-24 into the state equation A-19 allows the simplification of the state equation for the rate of pressure change.

$$\dot{p}_1(t) = \frac{\dot{m}_1(t)RT_1(t)}{A_1h_1(t)} - \frac{A_1\dot{h}_1p_1(t)}{A_1h_1(t)} + \frac{m_1(t)R}{A_1h_1(t)} \left[\frac{\dot{m}_1(t)C_pT_1(t)}{m_1(t)C_v} - \frac{p_1(t)A_1\dot{h}_1(t)}{m_1(t)C_v} \right] \quad (\text{A-25})$$

$$\dot{p}_1(t) = \left[1 + \frac{C_p}{C_v} \right] \frac{\dot{m}_1(t)p_1(t)}{m_1(t)} - \left[1 + \frac{R}{C_v} \right] \frac{\dot{h}_1(t)p_1(t)}{h_1(t)} \quad (\text{A-26})$$

The energy equation for pipe flow derived from equation 2-8 is applied to CV₂ to determine the mass flow rate of air through the orifice.

$$\frac{p_1 - p_2}{\rho g} + \frac{\Delta(V^2)}{2g} + \Delta z = h_L \quad (\text{A-27})$$

Since the change in kinetic energy $\Delta(V^2)$ and potential energy Δz in the orifice (CV₂) is small compared to the pressure difference over the orifice, they are omitted from the energy equation. The thickness of the orifice is small relative to the size of the air chamber therefore it is assumed that the air-velocity through the orifice volume V_2 is constant. The energy equation simplifies to equation A-28, where the pressure p_2 signifies the atmospheric pressure p_a .

$$h_L = \frac{p_1 - p_a}{\rho g} \quad (\text{A-28})$$

The head losses h_L of the air-flow comprises of the major and minor losses.

$$h_L = h_{L,major} + h_{L,minor} \quad (\text{A-29})$$

$$h_{L,major} = f \frac{L_{duct} V_2^2}{D_2 2g} \quad (\text{A-30})$$

$$\text{Where,} \quad f = \frac{1}{\left[-0.86 \ln \frac{\varepsilon}{3.7 D_2}\right]^2} \quad (\text{A-31})$$

The major losses for this model of the OWC model will be negligible due to the roughness ε of the OWC model's design material (perspex) being zero (Çengel and Cimbala, 2010). The minor losses are applicable for the contraction losses K_c , expansion losses K_e and the auxiliary losses K_{aux} .

$$h_{L,minor} = K_c \frac{V_2^2}{2g} + K_e \frac{V_2^2}{2g} + K_{aux} \frac{V_2^2}{2g} \quad (\text{A-32})$$

Consequently, the head loss term simplifies to:

$$h_L = (K_c + K_e + K_{aux}) \frac{V_2^2}{2g} \quad (\text{A-33})$$

The energy equation can now be used to find an expression for the air-velocity through CV₂.

$$V_2 = \sqrt{\frac{|p_1 - p_a|}{\rho(t)(K_c + K_e + K_{aux})}} \quad (\text{A-34})$$

The mass flow rate $\dot{m}_2(t)$ of air is defined for CV₂ as the product of the density of the air $\rho(t)$ with the air-velocity through the orifice $V_2(t)$. The direction of the mass flow rate is defined by the sign of the pressure drop ($p_1 - p_a$), thus positive for mass flow into the CV₂ and negative for mass flow out of it. If the mass flow rate for CV₁ is required, the sign term changes to $(p_a - p_1)$.

When $\dot{m}_1 = -\dot{m}(t)$ then $\dot{m}_2 = \dot{m}(t)$ and when $\dot{m}_1 = \dot{m}(t)$ then $\dot{m}_2 = -\dot{m}(t)$.

$$\dot{m}_2(t) = \rho(t)A_2V_2(t) = \rho(t)A_2\sqrt{\frac{|p_1-p_a|}{\rho(t)(K_c+K_e+K_{aux})}} \cdot \text{sign}(p_1 - p_a) \quad (\text{A-35})$$

The density of air is calculated using equation A-36.

$$\rho(t) = \frac{m_1(t)}{V_1(t)} = \frac{p_1}{RT_1(t)} \quad (\text{A-36})$$

The volumetric flow rate continuity equation is given by equation A-37.

$$Q_1 = Q_2 = A_2V_2(t) \quad (\text{A-37})$$

As mentioned before, the pneumatic power $P(t)$ is calculated from the product of the volumetric flow rate $Q_2(t)$ with the pressure drop over the orifice.

$$P(t) = (p_1(t) - p_a)A_2V_2(t) \quad (\text{A-38})$$

$$\therefore P(t) = |p_1(t) - p_a| A_2\sqrt{\frac{|p_1(t)-p_a|}{\rho(t)(K_c+K_e+K_{aux})}} \cdot \text{sign}(p_a - p_1) \quad (\text{A-39})$$

The following table (Table A-3) describes the state equations defined for model 2.

Table A-3: State equations for model 2

State equations for model 2	
Pressure	$\dot{p}_1(t) = \left[1 + \frac{C_p}{C_v}\right] \frac{\dot{m}(t)p_1(t)}{m_1(t)} - \left[1 + \frac{R}{C_v}\right] \frac{\dot{h}_1(t)p_1(t)}{h_1(t)}$
Mass flow rate	$\dot{m}(t) = \rho(t)A_2\sqrt{\frac{ p_1(t) - p_a }{\rho(t)(K_c + K_e + K_{aux})}} \cdot \text{sign}(p_a - p_1(t))$
Air chamber height	$h_1(t) = L_a - h_w(t)$
	$h_w(t) = A \sin \omega t$ $L_a =$ Initial height of air chamber $A =$ Amplitude of water column displacement
Air chamber speed	$\dot{h}_1(t) = -A\omega \sin \omega t$
States	$\dot{p}_1(t), h_1(t), \dot{h}_1(t), \dot{m}(t)$

A.3. Model 3 - OWC model with pneumatic power measurement device

The final model (model 3) describes the air-flow in the OWC model with the designed pneumatic power measurement device (venturi flow meter) connected to the orifice simulated in model 2. Model 3 simulates the pneumatic power using the pressure drop over the venturi flow meter and the volumetric flow rate through it. Figure A-5 shows the diagram of the OWC model with the adjoined venturi flow meter.

Control volume 1 (CV₁) is maintained from the other models as the air-chamber volume and control volume 2 (CV₂) covers the entire venturi device. The volumetric flow rate is calculated for two scenarios which make up the bidirectional air-flow. This would be using the pressure drop from the orifice to the venturi throat Δp_o for the upward air-flow and the pressure drop from the top of the venturi to the venturi throat Δp_i for the downward air-flow. The area of the throat of the venturi flow meter is given as A_t .

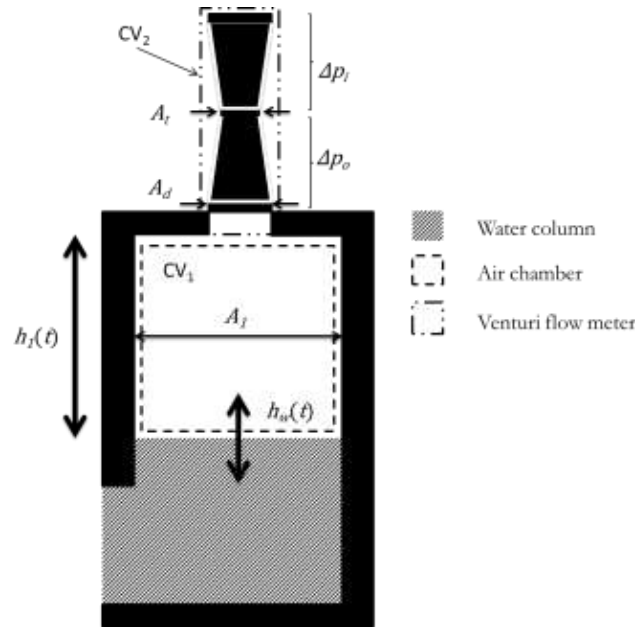


Figure A-5: Diagram of the OWC model and the pneumatic power measurement device (venturi flow meter)

The assumptions for model 3 are the same as model 2. The state equation for the pressure differential is the same as model 2 (equation A-26).

The mass flow rate through CV₂ is calculated from the volumetric flow rate equation of a venturi flow meter. The velocity through the throat of the venturi flow meter V_t is calculated using equation A-40.

$$V_t = \frac{A_d}{A_t} \sqrt{\frac{2\Delta p_{i,o}(t)}{\rho \left(\left(\frac{A_d}{A_t} \right)^2 - 1 \right)}} \quad (\text{A-40})$$

Where: A_d is the area of the air-duct connected to the venturi flow meter
 A_t is the area at the throat of the venturi flow meter
 $\Delta p_{i,o}$ is the pressure differential between the air-ducts and venturi throat

The mass flow rate through CV₂, given by equation A-43, is calculated using the volumetric flow rate through the venturi flow meter. The volumetric flow rate continuity equation is given by equation A-41.

$$Q_1 = Q_2 = A_d V_d(t) = A_t V_t(t) \quad (\text{A-41})$$

$$\dot{m}_2(t) = \rho(t) A_t V_t(t) \quad (\text{A-42})$$

$$\therefore \dot{m}_2(t) = \rho(t) A_d \sqrt{\frac{2\Delta p_{i,o}(t)}{\rho(t) \left(\left(\frac{A_d}{A_t} \right)^2 - 1 \right)}} \cdot \text{sign}(p_1 - p_a) \quad (\text{A-43})$$

The pneumatic power through the venturi flow meter can be calculated using the pressure differential over the device and the volumetric flow rate through it.

$$P(t) = (p_1(t) - p_a) Q_2(t) \quad (\text{A-44})$$

$$\therefore P(t) = (p_1(t) - p_a) A_d \sqrt{\frac{2\Delta p_{i,o}(t)}{\rho(t) \left(\left(\frac{A_d}{A_t} \right)^2 - 1 \right)}} \quad (\text{A-45})$$

The following table (Table A-4) describes the state equations defined for model 3.

Table A-4: State equations for model 3

State equations for model 3	
Pressure	$\dot{p}_1(t) = \left[1 + \frac{C_p}{C_v} \right] \frac{\dot{m}(t) P_1(t)}{m_1(t)} - \left[1 + \frac{R}{C_v} \right] \frac{\dot{h}_1(t) P_1(t)}{h_1(t)}$
Mass flow rate	$\dot{m}(t) = \rho(t) A_d \sqrt{\frac{2\Delta p_{i,o}(t)}{\rho(t) \left(\left(\frac{A_d}{A_t} \right)^2 - 1 \right)}} \cdot \text{sign}(p_a - p_1(t))$
Air chamber height	$h_1(t) = L_a - h_w(t)$
	$h_w(t) = A \sin \omega t$ $L_a =$ Initial height of air chamber $A =$ Amplitude of water column displacement
Air chamber speed	$\dot{h}_1(t) = -A\omega \sin \omega t$
States	$\dot{p}_1(t), h_1(t), \dot{h}_1(t), \dot{m}(t)$

A.4. Values for simulation parameters

The table below (Table A-5) lists the values and units of the simulation parameters used in the air-flow models.

Table A-5: Simulation parameters

Parameter	Value	Units
R	287	J/kg.K
C_p	1,005	J/kg.K
C_v	718	J/kg.K
T_a	288	K
P	101,325	Pa
ρ	1.23	kg/m ³
μ	1.79E-5	N.s/m ³
K_c	0.5	-
K_e	1	-
g	9.81	m/s ²
L_a	0.4/0.5	m
A_d	0.0154	m ²
A_t	0.0025	m ²
$m_{air,initial}$	0.02	kg

B. Dimensions of constructed test equipment

Figure B-1 shows the dimensions of the complete OWC model with the measuring device attached and Figure B-2 shows the detailed dimensions of the pneumatic power measurement device.

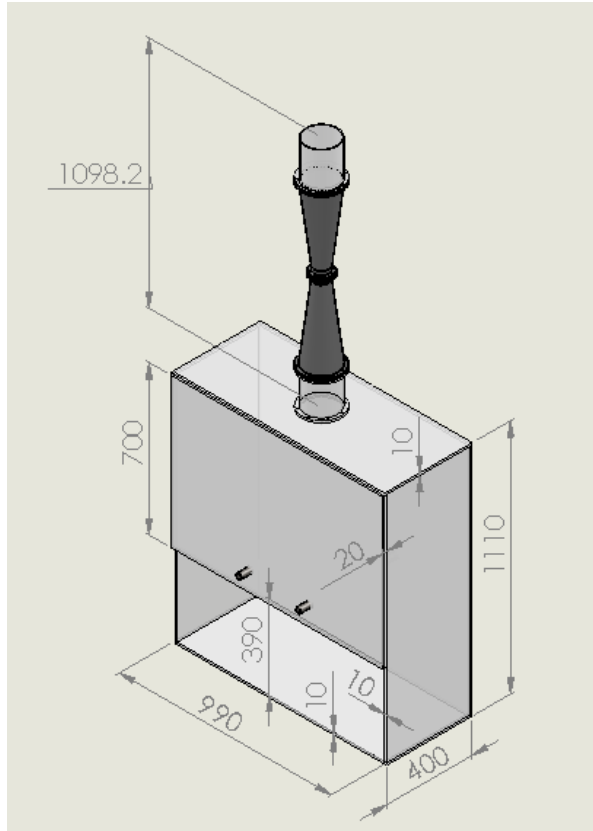


Figure B-1: Dimensions (mm) of constructed OWC box with pneumatic power measurement tool attached (SolidWorks, 2010)

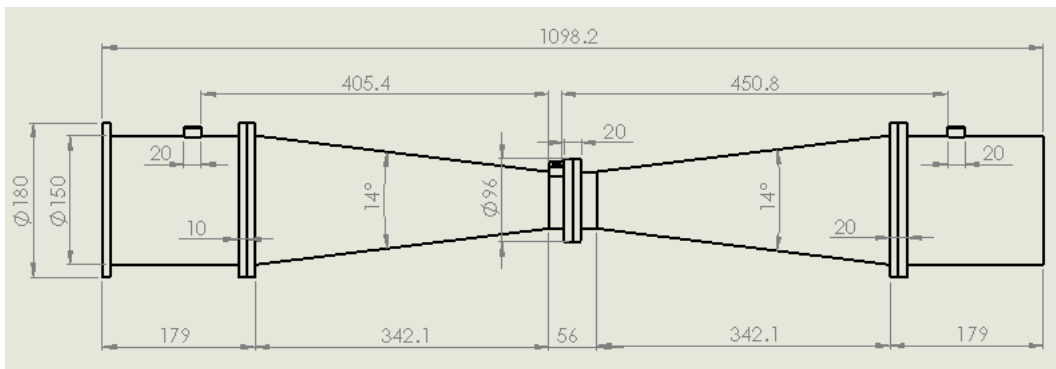


Figure B-2: Detailed dimensions (mm) of pneumatic power measurement device (SolidWorks, 2010)

C. Calibration and wave flume testing

C.1. Images from calibration tests



Figure C-1: Assembled pneumatic power measurement device



Figure C-2: Vertical wind tunnel



Figure C-3: Venturi clamped to wind tunnel with air-tight seal on air-duct of the device



Figure C-4: Support of venturi during blocked test with polystyrene seal

C.2. Images from wave flume tests



Figure C-5: Wave probes and assembled OWC model with measuring device



Figure C-6: Gauge pressure transducer and hot-film anemometer



Figure C-7: Differential pressure transducer



Figure C-8: Attached pneumatic power measuring device with air-tight seal





Figure C-9: Front and back supports of the OWC model



Figure C-10: Threaded rods strengthening the OWC model



Figure C-11: DAQ and PSU



Figure C-12: DAQ for wave probes and differential pressure transducer

C.3. Data acquisition (DAQ) wiring diagram

The MicroDAQ was set on differential signal measurement thereby measuring the voltage difference across two of its analog channels (ACH). Transducers labelled 1 to 3 were for the differential pressure measurements in the venturi flow meter. Transducer 4 was the hot-film anemometer probe which had two output connections: the analog output signal and the flow-direction output signal. The HR DAQ unit controlled the voltage output signals from the wave probes and the differential pressure transducer (transducer number 5 in Figure C-13) connected to the air chamber of the OWC model. This pressure transducer was added to the same DAQ as the wave probes so that the time series measurements of the water column displacement and the air chamber pressure oscillations were the same.

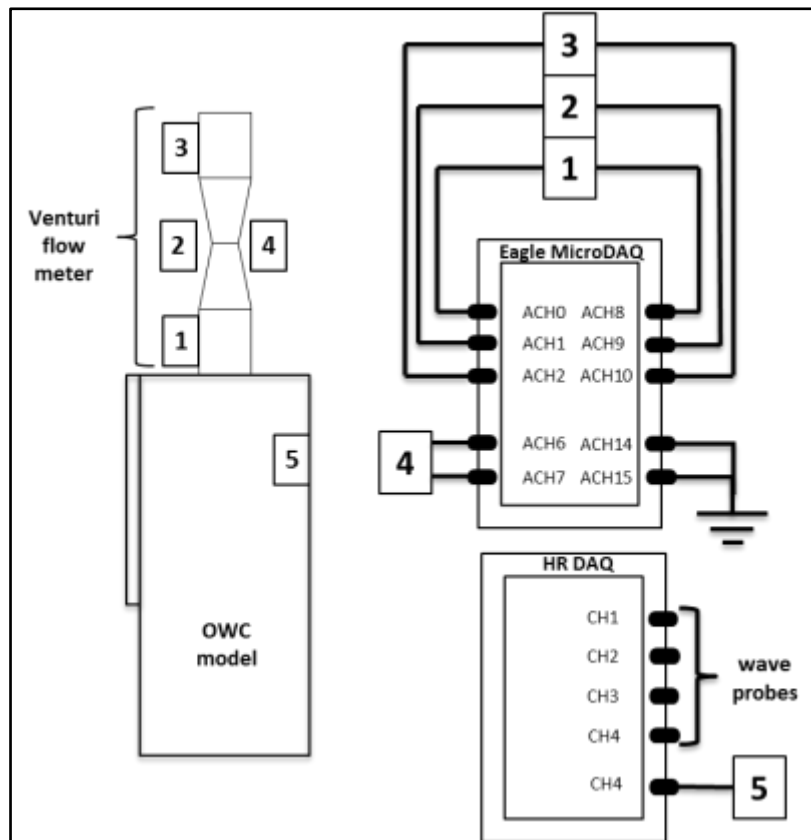


Figure C-13: Wiring diagram during the wave flume experiments

D. Measuring equipment

Table D-1: Detailed list of measuring equipment

Measuring Equipment	Manufacturer	Model Number	Specifications	Used for
Gauge pressure transducer	Ellison Sensors	LP1000	Operating range: -5kPa-5kPa Accuracy: 2.5% FSO Output signal: 4-20mA Supply voltage: 13-36Vdc Pressure connection: 1/4" BSP	Venturi pressure drop
Differential pressure transducer	Endress & Hauser		Operating range: -2.5kPa-2.5kPa. Serial Number: 54Q0200	OWC air-chamber pressure
Hot-film anemometer	SCHMIDT®	SS 20.400	Operating range: 0-20 m/s Frequency response: 0.01s Output signal: 0-10V Supply voltage:	Venturi throat velocity
Data acquisition unit	Eagle	USB-30A16	16 analog input channels Sampling rate: 250 kHz Input ranges: $\pm 2.5V$ $\pm 5V$ $\pm 10V$ 0-5V 0-10V (adapter for 4-20mA)	Handle data from pneumatic power measuring device
Power supply			DC output: 0-24 V	
Wave probes	HR Wallingford	EQ009	Frequency response: 0.01s	wave flume and OWC model
Data acquisition unit	HR Wallingford	HR DAQ		Handle data from wave probes

E. Testing schedule

E.1 Wave flume testing schedule (smaller wave heights)

Water depth (m)	Frequency (Hz)	Wavelength (m)	Absorption Gain	Wave Height (m)	Comments
0.7	1.00	1.55	320	0.05	No oscillations
	0.67	3.12	340	0.05	Oscillations out of phase
				0.1	
	0.57	3.80	400	0.05	Oscillations out of phase
				0.1	Large air-chamber pressures
	0.50	4.62	430	0.05	Planar water column, almost in phase
				0.1	
	0.44	5.30	460	0.05	-
				0.1	-
	0.40	6.06	500	0.05	-
				0.1	-
	0.33	7.40	620	0.05	-
0.6	1.00	1.54	320	0.05	-
	0.67	3.00	340	0.05	Sloshy water column
				0.1	
	0.57	3.60	420	0.05	Planar water column however out of phase
				0.1	
	0.50	4.35	430	0.05	Planar water column
				0.1	
	0.44	5.10	480	0.05	Planar water column and larger water column displacement than input wave height
				0.1	
	0.40	5.67	520	0.05	-
				0.1	Planar water column with large water column oscillations
	0.33	7.00	620	0.05	In phase water column
				0.01	Slightly out of phase, substantial reflection back to wave maker

0.5	0.67	2.83	420	0.05	-
	0.57	3.45	500	0.05	Planar water column
	0.50	4.00	540	0.05	-
	0.44	4.50	580	0.05	In phase water column
	0.40	5.24	620	0.05	-
	0.30	6.40	740	0.05	-

Table E-1: Wave flume testing schedule (smaller wave heights)

E.2 Wave flume testing schedule (larger wave heights)

Water Depth (m)	Frequency (Hz)	Wavelength (m)	Absorption Gain	Wave height (m)	Comments
0.6	0.50	4.35	430	0.125	Wave overtopping
	0.44	5.10	480	0.125	Wave overtopping
			-	0.150	Severe wave overtopping

Table E-2: Wave flume testing schedule (larger wave heights)

E.3 Wave flume theoretical performance curve

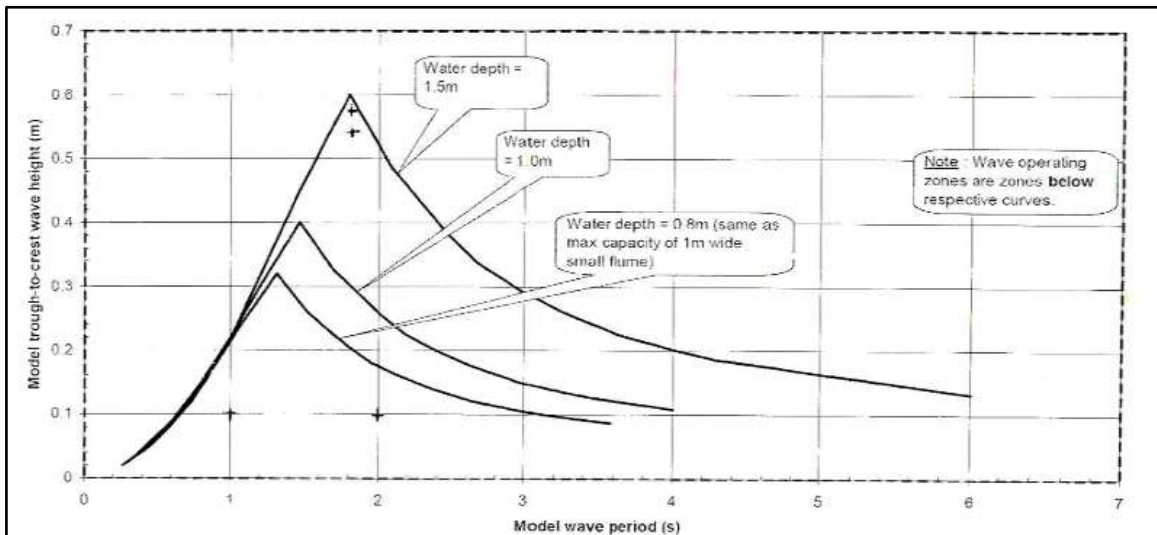


Figure E-1: Wave flume theoretical performance curve (HR Wallingford, 2010)

E.3 Absorption gain curve

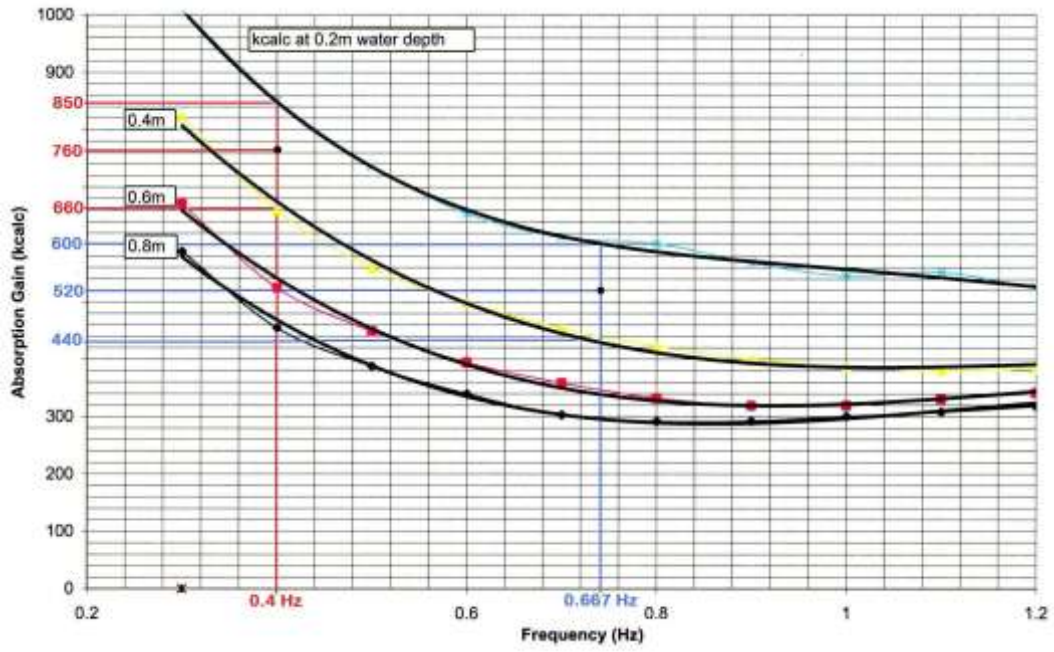


Figure E-2: Absorption gain identifier for various water depths

F. Additional pneumatic power measurement results

Figure F-1 is an example of the post processed pneumatic power results (bottom graph) calculated from the pressure drop over the throat of the venturi flow meter (top graph) and the volumetric flow rate through the venturi flow meter (middle graph). These graphs below depicts the results for the water depth of $D = 0.6$ m at wave height $H_w = 0.1$ m and frequency of $f = 0.5$ Hz.

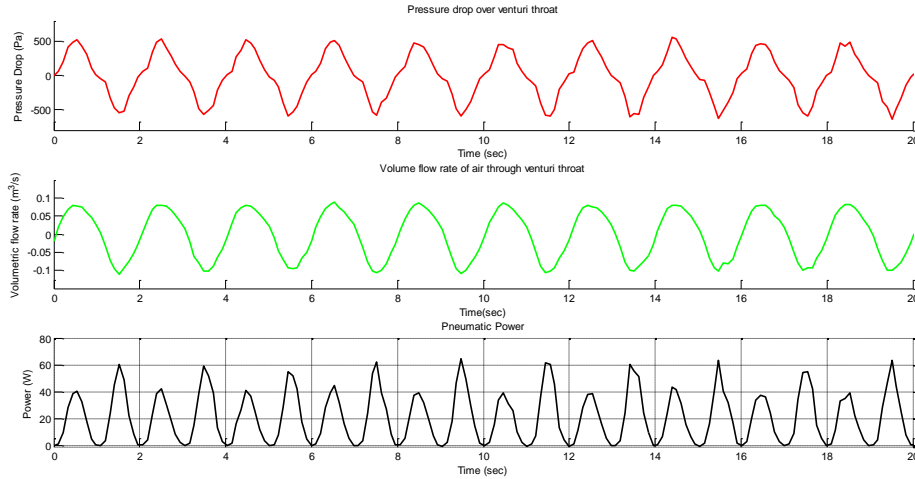


Figure F-1: Example of post processed results from the experimental tests

Figure F-2 and Figure F-3 show the graphs of the pneumatic power measured by the pneumatic power measurement device for larger wave heights.

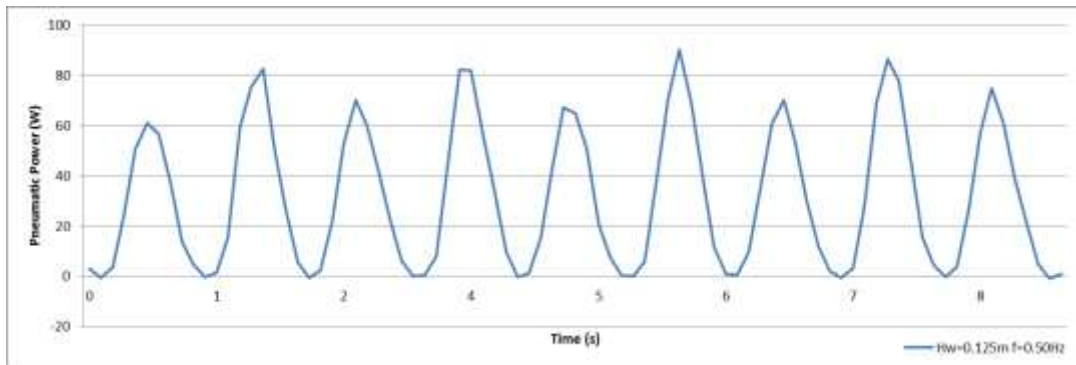


Figure F-2: Pneumatic Power for larger wave heights at test parameters: $H_w = 0.125$ m $f = 0.5$ Hz

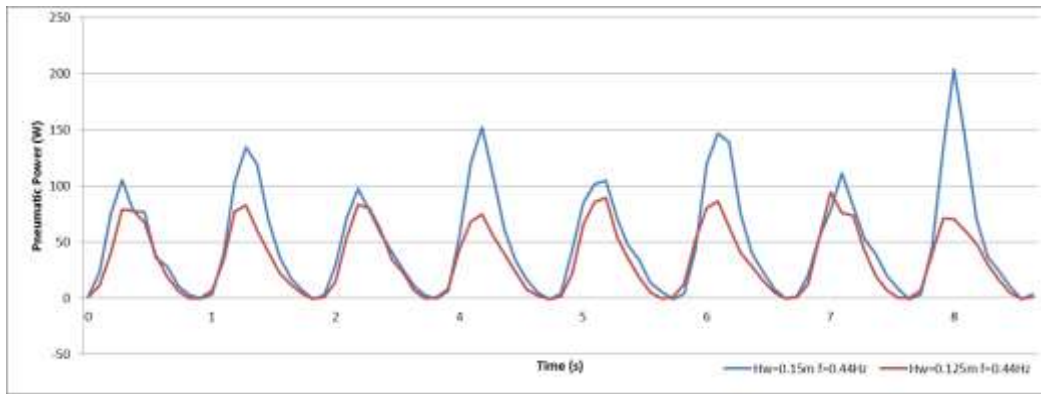


Figure F-3: Pneumatic Power for larger wave heights at test parameters: $H_w=0.125\text{m}$ $f=0.44\text{Hz}$ & $H_w=0.15\text{m}$ $f=0.44\text{Hz}$

G. Additional information on OWC devices

G.1. Operational OWC devices

There are a few OWC devices that are operational at the moment. They range from shoreline, nearshore and deep sea systems. With regards to the operational aspects of these working devices, the success and faults can be noted and learnt from in future applications of OWC devices. One of the main shoreline OWC devices that are operational is the LIMPET (Land Installed Marine Powered Energy Transformer) of Wavegen Ltd.

The LIMPET is a full scale OWC wave energy converter constructed in the United Kingdom. The location for this WEC is on the South Western coast of the Hibrudean island of Islay in Scotland. This 500 kW OWC device was designed by Queen's University of Belfast (QUB) from Ireland and Wavegen Ltd. from Scotland. The commissioning of the full scale device was based on the satisfactory performance of a prototype test unit developed by QUB in 1991 (Boake et al, 2002).

The basic design of the LIMPET shown in Figure G-1 is an inclined shore mounted water column, angled at 40° to the horizontal. The inclined nature of the column reduces turbulence and sloshing in the water column. The span of the structure is made up of 3 individual water columns spreading over a 21m width. The resultant air flow through these columns is channelled into a turbo-generation duct, which forms the exit path of the air flow during compression. The presence of the Well's turbine in the turbine unit allows the use of the bi-directional flow of air into and out of three columns. Additional features of the LIMPET are a pair of pressure relief valves and a wave breaker. The pressure relief valves, found in two of the columns, provide pneumatic control of the airflow of the system, especially during extreme operating conditions. The wave breaker at the external face of the column serves to reduce the amount of incoming waves that overtops the collector. The structural and control aspects of the system are a remarkable step into shoreline OWC research and implementation.

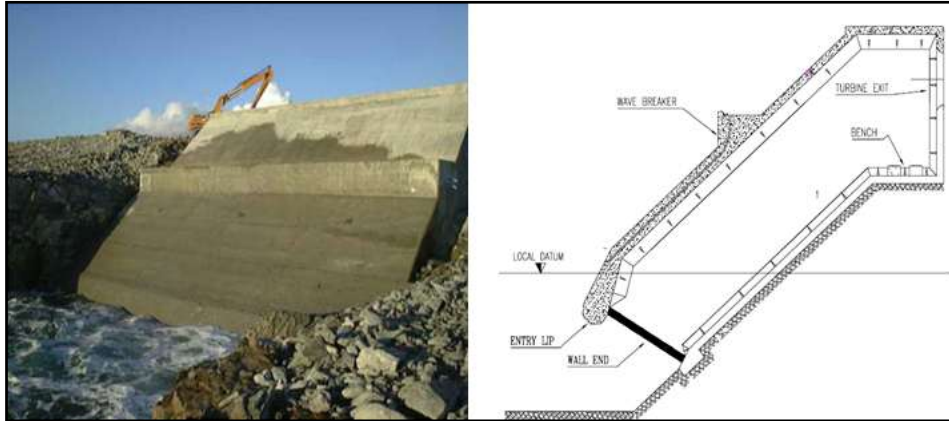


Figure G-1: LIMPET Construction and Incline Design Structure (Boake et al, 2002)

The latest commercial OWC device is the Mutriku Wave Power Plant located in Mutriku, Spain, which comprises of 16 OWC chamber's incorporated into a breakwater structure. Torre-Enciso et al (2009) mentions that Mutriku is the first breakwater to have several turbines installed into it, subsequently giving the structure a total power capacity of 296 kW. Other current operational OWC devices that are worth a mention are the Pico Power Plant (shoreline OWC) on the island of Azores, Vizhinjam OWC in India and the Sakata breakwater OWC in Japan (van Niekerk, 2010).

G.2. OWC related terminology

Capture Width	The maximum linear horizontal dimension of the collector chamber, or collector chamber plus guide walls where present, perpendicular to the approaching wave front
Pneumatic Efficiency	Proportion of wave energy captured in the compression and rarefaction of the air in the collector with respect to the total wave energy flux crossing a line equal to the capture width
Shoreline	An OWC is classified shoreline if connected to the shore above mean high water. It also includes OWC's using tunnel technology
Nearshore	OWC device close to the shore but not connected to it
Breakwater	Structure that provides sheltered conditions in its lee

Caisson	Monolithic structure (steel or concrete), usually divided into compartments, which is deployed in a marine environment
Power Train	Combination of turbine, gearbox/flywheel and generator
Inlet Broaching	The water level in the OWC drops below the front lip level and a direct air passage is opened between the air chamber and the atmosphere. This fault allows loss of pressure in chamber and consequently reduces pneumatic efficiency.
Rarefaction	Decrease in pressure of a medium (air in the case of an OWC device)
Heave	Upward lift of wave motion